Supercontinuum radiation for ultra-high sensitivity liquid-phase sensing

This dissertation is submitted for the degree of
Doctor of Philosophy

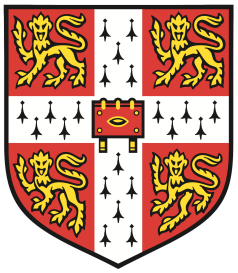

Ssegawa-Ssekintu Kiwanuka

Queens' College

July 2013

University of Cambridge

Department of Chemical Engineering & Biotechnology

Maama ne Taata

Preface

This dissertation is the result of my own work and includes nothing which is the outcome of work done in collaboration except where specifically indicated in the text. In total this document contains approximately 40,000 words and 66 figures. I confirm that the work contained in this dissertation, or any part thereof, has not been submitted for any other degree. The research presented here has been carried out at the Department of Chemical Engineering & Biotechnology, University of Cambridge, between October 2009 and January 2013.

Summary

The real-time detection of trace species is key to a wide range of applications such as on-line chemical process analysis, medical diagnostics, identification of environmentally toxic species and atmospheric pollutant sensing. There is a growing demand for suitable techniques that are not only sensitive, but also simple to operate, fast and versatile. Most currently available techniques, such as spectrophotometry, are neither sensitive enough nor fast enough for kinetic studies, whilst other techniques are too complex to be operated by the non-specialist.

This thesis presents two techniques that have been developed for and applied to liquid-phase analysis, with supercontinuum (SC) radiation used for liquid-phase absorption for the first time. Firstly, supercontinuum cavity enhanced absorption spectroscopy (SC-CEAS) was used for the kinetic measurement of chemical species in the liquid phase using a linear optical cavity. This technique is simple to implement, robust and achieves a sensitivity of $9.1 \times 10^{-7}\,\mathrm{cm^{-1}\,Hz^{-1/2}}$ at a wavelength of 550 nm for dye species dissolved in water. SC-CEAS is not calibration-free and for this purpose a second technique, a time-resolved variant called broadband cavity ring-down spectroscopy (BB-CRDS), was successfully developed. Use of a novel single-photon avalanche diode (SPAD) array enabled the simultaneous detection of ring-down events at multiple spectral positions for BB-CRDS measurements.

The performance of both techniques is demonstrated through a number of applications that included the monitoring of an oscillating (Belousov-Zhabotinsky) reaction, detection of commercially important photoluminescent metal complexes (europium(III)) at trace level concentration, and the analysis of biomedical species (whole and lysed blood) and proteins (amyloids). Absorption spectra covering the entire visible wavelength range can be acquired in fractions of a second using sample volumes measuring only 1.0 mL. Most alternative devices capable of achieving similar sensitivity have, up until now, been restricted to single wavelength measurements. This has limited speed and number of species that can be measured at once. The work presented here exemplifies the potential of these techniques as analytical tools for research scientists, healthcare practitioners and process engineers alike.

Acknowledgements

The work in this thesis would not have been possible without the support and guidance of my supervisor Prof Clemens Kaminski. Under his tutelage I have not only grown and developed as a researcher, but also as an individual. I would like to thank him for this great opportunity and experience.

I would also like to give special thanks to Dr Toni Laurila who was instrumental in teaching me important experimental skills at the start of my research. He has been very generous in his continued support from Finland and there are many stimulating theoretical discussions that we have had.

I have been fortunate enough to work with the following external collaborators, whom I must also thank: Dr Anita Jones (University of Edinburgh); Dr Jim Stone and Prof Jonathan Knight (University of Bath); Dr Jonathan Frank (Sandia National Laboratories, USA); Dr Alessandro Esposito (Hutchison/MRC Research Centre, Cambridge); Dr Teresa Tiffert and Dr Virgilio Lew (Department of Physiology, Development and Neuroscience, University of Cambridge); and Dr David Stoppa (Fondazione Bruno Kessler, Italy). Within the Laser Analytics Group I would like to thank Dr Miklos Erdelyi, Dr Eric Rees, Dr Rosalynne Watt, Dr Zhechao Qu and Dr Chu Liu for sharing their optics and physics expertise and Dr Gabi Kaminski and Fiona Chan for assistance with biological samples. Special thanks goes to Dr Johan Hult for first encouraging me to join the group for my Master's project. Past and present members of LAG have made the long hours in the lab both enjoyable and fulfilling over the past few years, so my thanks extends to them all. I extend my gratitude to Anne Philpott for proof reading.

The Engineering and Physical Research Council (EPSRC) kindly provided funding for this research. I am also grateful to Queens' College, the Department of Chemical Engineering, Roche Continents, Sensors for Water Interest Group and Institution of Chemical Engineers for generous financial contributions, grants and awards.

Lastly I would like to thank my parents Jim and Barbara who simply mean everything to me - Maama ne Taata mbaagala nnyo.

List of Publications

Work presented in this thesis has resulted in the publications listed below. Conference contributions are listed in Appendix B.

- S.-S. Kiwanuka, T.K. Laurila and C.F. Kaminski. **Sensitive method for the kinetic measurement of trace species in liquids using cavity enhanced absorption spectroscopy with broad bandwidth supercontinuum radiation**. *Analytical Chemistry*, 82 (17), pp 7498-7501 (2010).

- S.-S. Kiwanuka, T.K. Laurila, J.H. Frank, A. Esposito, K. Blomberg von der Geest, L. Pancheri, D. Stoppa, C.F. Kaminski. **Development of broadband cavity ring-down spectroscopy for biomedical diagnostics of liquid analytes**. *Analytical Chemistry*, 84 (13), pp 5489-5493 (2012).

Abbreviations

BB-CRDS	Broadband cavity ring-down spectroscopy
CCD	Charge-coupled device
CEAS	Cavity enhanced absorption spectroscopy
CMOS	Complementary metal-oxide semiconductor
CRDS	Cavity ring-down spectroscopy
CW	Continuous-wave
EM-CCD	Electron-multiplying charge-coupled device
FWHM	Full width at half maximum
FWM	Four-wave mixing
GVD	Group velocity dispersion
IR	Infrared
MI	Modulation instability
PCF	Photonic crystal fibre
PMT	Photomultiplier tube
SC	Supercontinuum
SC-CEAS	Supercontinuum cavity enhanced absorption spectrscopy
SNR	Signal-to-noise ratio
SPM	Self-phase modulation
UV	Ultraviolet
XPM	Cross-phase modulation
ZDW	Zero dispersion wavelength

Contents

Chapter 1

Introduction

The work presented in this thesis documents the development of spectrometers for liquid-phase analysis. The spectrometers employ broad spectral bandwidth supercontinuum radiation and cavity-enhanced techniques for highly sensitive and quantitative absorption measurements. This chapter introduces the motivation behind such developments and current opportunities presented by advancements in light source, detector and fibre technology. The chapter concludes with a summary of the main contributions of this work and the thesis structure.

1.1 Motivation: Demand for sensitive liquid absorption techniques

The analysis of liquids is an important requirement for understanding a number of fundamental scientific questions. There is high demand for rapid and sensitive concentration measurement of liquid analytes from a number of industries and areas of scientific research. For example, many fundamental biological processes occur in liquids at low concentrations. Therefore, a sensitive tool for analysis would be beneficial in the life sciences. Applications in the chemical process industry may not only require high sensitivity to measure small changes in reactant concentrations, but also sufficient measurement speed in order to monitor reaction dynamics. Flexibility is also another important factor as it may be necessary to detect a number of different trace molecule or compounds simultaneously, for

example, different environment-contaminating compounds in a waterway.

The measurements in this work are based on the interaction of electromagnetic (EM) fields with matter, which is overt in the field of science and forms the basis of optical spectroscopy. All atoms and molecules absorb EM radiation at some frequency and can thus be studied using a radiation source and a suitable detector. Benefits of optical spectroscopy include rapid, non-intrusive, sensitive and non-destructive measurements that can enable quantitative analysis. For a number of years, spectrophotometers have been used for spectroscopic analysis of liquids. The measurement sensitivity of such machines is limited and, as a result, they are not capable of detecting any of the samples at the concentrations presented in this work. There are number of high sensitivity absorption techniques for the gas phase, but these have yet to be translated into techniques for liquid-phase analysis. One such group of techniques employs optical cavities for orders of magnitude sensitivity enhancements.

The advent of broad spectral bandwidth light sources of high intensity opens up new possibilities. The aim in this work is to exploit the unique features of supercontinuum (SC) radiation which is informally known as a "white-light laser". SC radiation will be applied to liquid-phase direct absorption measurements for the first time. Light from the SC source will be coupled into an optical cavity formed by two highly reflective mirrors. This increases the sensitivity of the optical absorption technique by orders of magnitude over conventional single pass techniques. The use of SC light with cavity-enhanced absorption techniques utilising optical cavities should, in principle, provide a number of technological advantages for liquid analysis. There are a number of challenges in first generating broad bandwidth laser-like light and then secondly the increased solvent absorption in liquids. The motivation for this work is to develop a sensitive system of measurement for liquid analytes that can offer advances over existing techniques. This will thus enable greater levels of interrogation that up until now have been limited by the available technology.

1.2 Background principles

Optical Absorption

Electromagnetic (EM) radiation is commonly used for atomic and molecular analysis with their resulting spectra providing "fingerprints" for different species, enabling identification and, most importantly, quantification. Optical techniques can often be integrated into existing experimental set-ups, for example, process control lines. Some disadvantages include the potentially high cost of high sensitivity systems, the need for calibration in some cases and requirements for optical access. Furthermore, spectral overlap caused by the presence of multiple species may make quantitative analysis of each constituent difficult or even impossible. Such spectral interference is less important for analysis of small molecules in the gas phase, but may be an added challenge in the liquid phase, due to the broader spectra, as discussed in later chapters of this thesis.

Absorption spectroscopy is based on measuring the attenuation of light passing through a sample. Strictly speaking, the attenuation is caused by extinction, which is due to both absorption and scattering of the sample. The background (off-resonance) signal provides the baseline measurement. The amount of attenuation caused by the sample upon absorption is quantified using the Beer-Lambert law. The intensity I (W/m^2) transmitted through the sample is given by Equation 1.1.

$$I = I_0 \exp(-\epsilon C d), \tag{1.1}$$

where I_0 (W/m^2) is the incident intensity (or irradiance), ϵ (M^{-1} cm^{-1}) is the molar extinction coefficient, d (cm) is the sample pathlength and C (M) is the sample concentration. The absorption coefficient, α (cm^{-1}), is defined as $\alpha = \epsilon C$, directly relating it to sample concentration.

Absorption measurements are based on measuring small changes in intensity which appear over a large signal background. Fluorescence measurements on the other hand detect the emission radiating from atoms or molecules that have been excited by absorption. The fluorescence emission spectrum is redshifted from the excitation light and can thus be distinguished. This makes fluorescence the most

sensitive of all concentration measurement techniques as it essentially features a zero background. Although it allows for sensitive measurements, fluorescence suffers from quenching. Quenching results from loss of excitation energy through collisions with other atoms or molecules. As a result, this lost energy is not detected which prevents precise quantification of the total fluorescence. Furthermore, not all molecules fluoresce which limits the application of fluorescence techniques. These non-fluorescent analytes may, however, still be detectable by absorption, assuming sensitivity is not limiting.

Simple commercial spectrophotometers are widely available and routinely used in research and industry. These instruments are based on single-pass absorption and, as a result, their sensitivity is typically limited [Berden et al., 2000]. Measurements of 1.0 mL dye solutions were made with a commercial double-beam ultraviolet (UV)-visible spectrophotometer (UV1, Thermo Scientific, USA). The minimum detectable absorption coefficient obtained in a standard cuvette of 1.0 cm pathlength was $10^{-3}\,\mathrm{cm}^{-1}$, in agreement with the manufacturer technical specifications.

Cavity-enhanced techniques, such as cavity ring-down spectroscopy (CRDS) and cavity enhanced absorption spectroscopy (CEAS), have been implemented to increase sensitivity by increasing the effective pathlength, as light is passed through the sample a multitude of times [Berden and Engeln, 2009]. Maximum achievable pathlengths can be in orders of magnitude greater than traditional multi-pass Herriott and White cells. The first iterations of CEAS used narrow-band sources [Engeln et al., 1998]. Such sources are not suitable for simultaneous identification of different species in a sample. Therefore, alternative light sources must be sought in order to implement CEAS over much broader spectral bandwidths. The key attributes are thus:

(i) **Broad spectral bandwidth**: Increased bandwidths to reveal entire absorption spectra of liquids and to realise multi-species detection capability.

(ii) **High spectral resolution**: Distinguish spectral fingerprints of multiple compounds in a liquid sample. This is dependent on the spectral resolution of the technique, with higher spectral resolution enabling better quantification.

(iii) **High sensitivity**: Ability to detect atoms or molecules at trace concentration levels and for the recovery of weak spectral features.

(iv) **Fast spectral acquisition times**: Take advantage of high temporal resolution for the study of dynamics that occur on sub-second timescales.

Supercontinuum Radiation

The advent of novel supercontinuum light sources has presented opportunities to advance the field of optical sensing. Supercontinuum sources combine a pulsed laser with a non-linear medium. The nonlinear medium drastically broadens the narrowband laser pulse to form a continuous spectrum of light. Early demonstrations used shards of glass or drops of water to act as the nonlinear medium [Alfano and Shapiro, 1970; Jimbo et al., 1987]. It was not until highly nonlinear waveguides, such as photonic crystal fibres (PCF), came along that SC could be generated far more efficiently and conveniently. The first supercontinuum generated in photonic crystal fibre (PCF) was demonstrated by Ranka et al. [2000] and a recent publication presented a spectrum spanning 3.3 octaves reaching 4.5 µm in the mid infrared [Silva et al., 2012].

The exact same principle of total internal reflection used by standard optical fibres is used in PCF to guide light. The key difference from standard fibres is the physical structure. Standard optical fibres contain a glass core surrounded by a doped-glass cladding layer with a slightly lower index of refraction than the core material. This leads to wave-guiding of light through the core by total internal reflection. In contrast, PCF cladding does not contain a bulk material but rather a periodical matrix structure of both low and high refractive index materials, with light passing through a core of higher refractive index, as shown in Figure 1.1. The guiding properties of the PCF are dictated by the matrix structure and as a result can be modified by changing the hole size and/or periodicity. PCFs have been designed to enable propagation of high intensity light over very large bandwidth, which is not achievable with traditional fibres.

The single-mode power of a typical commercial SC source is shown in Figure 1.2. Light from SC sources has much higher spectral brightness which is maintained over a significantly broader spectral range. This gives rise to its colloquial

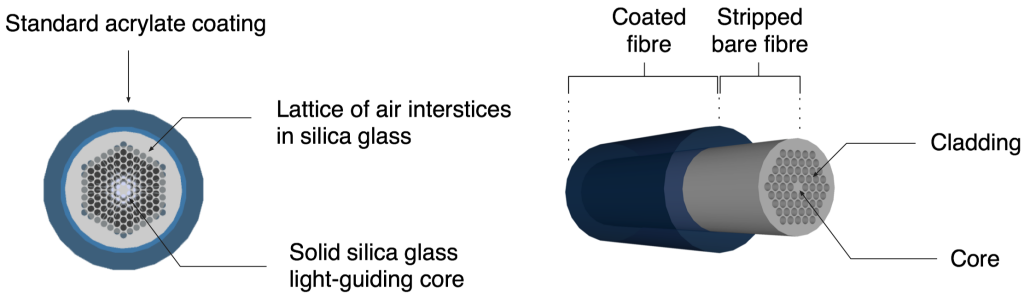

Figure 1.1: *Schematic diagram of a photonic crystal fibre (PCF). The active area of the solid core and hybrid air-silica lattice of the cladding are both highlighted.*

name of "white-light laser", as it combines some spatial and temporal properties of a laser with the extreme spectral bandwidth of a lamp. The properties of the light source will dictate the types of measurement that can be made and ultimately the overall applicability of the technique. Light sources previously used in liquid spectroscopy range from arc lamps [Fiedler, 2005] to lasers [Bahnev et al., 2005; Hallock et al., 2002] and light emitting diodes (LEDs) [Seetohul et al., 2009]. Therefore, an opportunity exists for the implementation of SC light sources for liquid-phase absorption spectroscopy.

- *Very high spectral brightness*: The high brightness is maintained throughout the visible and near-infrared spectral regions making SC flexible light sources for a number of applications. SC sources with typical average spectral power densities of 1 mW/nm throughout most of the visible range are readily available commercially.

- *High spatial coherence*: Light pulses from the pump laser source are coupled into the PCF which confines them in a single-mode waveguide resulting in very high spatial coherence and high output beam quality.

- *Pulsed output*: The pulsed nature of the pump laser source, and hence PCF output, enables time-resolved measurements to be made.

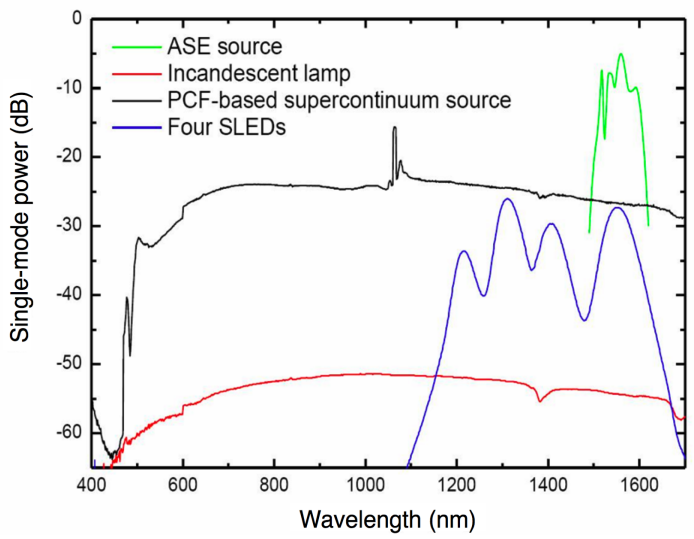

Figure 1.2: *Spectral output of PCF-based supercontinuum radiation compared with an amplified stimulated emission (ASE) source, incandescent lamp, and a superluminescent LED (SLED). Figure reproduced from manufacturer datasheet [NKT Photonics, 2009].*

1.3 Main contributions: Development of new methods

There are four main advancements in the field of liquid-phase spectroscopy presented here in this thesis:

(i) *First to perform liquid CEAS with supercontinuum radiation (SC-CEAS)*: Sensitivity down to picomolar concentrations is achieved through the use of external optical cavities. The technique is able to record broad spectral bandwidth spectra covering the visible spectrum at millisecond timescales. Furthermore, such sensitivity has been demonstrated in liquid sample path-lengths of ∼5 cm and volumes of only 1.0 mL.

(ii) *Implementation of near UV-SC to liquid sensing*: The spectral range of broadband CEAS for liquids has been significantly extended into the near-UV through the use of dispersion-engineered tapered PCF. An overview of SC generation in PCF is also given to provide more of an insight into SC

properties used here for liquid absorption spectroscopy for the first time. Both commercial and custom-built SC sources have been employed in the work here. The use of a custom-built source enabled different state-of-the-art PCF to be used, highlighting future possibilities.

(iii) *Novel use of single photon avalanche diode (SPAD) technology as a detector for broadband CRDS*: The development of broadband cavity ring-down spectroscopy (BB-CRDS) is an advancement that came out of the need for broad spectral bandwidth calibration of liquid CEAS. The implementation of SPAD array based on complementary metal-oxide semiconductor (CMOS) technology presents an opportunity to move towards a fully calibrated broadband liquid absorption technique using a detector that can be mass produced at low cost and yet still achieve sub-nanosecond time resolution.

(iv) *Demonstrated applications*: Four applications have been shown addressing different medical, scientific and technological questions. These are: monitoring of an oscillating reaction; detection of electronic transition in photophysically important lanthanide complexes; study of amyloidogenic proteins related to neurodegenerative diseases such as Alzheimer's and Parkinson's diseases; and detection of oxygenation levels in blood plasma.

1.4 Thesis outline

This first chapter provides the motivation behind the research presented in this thesis and an introduction to the background theory and experimental principles.

Chapter 2 discusses the propagation of light in photonic crystal fibres for the generation of broad supercontinuum radiation. The spectral properties of SC radiation are discussed to highlight the advantages and limitations of such sources in relation to the requirements of the optical sensing techniques developed in this work.

The principles behind the use of high finesse optical cavities for increased sensitivity for absorption techniques are introduced in Chapter 3. Both CEAS

and CRDS are discussed in the context of liquid sensing and enhancements over traditional single-pass techniques.

Chapter 4 details the design and development of SC-CEAS technique applied to liquid absorption spectroscopy. Experimental considerations and challenges specific to the liquid phase are first discussed. The experimental method is then detailed along with characterisation and calibration results.

A broadband calibration technique was developed using a SPAD array. Chapter 5 details how the enabling technology is used in the implementation of BB-CRDS.

Chapter 6 presents experimental applications that demonstrate the potential of the techniques developed in this thesis. The oscillating Belousov-Zhabotinsky reaction is used to demonstrate SC-CEAS as an optical reaction monitoring method. Detection of commercially important metal complexes at trace level highlights the significance this technique could have in high-technology industries. UV-CEAS is demonstrated for the first time to detect the early-stage aggregation of amyloidogenic proteins relevant to the study of neurodegenerative diseases. A fourth application shows the use of BB-CRDS as a stand-alone sensor for the detection of blood under different conditions, demonstrating a calibration-free sensor that could be applied to biomedical applications.

Finally, Chapter 7 sets out the conclusions of the research. It includes an overview of the work presented in this thesis and concludes with proposed future developments and improvements.

Chapter 2

Supercontinuum Generation

2.1 Introduction

The use of supercontinuum (SC) radiation as a practical light source came about in the last decade [Alfano, 2006; Dudley and Taylor, 2009]. SC sources have since been implemented in a number optical applications, including high sensitivity, broad bandwidth absorption measurements in the gas phase [Langridge et al., 2008; Thorpe et al., 2006]. The utility of SC sources for spectroscopy stems from their unique combination of bandwidth and brightness. Although often referred to as "white-light lasers", this terminology is not strictly correct as SC radiation is actually a converted form of laser light. High intensity pulsed laser light is spectrally broadened to encompass a wide range of wavelengths. This is most efficiently achieved by propagating the laser pulse along a nonlinear optic fibre. The SC generated retains laser-like properties of spatial coherence, brightness and pulsed nature from its pump source. Spatial coherence is obtained from the wave-guiding properties of the photonic crystal fibre (PCF) which allows for tight focussing and power delivery on location, both of which are desirable in spectroscopy [Dudley et al., 2006]. Such features are particularly useful for optical cavity-based techniques for which alignment is critical [Kelkar et al., 1999; Sanders, 2002; Watt et al., 2008]. Spectral brightness allows for shorter signal integration times which in turn enables faster sensing or more sensitive measurements and improves the signal-to-noise ratio. PCF-based sources are also

frequency-referenced which means they can be used for time-resolved spectroscopic measurements in sensing and microscopy [Kaminski et al., 2008].

In spite of the many advantages, there are a few challenges related to SC light generation. One example is pulse-to-pulse intensity variation. This variation stems from the inherently nonlinear processes involved in SC generation in certain PCF which could be problematic. Signal averaging could be one method of minimising such an effect, although this negatively affects the overall measurement speed. Long term intensity drifts may also be a problem for intensity-dependent measurements. The stability of the pump laser source will dictate the extent of this effect and whether it is likely to be of significant concern. A further challenge is to extend the spectral bandwidth into the UV. This would be of interest to the sensing of biological analytes in the liquid phase.

Chapter Summary

The aim of this chapter is to describe the physics behind SC light generation and discuss properties relevant to spectroscopic measurements.

2.2 Propagation of light in optical waveguides

The generation of supercontinuum radiation involves spectral broadening of a monochromatic laser pulse into a polychromatic pulse of white light. This conversion can occur in optical waveguides and is influenced by:

(i) Loss of photons by absorption.

(ii) Change of photon energy by nonlinear interactions - usually energy loss but can also be gain.

(iii) Dispersion due to photons of different energy - and corresponding wavelength, λ, - travelling at different speeds (refractive index).

The efficient generation of SC requires dispersion to be balanced with nonlinear optical effects within the waveguide [Stone and Knight, 2008]. This requires special waveguides that can be dispersion-engineered to meet such a requirement.

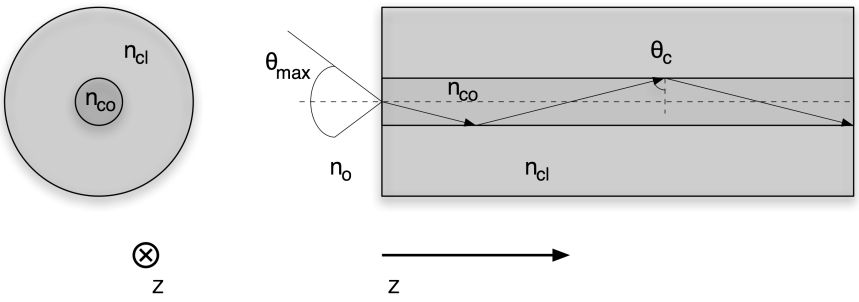

Figure 2.1: *Principle of light propagation within a conventional step-index fibre, as shown in axial and longitudinal cross-section. The maximum acceptance angle, θ_{max} is highlighted as well as the critical angle, θ_c, for total internal reflection. The core of high refractive index (n_{co}) is surrounded by a low refractive index cladding (n_{cl}).*

Conventional Step-index Fibres

Standard optical fibres are designed to carry light with minimal transmission losses. They are most widely used within the telecommunications industry for the transfer of electronic data. Light is confined within such waveguides using the principle of total internal reflection (TIR). For TIR to occur, the refractive index of the core, n_{co}, must be greater than the refractive index of the cladding, n_{cl}, as shown in Figure 2.1. A conventional step-index fibre can have refractive indices of $n_{\mathrm{co}} = 1.62$ and $n_{\mathrm{cl}} = 1.52$ [Hecht, 2002]. Light must then propagate through the fibre at an angle greater than the critical angle, θ_c. Under these conditions, no light will be refracted across the boundary from the high index core into the low index cladding, i.e. light is completely reflected at the boundary. Light thus propagates through the core and is not lost in transmission. In order to achieve efficient coupling of light into the fibre, one must match the numerical aperture (NA), or acceptance angle (θ_{max}), of the incident light beam to that of the optical fibre. The NA is calculated from the half-angle over which the fibre can accept light and is defined as $\mathrm{NA} = \sin\theta$ (where $\theta = \frac{1}{2}\theta_{\mathrm{max}}$ as depicted in Figure 2.1).

Photonic Crystal Fibres

The PCFs used in this work comprise an active core and a matrix cladding. The cladding is formed of a honeycomb-like structure of both high and low refractive

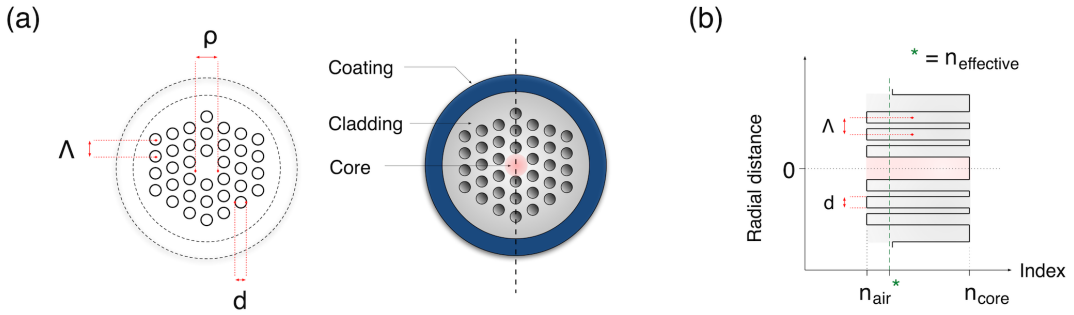

Figure 2.2: *Schematic section of a photonic crystal fibre (PCF) showing key fibre parameters. The light-guiding solid core is highlighted in red. (a) Cross-section showing fibre dimensions of core radius, ρ, hole diameter, d, and pitch, Λ. (b) Profile of the radial change in refractive index across the PCF.*

index materials, for example, air-glass microstructure cladding with low effective refractive index [Knight, 2003; Russell, 2003]. This is in contrast to standard optical fibres which most commonly contain two bulk materials, such as a silica core and a lower refractive index (solid glass) cladding. The hybrid micro-structured PCF cladding (shown in Figure 2.2) provides a stronger refractive index contrast than is the case in normal optical fibres, thus introducing the required nonlinearity to generate broadband SC [Knight et al., 1996]. The properties of the PCF are dictated by the matrix structure and three key parameters, namely: the core radius, ρ, the diameter of holes (either air-holes or cladding inclusions such as doped glass), d, and hole-to-hole spacing (pitch), Λ. Such a structure and dimensions thereof are depicted in Figure 2.2. As the core is not necessarily hollow, the diameter is defined as the shortest distance between air-holes or cladding inclusions across the centre of the fibre. It is possible to tailor these parameters and thus the dispersive qualities of the fibre whilst maintaining the tight spatial confinement of light pulses offered by an optical waveguide. This can be achieved by changing the hole size or periodicity, or by introducing complex inclusions and matrix designs.

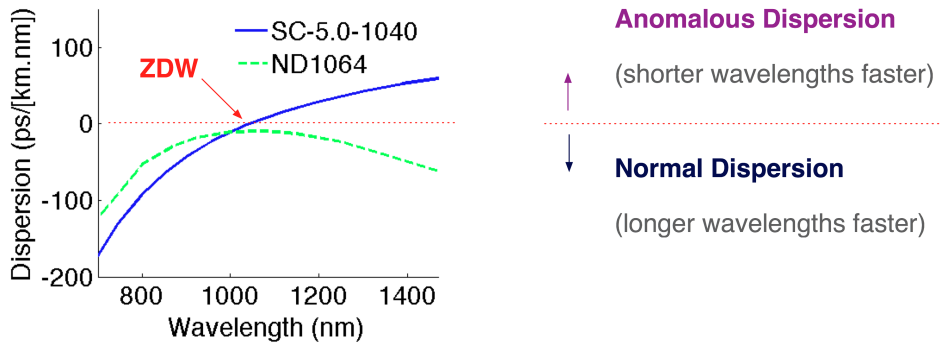

Figure 2.3: *Dispersion curves for a commercial anomalous dispersion PCF (SC-5.0-1040, NKT Photonics, Denmark) and a custom-designed all-normal dispersion PCF (ND1064, CPPM University of Bath, UK) courtesy of Hooper et al. [2011]. Anomalous and normal dispersion regions are indicated on either side of $D = 0$. The commercial PCF exhibits a zero dispersion wavelength (ZDW) at* 1040 nm*, whereas ND1064 only exhibits normal GVD.*

2.3 Theoretical background: Supercontinua

2.3.1 Dispersion

One of the two fundamental physical effects to occur in optical fibres is dispersion. Dispersion describes the wavelength dependence of group velocity refractive index which is due to both the material properties and waveguide geometry. It describes the speed at which photons of different wavelength travel.

The group velocity dispersion (GVD) is defined as the rate of change in phase of the frequency components of a wave packet. The GVD governs the temporal broadening and peak intensity as the pulse propagates along the fibre. Numerically, chromatic dispersion in a fibre is described using mode-propagation constant, β, which can be obtained by a Taylor series about the centre frequency of the input pulse, ω_0:

$$\beta(\omega) = n(\omega)\frac{\omega}{c} = \beta_0 + (\omega - \omega_0)\beta_1 + \frac{1}{2}(\omega - \omega_0)^2\beta_2 + \cdots + \frac{1}{m!}(\omega - \omega_0)^m\beta_m, \quad (2.1)$$

where both β_1 and β_2 are related to refractive index and its derivatives, given the

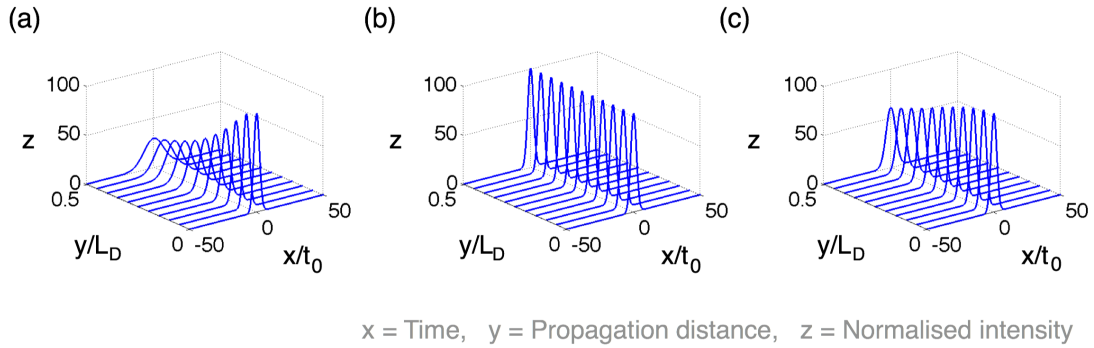

Figure 2.4: *Effects of GVD on the propagation of an unchirped Gaussian pulse. The modelled pulses have a pulsewidth of* 5 ps *(FWHM) and input pulse power of* 100 mW*. (a) Normal dispersion of* $D = -100\,\mathrm{ps\,km^{-1}\,nm^{-1}}$*. (b) Zero dispersion,* $D = 0$*. (c) Anomalous dispersion of* $D = 40\,\mathrm{ps\,km^{-1}\,nm^{-1}}$*.*

relationship in Equation 2.2:

$$\beta_m = \left(\frac{d^m\beta}{d\omega^m}\right)_{\omega=\omega_0} \qquad (m = 0, 1, 2, \dots). \tag{2.2}$$

The variable β_1 is defined as the reciprocal of group velocity and β_2 is the variable of most significance with regard to SC generation. The zero dispersion wavelength (ZDW or λ_D), where $\beta_2 = 0$, is the spectral position at which material dispersion and waveguide dispersion cancel each other out. The normal dispersion regime is the region in which $\beta_2 > 0$ where longer wavelengths travel faster. The anomalous dispersion regime is where $\beta_2 < 0$ and conversely shorter wavelengths travel faster. These regimes are indicated on the dispersion curves shown in Figure 2.3 for two different PCFs, one of which has normal GVD across all wavelength ranges (ND1064) and another which has normal dispersion at lower wavelengths and anomalous dispersion at higher ones (SC-5.0-1040). GVD acting on its own will always cause a pulse to broaden [Siegman, 1986], as shown for a Gaussian pulse in Figure 2.4 for different cases. Nonlinear effects can either act to reinforce this broadening, or in fact counter-act the broadening through pulse compression. A special case of the latter phenomenon are solitons, which are introduced in Section 2.3.3.

There is a minimum propagation distance required for the dispersion effects to

become significant in an optical waveguide. The characteristic dispersion length, L_{D} is given by Equation 2.3:

$$L_{\mathrm{D}} = \frac{T_0^2}{|\beta_2|}, \tag{2.3}$$

where T_0 is the full width at half maximum (FWHM) of the input pulse and β_2 is GVD parameter of the fibre, which is dependent on wavelength.

2.3.2 Nonlinearity

The Kerr effect is an optical nonlinear effect that describes the intensity dependence of refractive index as shown in Equation 2.4:

$$n_{\mathrm{tot}} = n + \Delta n = n + n_2 I, \tag{2.4}$$

where n is linear refractive index, n_2 is nonlinear refractive index and I is intensity of the light pulse. The overall result is that more intense light will have a larger refractive index and thus travel more slowly than less intense light. Waveguides and other dielectric materials exhibit a nonlinear response when subjected to high intensity fields. This manifests itself in an induced polarisation, p, which can be represented as a Taylor expansion:

$$p = \epsilon_0 \sum_n \chi_n E^n, \tag{2.5}$$

where E is the applied electric field, ϵ_0 is the permittivity of free space, χ_n is the n^{th} order susceptibility of the material. This polarisation is mainly due to the interaction of the applied field with weakly bound valence electrons in the material. The physical interpretation of these interactions is complex so discussion here is limited to the lowest order nonlinear effects, which for isotropic materials such as liquids is third order susceptibility, χ_3, a waveguide and material property [Boyd, 2003]. This term includes nonlinear effects such as third harmonic generation (THG), four wave mixing (FWM), Kerr effect, Raman scattering, multi-phonon absorption and self-phase modulation (SPM). A more detailed discussion of other effects is covered in the literature [Agrawal, 2001; Alfano, 2006].

The gamma factor, γ, is used to quantify nonlinearity in a fibre. It relates laser power to nonlinearity and is assumed to be uniformly distributed through the fibre mode:

$$\gamma = \frac{n_2 \omega_0}{c A_{\text{eff}}}, \tag{2.6}$$

where A_{eff} is the effective core area, n_2 is the nonlinear refractive index, c the speed of light and ω_0 the central frequency of the input pulse. Equation 2.6 shows that the nonlinearity of a fibre increases as the core size decreases.

The characteristic length scale for nonlinear effects to become significant, L_{NL}, is defined:

$$L_{\text{NL}} = \frac{1}{\gamma P_0}, \tag{2.7}$$

where P_0 is the peak power of the input pulse. The amount of nonlinearity experienced by a pulse of light will depend on the length of fibre it interacts with. The power of the pulse is also a factor, with pulses of increased peak power experiencing greater nonlinearity. As a result, pulses of higher peak powers have shorter L_{NL}, as can be calculated from Equation 2.7.

2.3.3 Phenomena in fibre-guided laser light

There are specific phenomena that can occur in optical fibres depending on their dispersive and nonlinear properties. A few key phenomena that feature in SC generation are introduced here.

Solitons

Solitons are "waves of translation" that propagate without changing shape. They were first observed as low amplitude waves in canals that did not dissipate energy [Rogers and Shadwick, 1982]. In optical applications solitons are formed when the effect of dispersion and nonlinearity (SPM) counteract. In the anomalous regime, shorter wavelengths travel faster than longer ones, but nonlinearity causes shorter wavelengths to travel more slowly. Solitons propagate when these two effects cancel each other out. This can be shown by considering both effects in first-

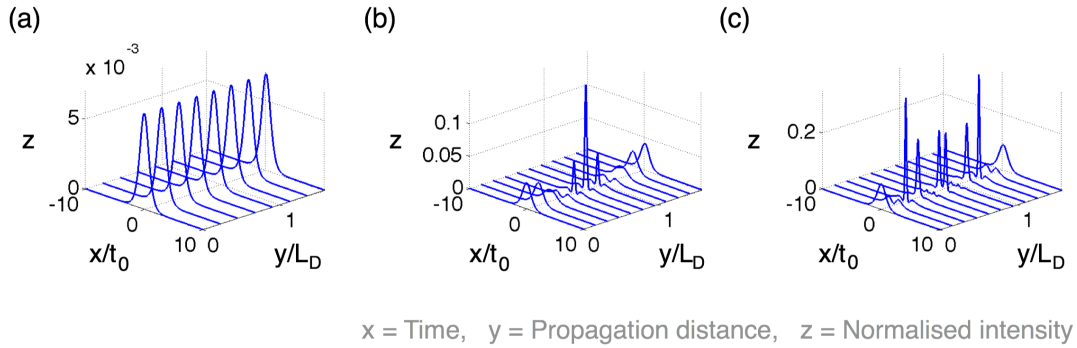

Figure 2.5: *Propagation of a sech^2 pulse with anomalous dispersion ($\beta_2 < 0$) for solitons of order N=1, 2 and 3. (a) $N = 1$, i.e. fundamental soliton, (b) $N = 2$ and (c) $N = 3$. The non-fundamental solitons are shown propagating over one soliton period, z_0.*

order and referring to the nonlinear Schrödinger equation (NLSE) [Mollenauer and Gordon, 2006]. The result shows that both nonlinearity and dispersion can be considered as complementary phase shifts, $d\phi(t)$, acting on a pulse. This result is derived in Appendix A.

Solitons are categorised by their soliton number, N, which can explain differences in propagation:

$$N^2 = L_D \gamma P_0 = \frac{\gamma P_0 T_0^2}{|\beta_2|}, \tag{2.8}$$

where T_0, P_0 are optical pulse parameters, and γ and β_2 are waveguide parameters. The propagation of three different soliton orders are shown in Figure 2.5. The fundamental soliton is for the case $N = 1$, as shown in Figure 2.5(a). It maintains its shape throughout propagation and does not experience spectral or temporal broadening [Mollenauer and Gordon, 2006; Satsuma and Yajima, 1974]. Higher order solitons undergo periodic spectral and temporal oscillations, but return to their original shape after propagating a characteristic soliton distance, z_0. This is shown in Figure 2.5(b) and (c) where $z_0 = \frac{\pi}{2} L_D$.

Raman Scattering

Most nonlinear effects involved in SC generation are elastic processes, i.e. those that do not involve energy transfer with the nonlinear propagation medium. Ra-

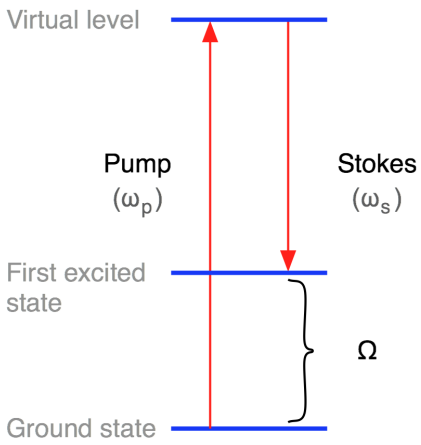

Figure 2.6: *Raman scattering energy level diagram. A pump photon (ω_p) undergoes a nonlinear interaction (e.g. a "collision" with the glass) shedding energy (Ω) and being scattered as a lower energy Stokes photon (ω_s).*

man scattering, on the other hand, is an inelastic process which involves the transfer of energy from the optical field (propagating electromagnetic wave) to the optical waveguide (dielectric material) [Raman and Krishnan, 1928]. A photon from the EM field interacts with the glass to create a lower frequency photon if the pump photon excites a vibrational state of a molecule in the nonlinear waveguide (see Figure 2.6). The scattered lower frequency so-called Stokes photon propagates in the same direction as the incident photon. Energy and momentum are conserved in this process.

Stimulated Raman scattering (SRS) is an efficient form of Raman scattering and requires a high intensity pump laser beam. This process occurs if the bandwidth of the soliton is greater than the Raman gain of silica and stimulated emission increases the rate of Stokes photons production [Agrawal, 2001]. The formation of Stokes frequencies at the expense of higher frequency components results in what is known as soliton self-frequency shift (SSFS) [Lee et al., 2008] and lends to the efficient production of longer wavelengths within the supercontinuum (laser pulse) creating a continuous spectrum.

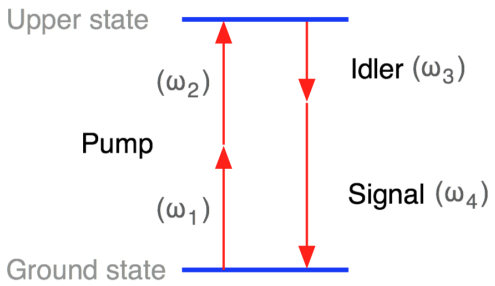

Figure 2.7: *Energy level diagram for degenerate four-wave mixing (FWM). Two pump photons (ω_1 and ω_2) interact to produce an idler photon, ω_3, and a signal photon, ω_4.*

Four-wave Mixing

Four-wave mixing (FWM) is an important nonlinear effect in SC generation because it can create new frequencies that are some distance from the pump frequency. In this process two photons, ω_1 and ω_2 interact and produce two new photons, one red-shifted (idler, ω_4) and one blue-shifted (signal, ω_3), as depicted in Figure 2.7. The process is possible when the energy and momentum (wavenumber) are conserved. Most fibres will support some FWM in the case of pulse break-up $\omega_1 = \omega_2$ (degenerate FWM). PCF is also able to support FWM for greatly different wavelengths, $\omega_1 \neq \omega_2$ and $\omega_4 >> \omega_3$, due to its specially "engineered" waveguide dispersion. This supports energy transfer from solitons to visible light [Skryabin and Yulin, 2005] and hence white light SC generation.

Dispersive Waves

Solitons that propagate close to the zero dispersion wavelength (ZDW) can transfer energy in the the normal regime to generate so-called dispersive waves which are occasionally referred to as "non-solitonic" or Cherenkov radiation [Akhmediev and Karlsson, 1995]. This effect comes about due to phase-matching between solitons and continuous waves in the normal dispersion regime [Skryabin and Yulin, 2005; Wai et al., 1986]. The generation of dispersive waves is crucial for spectral broadening, as it involves the transfer of high intensity in the infrared (IR) to the visible spectrum. This effect usually occurs close to the ZDW. Higher order solitons have increased spectral broadening and thus can be further from

the ZDW and still achieve the required overlap [Dudley et al., 2006].

A further effect of group velocity matching and cross-phase modulation can result in the trapping of a dispersive wave by a soliton. Dispersive waves begin with a lower group velocity than solitons. Soliton self-frequency shift (SSFS) causes solitons to slow down as they shift to longer wavelengths which allows the dispersive wave to catch up with the soliton. Interaction between the soliton and dispersive wave occurs when the group velocities are matched and the resultant FWM process shifts the blue edge of the dispersive wave to even shorter wavelengths. This process repeats itself. Solitons that have been shifted further into the IR by SSFS go on to trap dispersive waves that have been further blue-shifted through dispersive wave trapping [Genty et al., 2004; Gorbach and Skryabin, 2007a; Nishizawa and Goto, 2002].

2.3.4 Photonic crystal fibre pumping

Different types of lasers have been used for pumping PCF. Mode-locked titanium-sapphire (Ti:sapph) lasers were initially required as pump laser sources [Birks et al., 2000; Ranka et al., 2000; Wadsworth et al., 2002]. Fibre lasers were then introduced as more compact alternatives that are simpler to operate and less expensive [Rulkov et al., 2005; Urquhart, 1988].

Further advancements in PCF design and dispersion engineering are leading towards fibres better tailored to pump sources and offering new opportunities in spectral and/or temporal output to be realised [Dudley and Taylor, 2009]. PCFs with all-normal GVD profiles (c.f. ND1064 dispersion profile in Figure 2.3) have been demonstrated for generating supercontinua [Heidt et al., 2011; Hooper et al., 2011]. All-normal GVD fibres have better noise characteristics but much narrower spectral outputs. The output of the fibre shown in Figure 2.3, for instance, extends to around only 650 nm in the visible. These fibres are still a relatively new area of PCF research and not yet commercially available. Anomalous GVD fibres on the other hand can be readily purchased, as can complete "turn-key" SC systems which use such fibres [Savage, 2009]. Therefore, the discussions in the rest of this chapter focus on anomalous GVD PCF.

One of the main features of SC generated from PCF pumped in the anomalous

group velocity dispersion regime (i.e. $\lambda >$ ZDW) is the generation of solitons. Solitons entail high-intensity light propagating long distances along PCF. This enables individual pulses to experience more nonlinear interactions as they interact with PCF for a longer period of time. The end result is a broader SC output. The exact nature of the SC generated also depends on pulse length. Pump laser sources used in this work have relatively long pulses (>1 ps). These types of lasers have high soliton orders ($N > 500$). High-order solitons can undergo soliton fission which leads to spectral broadening in the IR. The combination of these and other solitonic processes result in broad SC, almost spanning the entire transparent window of silicon and high average powers. As previously mentioned, the major trade-off with SC generated from anomalous GVD PCF is the reduced temporal coherence, leading to greater pulse-to-pulse variation.

2.4 Modelling nonlinearity and dispersion

As part of this research, SC simulations were performed based on the established Fourth-Order Runge-Kutta interaction picture method (RK4IP) developed by Hult [2007] of the Laser Analytics Group, using more recent algorithm written by co-workers in the group [Liu et al., 2010, 2012] and implemented in MATLAB (Mathworks, USA). The fibre and pump laser parameters required for the simulation are listed in Table 2.1.

Table 2.1: *Input pump laser and PCF parameters for RK4IP simulations.*

Symbol	Input pulse parameter	Units
λ_0	Centre wavelength	nm
P_0	Peak power	W
T_0	Pulse width (FWHM)	ps
Symbol	**Fibre parameter**	**Units**
γ	Nonlinear coefficient	$\mathrm{W^{-1}\ m^{-1}}$
$R(t)$	Nonlinear response function	
τ_{shock}	Self-steepening timescale	fs
β_k	Dispersion coefficients at λ_0 ($k =$ order)	$\mathrm{ps^{k}\ km^{-1}}$

Simulations and Spectrograms

It is difficult to isolate individual phenomena which is why spectrograms are useful tools for visualising the interplay between nonlinearity and dispersion. They represent snapshots of the spectral and temporal state of a laser pulse at a particular position along the optical fibre and can help aid the understanding of very complex interdependent processes. The pulse parameters input into the RK4IP simulation were for a 5 ps unchirped Gaussian pulse with a 100 ps FWHM, 100 W input peak power, centred at 1060 nm. The fibre parameters for a 26 m PCF with zero dispersion at 1055 nm were taken from Dudley et al. [2008]. Interpretation of the resultant spectrograms shown in Figure 2.8 is given below:

(a) *Input pulse*: A high power monochromatic laser pulse is injected into the fibre at the zero dispersion wavelength (ZDW), leading to propagation. The pulse then propagates seemingly unperturbed for the first 3 m of fibre.

(b) *Creation of sidebands and pulse disintegration*: Parametric sidebands are formed due to four-wave mixing (FWM) in the frequency domain. Phase matching in fibres enables efficient energy exchange. This requires low anomalous dispersion and high nonlinearity. The new frequencies are created as two identical photons create a new frequency up-shifted "signal" photon and a frequency down-shifted "idler" photon. This process is equivalent to modulation instability (MI) in the time domain, where the steady state interplay between nonlinear and dispersive effects causes pulse disintegration as FWM is phase-matched by self-phase modulation (SPM) [Potasek and Agrawal, 1987].

(c) *Formation of solitons and dispersive waves*: The sidebands formed in the previous stage are strengthened. Since the input pump pulse is pumped at the ZDW, the sidebands are thus formed in both the normal and anomalous regions. Solitons are formed on the long wavelength side (nonlinearity and dispersion cancel each other out) and dispersive waves on the short wavelength side (where both nonlinearity and dispersion result in temporal broadening). In terms of solitons, the modulation frequency, $\Delta\omega_{\mathrm{MI}}$, is given as:

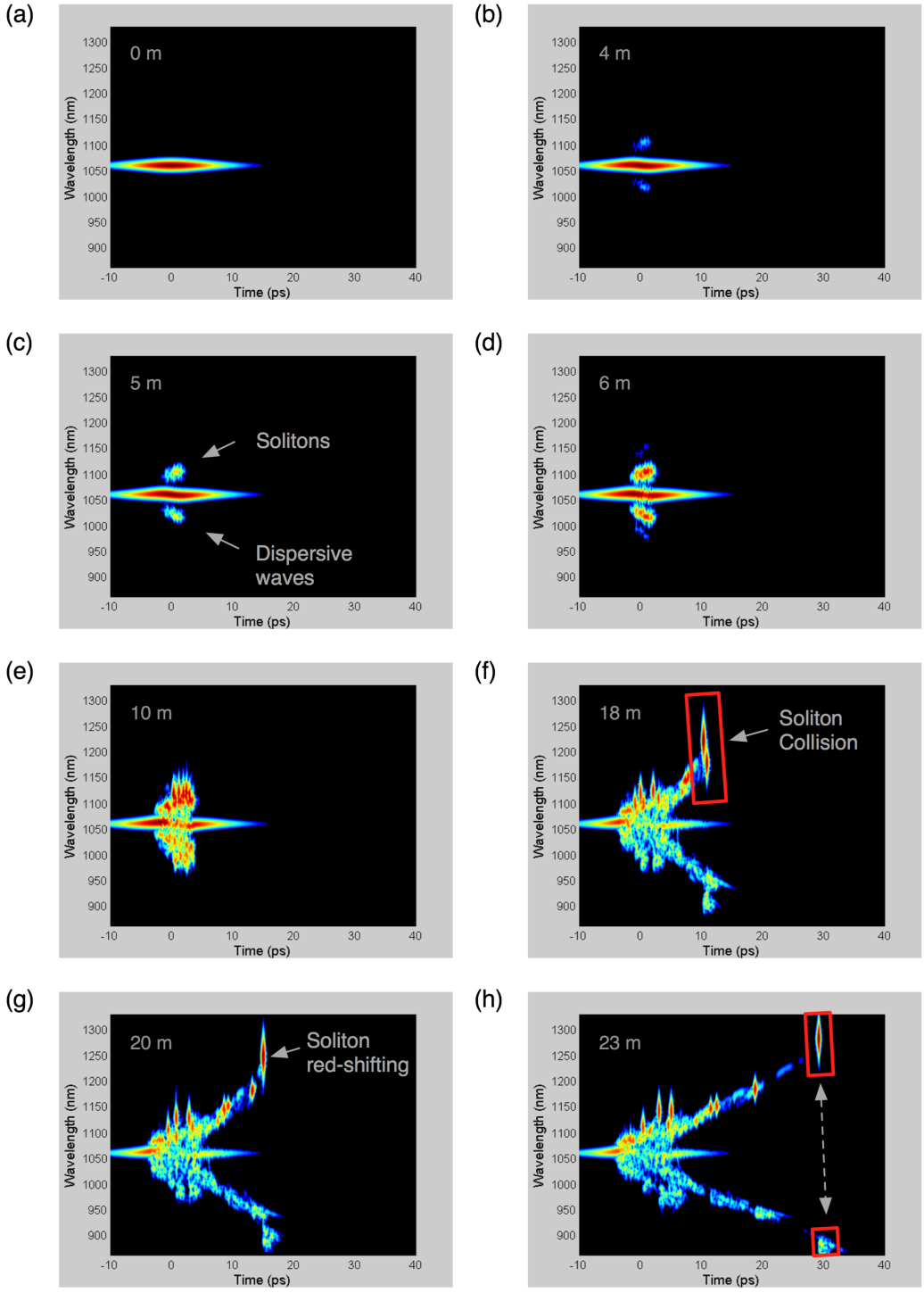

Figure 2.8: *Spectrograms of the spectral and temporal evolution of a* 5 ps *pulse along a* 26 m *anomalous PCF. (a) Input pulse. (b) Creation of sidebands and pulse disintegration. (c) Formation of solitons and dispersive waves. (d) Further soliton fission. (e) Soliton turbulence. (f) Soliton collision. (g) Raman scattering and red-shifting of solitons. (h, and f-h) Pulse breakup and dispersive wave trapping.*

$$\Delta\omega_{\mathrm{MI}} = \sqrt{(2\gamma P)/(|\beta_2|)}, \tag{2.9}$$

where P is the pump power and the maximum side-band gain is $2\gamma P$. The soliton duration (FWHM) can be related to the period of MI, T_{MI}, in the time domain, which is $T_{\mathrm{MI}} = 2\pi/(\Delta\omega_{\mathrm{MI}})$. Shorter solitons are created when the MI period is short, more specifically $\sim T_{\mathrm{MI}}/5$ [Islam et al., 1989; Travers, 2010].

(d) *Further soliton fission*: The splitting up of high-order solitons into multiple fundamental solitons is termed soliton fission. The characteristic length over which soliton fission occurs L_{fiss} is dependent on the characteristic dispersion length, L_{D}, and the soliton order, N, as follows: $L_{\mathrm{fiss}} \sim L_D/N$. This increases with pump pulse duration which means that the effects of MI/FWM dominate the initial propagation stage.

(e) *Soliton turbulence*: Solitons enter a regime of soliton turbulence as different packets of light bounce off each other to cause the broadening observed in the spectrogram. Energy is sometimes lost to Raman scattering in otherwise elastic collisions.

(f) *Soliton collision*: Solitons in the anomalous regime can experience collisions. This strengthens the high intensity soliton and weakens the low intensity soliton. This process is termed cross-Raman scattering in the temporal domain [Frosz et al., 2006; Islam et al., 1989; Korneev et al., 2008]. Interestingly, solitons travelling near the ZDW can transfer some energy to the normal regime to a dispersive wave through spectral overlap. This enables spectral power to build up in the normal dispersion regime [Akhmediev and Karlsson, 1995; Gorbach et al., 2006; Karpman, 1993; Skryabin and Yulin, 2005; Wai et al., 1986].

(g) *Raman scattering and red-shifting of solitons*: Soliton bandwidths overlap with Raman gain and thus the long wavelength solitons undergo Raman self-frequency shift causing the long wavelength edge to broaden [Dianov and Mamyshev, 1985; Mussot et al., 2009]. This is another process involving

self-phase modulation (SPM) and highlights the need for sufficient soliton duration to enable temporal overlap with the Raman gain spectrum.

(h) *Pulse breakup and dispersive wave trapping*: Group velocity matching and cross-phase modulation (XPM) can cause interactions between spectral components in different regimes. Blue dispersive waves become trapped behind solitons [Beaud and Hodel, 1987; Genty et al., 2004; Gorbach and Skryabin, 2007a,b; Nishizawa and Goto, 2002]. Raman red-shifting causes the solitons to slow down forcing the trapped dispersive waves to also slow down, resulting in further blue-shifting. This process is key to the formation of broad bandwidth supercontinuum spectra [Stone and Knight, 2008].

The efficient generation of SC requires a balance of low anomalous dispersion and high nonlinearity. The spectrograms in Figure 2.8 show that extremely broad SC generation requires soliton interactions, which necessitates pumping of PCF in the anomalous regime. For the creation of dispersive waves and spectral overlap, one needs to pump near the ZDW. The final stages of dispersive wave trapping require group velocity matching of the two spectrally dispersed edges. All these requirements can be satisfied through careful PCF design and optimised through modelling.

Current Limitations in SC Generation

There are two main limitations that may affect spectroscopic measurements from SC generated light:

(i) *Spectral bandwidth*: Limitations in spectral intensity in required wavelength range.

(ii) *Pulse variation*: Pulse-to-pulse intensity fluctuations can introduce noise for intensity-based measurements.

Material constraints also limit the broadening of supercontinua. As previously mentioned, PCF is typically drawn from silica preforms (c.f. Figure 2.9). Silica electronic absorption in the UV limits spectral dispersion at the blue edge. In the

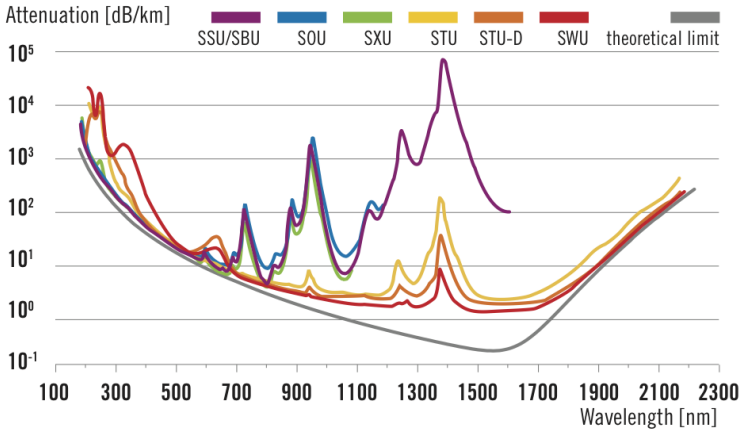

Figure 2.9: *Fibre attenuation curves for fused silica core step-index multimode preforms from the UV to near-IR. The SSU, SBU, SXU and SOU fibres are undoped, high OH^- pure silica cores with improved UV transmission. STU, STU-D and SWU are low OH^- (<0.7 ppm) silica preforms. Fibre cladding is pure silica with the exception of fluorine-doped silica for STU and STU-D preforms. The overall theoretical attenuation limit is also shown. Figure reproduced from manufacturer datasheet [Heraeus Quarzglas, 2012].*

IR, the main limitation is OH^- ion absorption, specifically at 2.7 µm. Water molecules and other contaminant can get "frozen in" during PCF fabrication, which is why dopants are normally added to mitigate this. Preform cores are generally treated with chlorine during fabrication to reduce OH^- content. However, the addition of some dopants such as Cl^- ions can also limit the blue edge due to the introduction of chlorine absorption bands in the UV. As such, different glass compositions are used to suit different requirements, as shown in Figure 2.9.

SC generated from anomalous regime pumping of PCF have very broad spectra produced by processes that involve solitons and that are seeded by noise. Such processes are sensitive to pump laser fluctuations and result in large pulse-to-pulse variation in spectral structure [Dudley and Coen, 2002]. Signal averaging of multiple pulses has been shown to wash out these single-shot spectral pulse variations [Gu et al., 2002], although this increases the times required for signal acquisition.

2.5 Summary: Supercontinua for optical sensing

The underlying physics behind SC generation has been discussed in this chapter in order to provide a better understanding of its properties. In summary, there are four key attributes that make SC radiation suitable for optical metrology:

(i) Extreme spectral bandwidths greater than 1000 nm with potential to cover the entire transparent window of silica glass (300 nm to 2.4 µm).

(ii) High spatial coherence, directionality and brightness like a laser source.

(iii) Very high spectral power densities of 1 mW/nm and even up to 50 mW/nm [Travers et al., 2007].

(iv) Pulsed character, enabling advanced time-resolved measurement techniques using, for example, picosecond SC sources modelled in this chapter.

The past decade has seen the application of SC radiation in a number of well-established metrological techniques, demonstrating its potential, such as optical coherence tomography [Hartl et al., 2001], confocal fluorescence microscopy [Dunsby et al., 2004; Frank et al., 2007; McConnell, 2004], high speed gas sensing [Kelkar et al., 1999; Sanders, 2002; Watt et al., 2008] and open-path remote atmospheric analysis [Kasparian et al., 2003]. The motivation here is to now use SC radiation as an incoherent light source for liquid-phase absorption spectroscopy, specifically cavity-enhanced techniques.

Chapter 3

Optical Cavities for Liquid Spectroscopy

3.1 Motivation: Increasing absorption spectroscopy sensitivity

Optical cavities offer a different approach to traditional single-pass absorption techniques in that light passes through the sample multiple times. This acts to increase the optical path length. Whilst theoretically attractive, there are practical consequences, as it requires the introduction of two high reflectivity mirrors (which form the cavity) into the optical path. This reduces the amount of light reaching the detector, placing additional demands on detector sensitivity. Light must also be effectively coupled into the cavity, which might place constraints on the types of light sources that can be employed. Although optical cavities have been widely employed in the gas phase, there are only a limited number of investigations in the liquid phase demonstrated in the liquid phase. There are different challenges in the liquid phase in terms of increased optical density, higher background losses and broader spectral features. These factors must be taken into consideration to determine whether optical cavity techniques can offer similar sensitivity enhancements for the liquid phase, as they do with the gas phase. In this chapter, calculations are made and results plotted to model the effects of liquid absorption for different optical cavities. The aim is to provide some

theoretical context to the design decisions made in the forthcoming experimental chapters.

Chapter Summary

The chapter begins with an introduction to single-pass absorption spectroscopy as used for quantitive absorption measurements before introducing multi-pass techniques under which cavity-enhanced methods fall. Cavity ring-down spectroscopy (CRDS) and cavity enhanced absorption spectroscopy (CEAS) are then introduced in the context of liquid-phase absorption measurements and the background theory provided.

3.2 Current spectroscopic techniques for liquids

3.2.1 Single-pass absorption

Commercial spectrophotometers commonly employed by scientific researchers use single-pass absorption for analysis. The technology is fairly mature, with single-pass measurements taken using a white light source which most commonly is an incandescent lamp. A monochromator is used to filter selectively the light after it has been transmitted through the absorbing sample. It is then possible to build up a broad bandwidth spectrum through sequentially scanning across the desired wavelength region. The sample under investigation is held within standard cuvettes through which the light is passed. Standard cuvettes usually come with a fixed optical sample pathlength of 1 cm and even 2 mm in cases.

The absorption in single-pass measurements is calculated using the Beer-Lambert law (Equation 3.1). The wavelength-dependent absorption coefficient $\alpha(\lambda)$ is calculated for the transmitted intensity, I, and the incident intensity, I_0, from:

$$I(\lambda) = I_0(\lambda) \exp(-\alpha(\lambda)d), \tag{3.1}$$

where d is the sample absorption pathlength. The absorption coefficient is a function of concentration, C, related by the molar extinction coefficient, ϵ, via

$\alpha(\lambda) = \epsilon(\lambda)C$. Rearranging Equation 3.1 in terms of the absorption coefficient gives:

$$\alpha(\lambda) = -\frac{1}{d}\ln\left(\frac{I(\lambda)}{I_0(\lambda)}\right) \approx \frac{1}{d}\left(1 - \frac{I(\lambda)}{I_0(\lambda)}\right). \tag{3.2}$$

Weak absorptions in liquids ($1 - \frac{I}{I_0} < 10^{-3}$) are difficult to detect with conventional techniques, due to the low signal-to-noise ratios (SNR). Absorption measurements require the detection of a small change in intensity ($I_0 - I$) over a large background (I_0). Options to increase measurement sensitivity are either to suppress (or filter) the detection noise, or to extend the absorption pathlength. Equation 3.1 shows that an increase in pathlength would result in a larger intensity difference and thus improve the sensitivity of the measurement to above any SNR limit.

3.2.2 Multi-pass configurations for pathlength increases

It is possible to extend the effective pathlength through multi-pass configurations. The result of such an approach is evident from Beer-Lambert (see Equation 3.1) where an increase in pathlength is proportional to an increase in absorption signal. The earliest multi-pass cells were introduced by White [1942] and Herriott and Schulte [1965] in the mid 20^{th} century, the principle of which is shown schematically in Figure 3.1(a). The light beam is passed through a small hole in a mirror and it then traces a path around the cell as it is reflected between the mirrors. The beam then exits through one of the mirrors, having passed through the sample a multiple number of times. The alignment of the concave mirrors dictates the beam path, with effort made to ensure the beam does not overlap itself on the mirror face as this leads to optical interference. Optical interference in multi-pass cells comes in the form of cross-talk. Light beams passing through White cells built using mirrors of lower reflectivity experience higher transmission losses per pass. Cross-talk in this case would be particularly extreme if an intense entry beam were to interact with a weaker output beam leading to signal fluctuations [White, 1942]. Light from multiple lasers can be passed through the

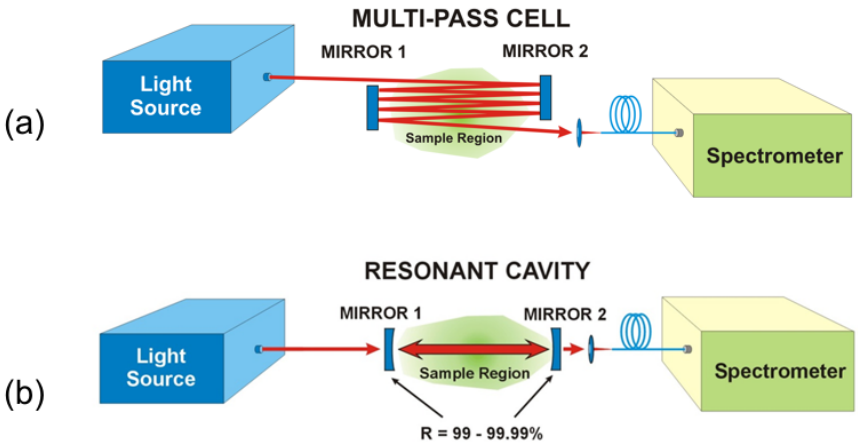

Figure 3.1: *Methods of increasing absorption length and thus sensitivity of absorption measurements, compared to single-pass* 1 cm *standard cuvette measurements. (a) Multi-pass cell arrangement, which can offer* 10 m *to* 100 m *absorption lengths. Light beams trace unique paths through the cell. (b) Line-of-sight resonant optical cavity which can offer* 100 m *to* 10 000 m *absorption lengths, based on the chosen mirror reflectivity pairings. Light beams travel along the same axis.*

same Herriott cell as long as each beam traced a unique path. Path overlap of different lasers beams or interference fringes on the mirror surfaces would also result in unwanted cross talk [Herriott and Schulte, 1965; Tarsitano and Webster, 2007]. Another issue is the drop in cavity transmission as the number of passes increases. The overall enhancement is primarily limited by the finite number of unique passes that can be made without overlap for a given cavity mirror.

Optical resonators (see Figure 3.1(b)) can achieve even greater number of passes than multi-pass cells. Dielectric mirrors, which have a much higher reflectivity than the metallic mirrors used in multi-pass cells, are used to achieve longer pathlengths. These so-called cavity-enhanced techniques are normally based on linear optical cavities in which the input beam traces the exact same path as it is reflected back and forth within the cavity. This means the effective pathlength is proportional to the reflectivity values of the mirrors. This linear optical resonator approach is now more commonly employed in recently published work due to the smaller sample volumes that are required and larger

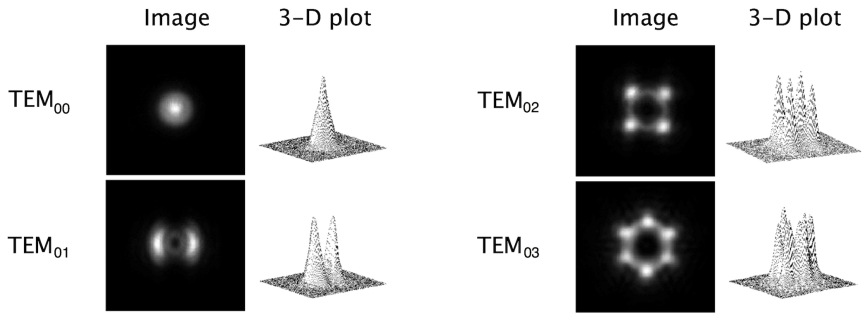

Figure 3.2: *Representation of Laguerre-Gaussian TEM mode intensity profiles along with corresponding 3D intensity distribution plots. Figure adapted from Ishaaya et al. [2003].*

effective pathlengths obtainable in comparison to multi-pass Herriott and White cells [Berden and Engeln, 2009].

3.3 Optical cavities

Optical cavities are able to support certain solutions of the electromagnetic (EM) wave equation [Kogelnik and Li, 1966]. The transverse and longitudinal modes of light waves are mathematically represented by Laguerre-Gaussian polynomials for cylindrical geometries [Siegman, 1986], TEM_{pl}, where l and p are azimuthal and radial mode indices respectively [Arlt and Padgett, 2000].

Longitudinal modes are important in describing the waves that can be supported within the cavity, in specific relation to the wavelength of resonant light. Figure 3.2 shows the spatial intensity distributions of four transverse modes, with the "fundamental" transverse mode (TEM_{00}) having a near Gaussian distribution. TEM_{00} has much lower diffractional losses than the larger higher order modes [Yariv, 1997], and, where necessary, can be preferentially excited through the use of mode matching optics (where TEM_{00} is chosen to match the intra-cavity beam dimensions, c.f. Figure 3.3).

Fabry-Perot resonator theory states that optical cavities formed of low loss mirrors will produce a comb-like interference pattern for the cavity transmission in the form of an Airy function [Born and Wolf, 1999]. The resonance condition is established when an integer number of wavelengths matches the cavity roundtrip

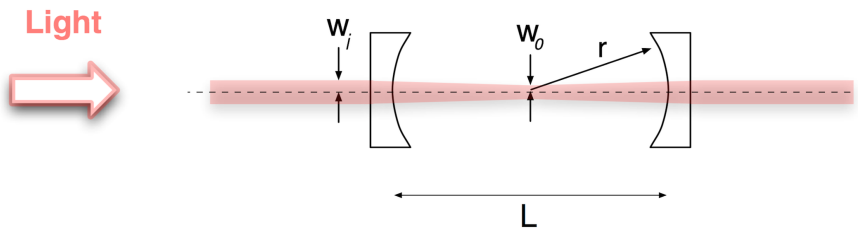

Figure 3.3: *Cavity parameters and Gaussian beam dimensions for cavity-enhanced optical set-ups. Radius of incident light beam on rear-side of first cavity mirror, w_i, minimum intra-cavity beam radius, w_0, mirror radius of curvature, r,and cavity length (i.e. mirror separation), L, are shown. The cavity is comprised of two plano-concave mirrors aligned along one axis in this "line-of-sight" scheme.*

length, $q\lambda = 2L$, where L is the cavity length (i.e. mirror separation) and q is the integer longitudinal mode order. Two adjacent cavity comb elements (i.e. q, $q+1$) are separated in frequency space by the free spectral range (FSR, $\Delta\nu_{\mathrm{FSR}}$) given by:

$$\Delta\nu_{\mathrm{FSR}} = \frac{c}{2nL} = \frac{1}{t_r}, \tag{3.3}$$

where n is the refractive index of the medium inside the cavity, c is the speed of light and t_r is the cavity roundtrip time. The ability of a cavity to maintain constructive interference for long periods of time is governed by the cavity finesse, F:

$$F = \frac{\pi\sqrt{R}}{1-R}, \tag{3.4}$$

where R is mirror reflectivity. The finesse is related to the linewidth of the cavity comb $\Delta\nu_c$ by Equation 3.5. $\Delta\nu_c$ defines the spectral resolution (FWHM) and is shown for $R = 40\%$ in Figure 3.4. Cavity finesse is plotted in Figure 3.4 for cavities with mirrors of different reflectivity. The modelled results show a decrease in cavity mode linewidth $\Delta\nu_c$ with a corresponding increase in mirror reflectivity.

$$\Delta\nu_{\mathrm{c}} = \frac{\Delta\nu_{\mathrm{FSR}}}{F}. \tag{3.5}$$

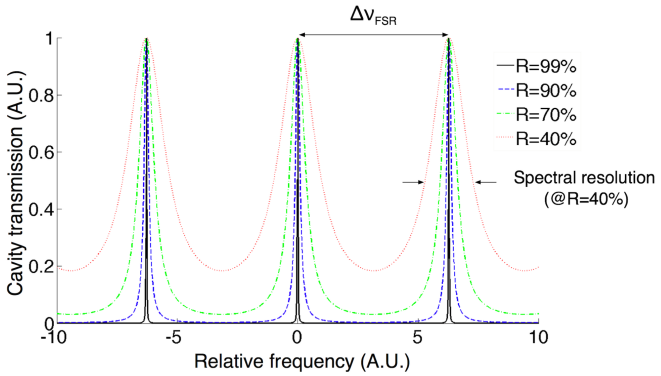

Figure 3.4: *Cavity transmission modelled on the Airy function for two-mirror optical cavities. Mirror reflectivity values of R =*40 %*,* 70 %*,* 90 % *and* 99 % *were modelled. The spectral resolution,* $\Delta\nu_c$*, is shown for* $R = 40\%$*.*

Another consideration relates to the confinement of light within the cavity. Light can be lost from the cavity by diffraction due to the finite size of mirrors. Therefore, an optically stable cavity must enable the refocusing and most importantly, confinement of light within the resonant cavity [Kogelnik and Li, 1966]. The criterion originating from optical Gaussian beam theory for a two-mirror cavity is:

$$0 < \left(1 - \frac{L}{r_1}\right)\left(1 - \frac{L}{r_2}\right) < 1, \tag{3.6}$$

where r_m (where m=1 or 2 for the respective mirror) is mirror radius of curvature and L the cavity length (i.e. mirror separation).

Mode Matching vs. Mode Washout

Maximum transmission of light through a cavity occurs when laser frequencies fully overlap cavity modes. This approach was taken in early cavity-enhanced methods [Newman et al., 1999; Romanini and Lehmann, 1993] by ensuring that laser light was coupled to the fundamental cavity mode (TEM_{00}) for the most efficient laser coupling (see Figure 3.5(a)). The throughput, or transmission T, at a given wavelength is dependent on the overlap of the laser linewidth $\Delta\nu_{\mathrm{L}}$ with the corresponding cavity comb mode $\Delta\nu_{\mathrm{c}}$ according to the relationship $T = \Delta\nu_{\mathrm{c}}/\Delta\nu_{\mathrm{L}}$

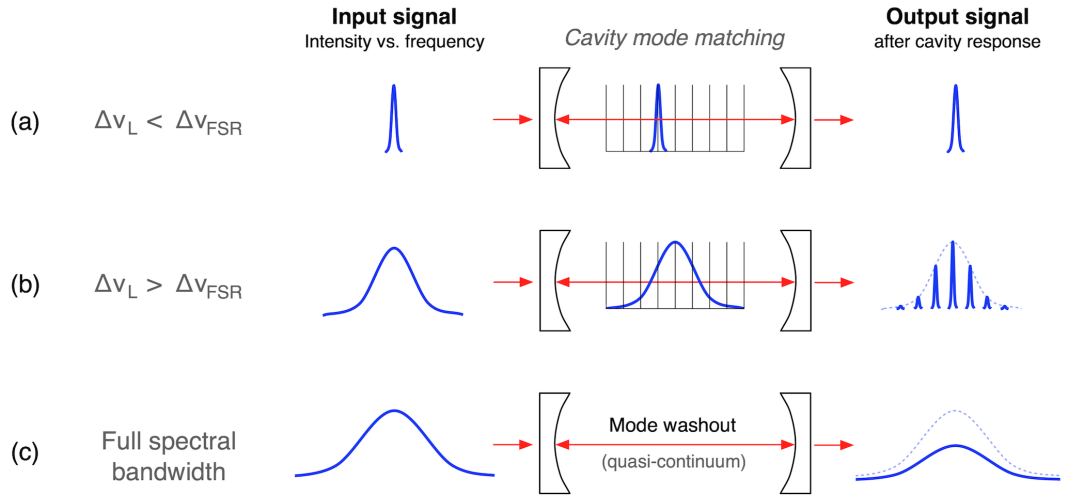

Figure 3.5: *Schematic illustrating optical cavity and laser comb coupling schemes. (a) Single laser frequency locking to one cavity mode, where $\Delta\nu_L < \Delta\nu_{FSR}$. (b) Mode matching: Locked coupling of frequency comb to cavity comb, where $\Delta\nu_L > \Delta\nu_{FSR}$. Intra-cavity dispersion results in inefficient mode matching away from the central locking frequency producing a narrower spectrum. (c) Mode washout: The defined cavity mode structure is "washed out" by the excitation of multiple higher order modes leading to a dense quasi-continuous cavity mode structure. Light is coupled at every wavelength and thus the full spectral bandwidth of a light source ($\Delta\nu_L \gg \Delta\nu_{FSR}$) is transmitted, but the intensity throughput is low.*

[Tittel et al., 2003]. Note that this is true only for cases where $\Delta\nu_{\mathrm{L}} < \Delta\nu_{\mathrm{FSR}}$. It is necessary to match not only the spacing of individual comb elements, but also absolute positions for the cavity modes and laser comb frequencies [Adler et al., 2010]. This can be achieved using laser frequency combs (LFCs). These are special mode-locked lasers that produce pulse trains of broad spectral bandwidth which are evenly spaced in the frequency domain [Schliesser et al., 2012]. The laser linewidth may be broad enough to overlap a number of cavity modes. In such cases $\Delta\nu_{\mathrm{L}} > \Delta\nu_{\mathrm{FSR}}$. The degree of overlap dictates the transmitted intensity, as shown in Figure 3.5(b).

Mode-matching can be achieved by either adjusting the frequency comb of the laser or modulating the external cavity itself. The cavity mode structure is dependent on its geometry. Therefore, it is possible to alter certain parameters

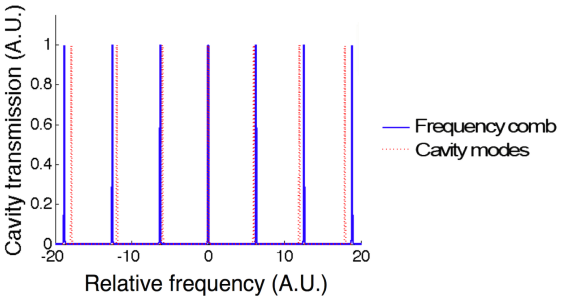

Figure 3.6: *Temporal walk-off as a result of intra-cavity dispersion. The simulation shows a phase-dependent frequency mismatch between the laser frequency comb and cavity modes which is defined as "walk-off".*

by adjusting the cavity, for example controlling the FSR by altering the cavity length. This method immediately increases the complexity of such a technique as it requires fine control of the cavity through the use of piezoelectric actuators and also a feedback loop system for accurate locking. At present only a few optical labs in the world have the technology and expertise to implement this technique.

The ability to match a laser comb to cavity modes over a broadband spectral range is further complicated by intra-cavity dispersion. The longitudinal mode spacing within the cavity is no longer described by a fixed free spectral range (FSR, c.f. Equation 3.3). Instead, it takes into account a frequency-dependent phase shift, $\phi(\omega)$, introduced by cavity mirrors, where $\omega = 2\pi\nu$ [Lehmann and Romanini, 1996]:

$$\Delta\nu_{\mathrm{FSR}}(\omega) = \frac{c}{2n(\omega)L + c\frac{\partial\phi}{\partial\omega}\big|_{\omega_0}}, \tag{3.7}$$

where L is cavity length, n is refractive index, c is the speed of light and ω_0 the centre frequency. The second term in the denominator, $\frac{\partial\phi}{\partial\omega}$, is the contribution from intra-cavity dispersion and causes the mismatch between the laser comb and cavity modes, also known as "temporal walk-off"[Peters et al., 2009]. This mismatch increases with distance away from ω_0, shown in Figure 3.6, thus placing a practical limit on the broadband spectral range for effective mode matching. Furthermore, the presence of a sample alters the effective cavity mode spacing and this effect is greater in the liquid phase than for gases.

An alternative method to mode-matching is called "mode washout" and it involves the excitation of not one but many transverse modes resulting in a complex mode spectrum. Previous techniques avoided manipulation of the cavity mode structure. The reasoning behind this is two-fold. First, if a narrow molecular absorption line fell between the cavity mode structure, it would be absent from the resultant spectrum. Secondly, it was deemed necessary to match the frequency comb produced by the laser to the cavity mode structure in order to couple light in.

The mode washout approach deliberately manipulates the cavity mode structure in order to excite multiple higher order transverse modes that fall between the longitudinal mode spacing. This has the effect of "filling in" gaps in the cavity mode spectrum to create a dense quasi-continuum. As a result, there are cavity modes at every wavelength and thus the full spectral bandwidth of a light source can be coupled in and transmitted. This is shown schematically in Figure 3.5(c). All absorption features within this spectral range will be detected and there will always be a cavity mode under every spectral position. Mode washout is simple to achieve, as the two criteria are for the cavity to be stable (see Equation 3.6) and the mirror separation to be any length that is not confocal (i.e. $L \neq r_1 + r_2$), as shown in Figure 3.7 taken from Meijer et al. [1994].

Whereas mode-locked techniques require precise control of the optical cavity, mode washout cavities have much lower mechanical stability requirements. Slight fluctuations in cavity length, for instance, would only act to excite more transverse cavity modes and thus increase the density of the cavity mode spectrum. Meijer et al. [1994] showed the quasi-continuum mode structure and compared it to the confocal arrangement. They also noted that the requirement of high reflectivity mirrors is relaxed for this case. Furthermore, high precision lasers with frequency combs are not required and, as a result, non-pulsed coherent and incoherent light sources, such as LEDs and lamps, can be used. The main downside of the mode washout approach is that the resultant intensity of light transmitted out of the cavity is much lower than in a mode-matching scheme as cavity modes are not actively matched and Fabry-Perot theory collapses [Lehmann and Romanini, 1996; Zalicki and Zare, 1995]. Consequently, sources of high spectral intensity per unit wavelength are used.

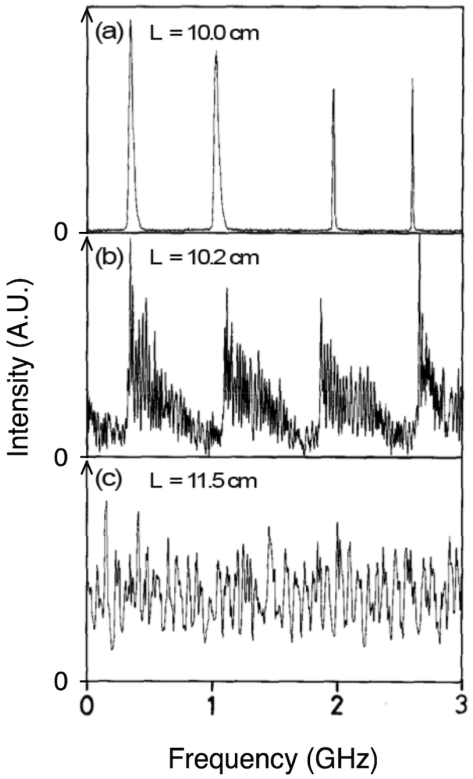

Figure 3.7: *Creation of a quasi-continuous mode structure with mirror separations (L) with non-confocal cavity geometries. (a) Mode spectrum for a confocal cavity, where L =10.0 cm. (b) Mode spectrum of a cavity slightly detuned from confocal (L =10.2 cm) resulting in the excitation of transverse modes. (c) Very dense mode spectrum for an intra-cavity length for non-confocal geometry (L =11.5 cm). Figure reproduced and adapted from Meijer et al. [1994].*

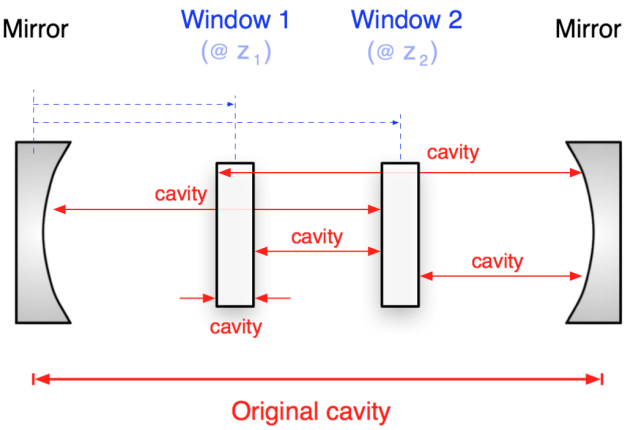

Figure 3.8: *Intra-cavity windows creating "cavities within a cavity". Optical interfaces within the original cavity act as low reflectivity mirrors creating multiple internal cavities, some of which are depicted in the schematic diagram above. The distance between windows 1 and 2 defines the intra-cuvette sample pathlength.*

Effect of "Cavities within a Cavity"

Liquid sensing using optical cavities may require additional optics for sample containment. Liquid samples are commonly held in glass cuvettes whereas gas samples are frequently in direct contact with cavity mirrors. For liquids this could lead to an added complication, as light retro-reflected off the first cuvette window would in theory create another optical cavity within the original cavity. The original cavity could then be considered as three Fabry-Perot resonators coupled to each other. The introduction of any additional cavity windows would amplify the effect creating multiple smaller cavities within a cavity, as shown in Figure 3.8.

Fabry-Perot theory is required to study the implications of etalon effects on the cavity mode structure. The equation for the resonant modes of the optical cavity is [Hodges et al., 1996]:

$$\nu_{qpl} = \frac{c}{2L}\left(q + \frac{(p+l+1)}{\pi}\arccos\sqrt{g_1 g_2}\right), \tag{3.8}$$

where q is the longitudinal mode index, p and l are transverse mode indices as defined at the start of Section 3.3, c is the speed of light in a vacuum, L is cavity

length and $g_i = 1 - (L/r_i)$, where r_i (for $i = 1, 2$) is radius of curvature for each respective mirror.

Trace gas sensing requires optical cavities of high finesse, and thus mirrors of high reflectivity, in order to achieve the required resolution [Ball and Jones, 2003]. Mirrors of lower reflectivity can be used for liquid sensing, such as the pair modelled in Figure 3.9. The cavity mode structure of TEM_{00} in a two-mirror cavity of length 30 cm and mirror reflectivity $R = 99.0\%$ is shown in Figure 3.9(a).

Figure 3.9(b) shows the case of a cavity window creating two separate cavities of length 10 cm and 19.5 cm, inside the original cavity. The window is assumed to be a low-reflectance mirror, with a reflectivity value of $R = 4.0\%$ (c.f. Fresnel's law in [Hecht, 2002]). Both cavities are modelled as having a mean reflectance of $R = 51.5\%$. Figure 3.9(c) plots the previous three profiles along with the broad transmission profile of an intra-cuvette cavity.

The results plotted in Figure 3.9 show that etalon effects act to create a dense cavity transmission profile across the frequency range. Results for the fundamental mode only have been plotted in each case, for simplification. The presence of higher order modes and other etalons not depicted in Figure 3.9 will further contribute to the "mode washout" phenomenon. This would not be suitable for a frequency comb method. However, the build up in mode structure and the collapse of Fabry-Perot theory is beneficial in the case of cavity-enhanced techniques to be developed in this thesis.

3.4 Theory of cavity-enhanced techniques

3.4.1 Cavity ring-down spectroscopy

Cavity ring-down spectroscopy (CRDS) was first employed as a method for measuring mirror reflectivity [Anderson et al., 1984; Herbelin et al., 1980], before being adopted as a stand-alone method for absorption measurements [O'Keefe and Deacon, 1988]. The technique involves the injection of a short pulse into an optically stable resonator of high finesse. Only a small fraction of this pulse transmits through the front mirror. This transmitted fraction then bounces back-and-forth

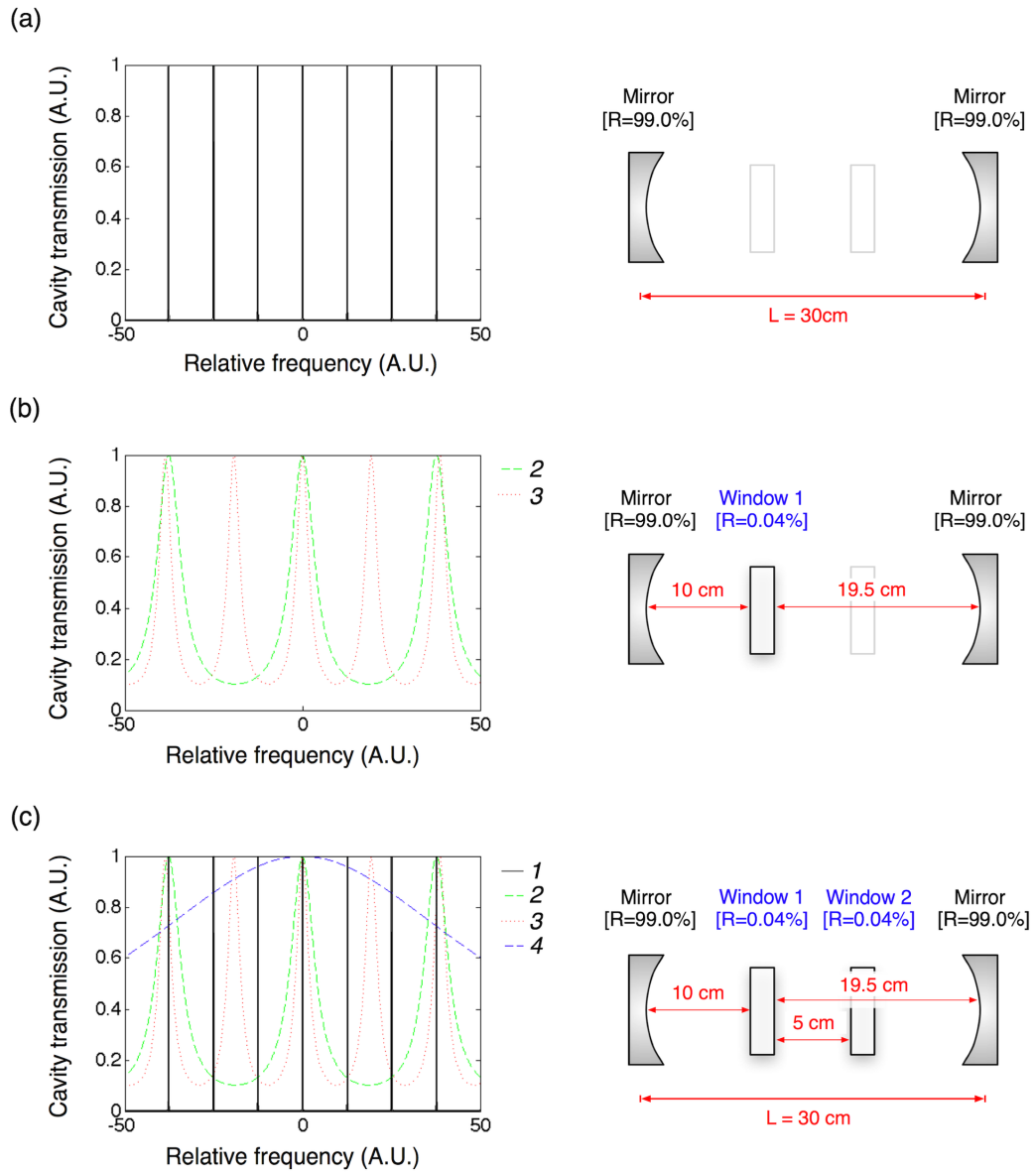

Figure 3.9: *Modelled spectra studying the effects of "cavities within a cavity" on transmission for cavity mode TEM_{00}. Legend: '1' shows $R = 99.0\%$, $L = 30.0\,\mathrm{cm}$; '2' shows $R = 51.5\%$, $L = 10.0\,\mathrm{cm}$; '3' shows $R = 51.5\%$, $L = 19.5\,\mathrm{cm}$; and '4' shows $R = 0.04\%$, $L = 5.0\,\mathrm{cm}$. (a) Transmission profile for the original two-mirror optical cavity. (b) Cuvette window acting as a low-reflectance mirror and bisecting the original cavity to create two additional cavities of mean reflectance $R = 51.5\%$, as plotted. (c) Transmission profiles for the original cavity plotted with three intra-cavity etalon profiles.*

between the two highly reflective dielectric mirrors. The intensity of the pulse drops with each pass, dependent on the reflectivity of the mirrors. It is possible to record this rate of decay, the so-called ring-down time, using a detector placed behind the rear mirror. The ring-down time is defined as the average time taken for the intensity of a light pulse leaving the cavity to decrease to $1/e$ of its initial value. The value of τ is then obtained by fitting a ring-down trace with an exponential decay, as shown in Figure 3.10. Continuous-wave (CW) sources can also be utilised for CRDS measurements. In CW set-ups, the light beam is cut off in order to measure the cavity response, i.e. decay rate [He et al., 1998; Romanini et al., 1997; Schulz and Simpson, 1998].

In the absence of an absorber, the transmitted intensity measured after the first pass, I_0, is given by:

$$I_0 = (T_1 I_{\text{in}}) T_2, \tag{3.9}$$

where $T_m = 1 - R_m$ (where m=1 or 2 for the respective mirror), i.e. if scattering and diffraction losses are assumed to be negligible. If one assumes the mirror reflectivity is equal to the geometric mean of both mirrors (where $R = \sqrt{R_1 R_2}$) and takes into account absorption according to Beer-Lambert (see Equation 3.1), then Equation 3.9 simplifies to:

$$I_0(\lambda) = I_{in}(\lambda) T^2 e^{-\alpha(\lambda)d}, \tag{3.10}$$

where d is the single-pass pathlength of the absorbing sample.

A round-trip consists of two passes; therefore, attenuation of stored intensity within the cavity follows the geometric progression of $(e^{-\alpha(\lambda)d}R)^{2n}$ for n roundtrips. The equation for total transmitted intensity can then be re-expressed in Equation 3.11.

$$\begin{aligned} I_n &= I_0 (e^{-\alpha d} R)^{2n} \\ &= I_0 \exp(-2n(\alpha d - |\ln R|)). \end{aligned} \tag{3.11}$$

Equation 3.11 can also be rewritten in terms of temporal dependence:

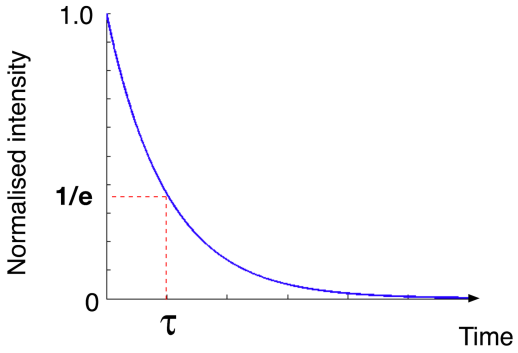

Figure 3.10: *Definition of ring-down time, τ, as shown on a monoexponential cavity ring-down decay. It is the time taken for the intensity to reach $1/e$ of its initial value.*

$$I_n(t) = I_0 \exp\left(\frac{ct}{L}(\ln R - \alpha d)\right), \tag{3.12}$$

where L is the cavity length and $t = 2Ln/c$. In the limit of high reflectivity (i.e. $R \to 1$), $\ln R \approx 1 - R$ and thus:

$$I_n(\lambda, t) = I_0(\lambda) \exp\left(-\frac{t}{\tau(\lambda)}\right), \tag{3.13}$$

where the decay constant, τ, is given by:

$$\tau(\lambda) = \frac{L}{c(1 - R(\lambda) + \alpha d)}. \tag{3.14}$$

In the absence of an absorber, the decay constant for the background, or empty resonator, is given by:

$$\tau_0(\lambda) = \frac{L}{c(1 - R(\lambda))}. \tag{3.15}$$

The absorption coefficient can then be obtained from CRDS measurements of τ and τ_0 using Equation 3.16:

$$\alpha(\lambda) = \frac{L}{cd}\left(\frac{1}{\tau(\lambda)} - \frac{1}{\tau_0(\lambda)}\right). \tag{3.16}$$

Figure 3.11 shows numerically simulated results using Equation 3.12 for a

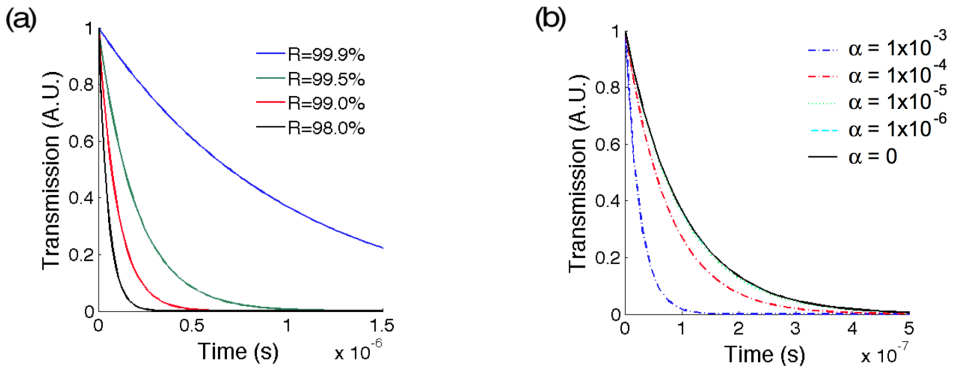

Figure 3.11: *Modelled CRDS decays for mirrors of different reflectivity and increasing levels of intra-cavity absorption for a cavity length* L =30 cm. *(a) Ring-down decay curves for mirrors of reflectivity* R =98.0 %, 99.0 %, 99.5 % *and* 99.9 %. *(b) Modelled changes in decay time for a cavity of R=99.0% mirrors and increasing trace levels of intra-cavity absorption,* α.

cavity of length 30 cm. The relatively low reflectivity mirrors, in comparison to those employed in the gas phase, lead to correspondingly short ring-down times, as shown in Figure 3.11(a) for an empty cavity with no absorption. The second challenge for liquid-phase CRDS is having to detect small absorbances, as reflected by fractional changes in ring-down times (see Equation 3.16). The scale of such changes is indicated in Figure 3.11(b) to provide an indication of the temporal resolution required for such measurements.

3.4.2 Cavity enhanced absorption spectroscopy

The first cavity-enhanced technique (CRDS) requires the time-resolved measurement events occurring on a very short time-scale. Cavity ring-down events in liquids are much shorter than those in the gas phase and typically of the order of 1 ns to 100 ns. This requires pulsed lasers (with pulse picking necessary for lasers of high repetition rates) or accurate "optical chopping" of continuous-wave (CW) sources in order to produce a pulsed output. Further to this, detectors must have a fast enough time response in order to detect and process the signal. These constraints have been met for single-channel liquid-phase techniques using point detectors [Alexander, 2006; Hallock et al., 2003; Xu et al., 2002]. The challenge

increases if broad bandwidth measurements spanning the entire visible spectrum are to be made simultaneously, i.e. without having to tune the light source or sequentially shift the detector.

A variant of CRDS called cavity enhanced absorption spectroscopy (CEAS) was introduced to simplify experimental requirements, whilst still offering the absorption enhancements conferred by cavity-enhanced techniques. CEAS involves the detection of changes in steady state intensity due to sample absorption rather than changes in ring-down time. As a result, individual light pulses do not need to be resolved. This significantly reduces the time resolution requirements of detectors and also means that a range of incoherent and coherent light sources can be used [Berden and Engeln, 2009]. The CEAS approach involves the excitation of many higher order modes across a broad spectral range in order to produce a dense mode structure, rather than the defined comb structure required for CRDS [Lehmann and Romanini, 1996] and more experimentally demanding techniques such as optical frequency comb spectroscopy [Thorpe et al., 2006]. In CEAS, the detected intensity is the superposition of all the intensities after an odd number of passes, as shown in Figure 3.12. This superposition is described below, starting with Equation 3.17 for the intensity of light transmitted out of the cavity after the first pass:

$$I = I_{\text{in}}(1 - R_1)(1 - A)(1 - R_2). \tag{3.17}$$

The intensity of subsequent passes is up to n passes:

$$\begin{aligned} I &= I_{\text{in}}(1 - R_1)(1 - A)(1 - R_2) \\ &\quad + I_{\text{in}}(1 - R_1)(1 - A)R_2(1 - A)R_1(1 - A)(1 - R_2) \\ &\quad + \dots \\ &\quad + I_{\text{in}}(1 - R_1)(1 - A)R_2^n R_1^n (1 - A)^{2n+1} \\ &= I_{\text{in}}(1 - R_1)(1 - R_2)(1 - A) \sum R_1^n R_2^n (1 - A)^{2n}. \end{aligned} \tag{3.18}$$

In the case where $R_1 = R_2 = R$, Equation 3.18 simplifies to:

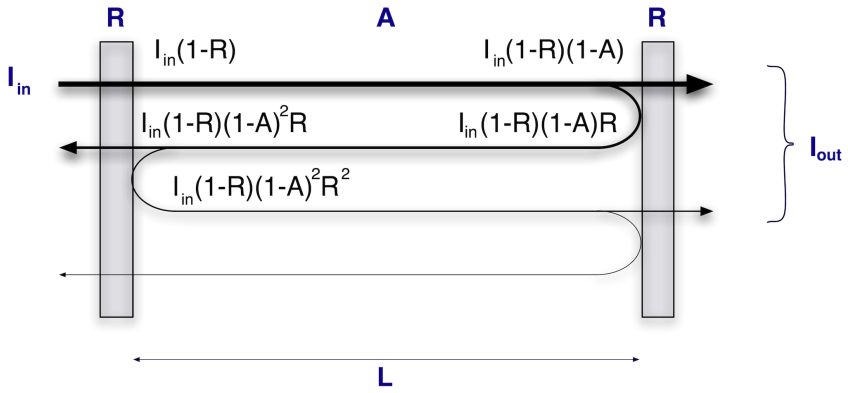

Figure 3.12: *Schematic diagram of variations in intensity of a beam propagating within a cavity of length L during CEAS measurements. I_{in} is the incident input intensity from the laser, and I_{out} is the time-integrated output intensity after the cavity. The labels denote reflection at the mirror surfaces (of reflectivity, R) and intra-cavity absorption (A) only. It is assumed here that the intensity of light will leak out equally from the front and back mirror.*

$$I_{\text{out}} = I_{\text{in}}(1-R)^2(1-A)\sum_{n=0}^{\infty} R^{2n}(1-A)^{2n}. \tag{3.19}$$

When $R < 1$ and $A < 1$ then the above Equation 3.19 can be simplified using a geometric progression to:

$$I_{\text{out}} = I_{\text{in}}\frac{(1-R)^2(1-A)}{1-R^2(1-A)^2}. \tag{3.20}$$

It is now possible to relate measurements made in the presence (I_{out}) and absence ($I_{out,0}$) of an absorbing sample to the absorption coefficient, α, approximated by Beer-Lambert to be $(1-A) = e^{-\alpha d}$ in the limit of low absorption ($\alpha \to 0$):

$$\frac{I_{\text{out},0}}{I_{\text{out}}} = \frac{1-(e^{-\alpha d}R)^2}{(1-R^2)e^{-\alpha d}}, \tag{3.21}$$

where d is sample pathlength. Equation 3.21 can be re-arranged to:

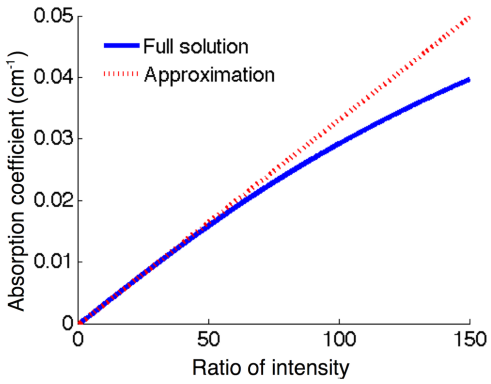

Figure 3.13: *Comparison of the full solution (Equation 3.22) and the approximated form (Equation 3.23) of the equation for calculating the CEAS absorption coefficient. Absorption coefficient, α, is plotted against ratio of intensity, I_0/I, at a fixed wavelength. The cavity parameters are set as $R = 0.99$ and L =30 cm.*

$$\alpha = -\frac{1}{d}\ln\left[\frac{1}{2R^2}\left(\sqrt{4R^2 + \left(\frac{I_{\text{out},0}}{I_{\text{out}}}(R^2-1)\right)^2} + \frac{I_{\text{out},0}}{I_{\text{out}}}(R^2-1)\right)\right]. \tag{3.22}$$

In the case of high reflectivity mirrors and at low loss (as $R \to 1$ and $\alpha \to 0$), Equation 3.22 becomes:

$$\alpha = \left(\frac{I_{\text{out},0}}{I_{\text{out}}} - 1\right)\left(\frac{1-R}{d}\right). \tag{3.23}$$

The approximate form (see Equation 3.23) has been compared with the full solution (see Equation 3.22) for a cavity of length 30 cm and a mirror reflectivity of 99.0%, cavity parameters used for liquid-phase CEAS measurements in this work (see Chapter 4). The results are shown in Figure 3.13. Equation 3.23 holds true for absorption values $\alpha \leq 0.01$ with a discrepancy of <1%, rising to a discrepancy of 5% for $\alpha = 0.02$. The typical range of CEAS measurements in this work is from $10^{-3}\,\text{cm}^{-1}$ to $10^{-6}\,\text{cm}^{-1}$. For a common dye such as rhodamine 6G ($\epsilon = 116\,000\,\text{M}^{-1}\,\text{cm}^{-1}$) this equates to concentrations in the nanomolar and high picomolar range.

Sensitivity Enhancement of Optical Cavities

Optical cavities increase the number of passes through a sample, but also reduce the amount of light reaching the detector after the cavity. Given this, it is necessary to determine whether there is an overall increase in sensitivity when using optical cavities, as modelled for a range of mirror reflectivity values. This can be done by comparing signal-to-noise ratios (SNR) of CEAS and single-pass measurements. Photon behaviour can be approximated using Poisson statistics and thus, if the mean signal intensity is N photons per second, the root mean square variation is given as $\pm\sqrt{N}$ photons per second. This is shown in Equation 3.24:

$$\mathrm{SNR} = \sqrt{N}. \tag{3.24}$$

The mirrors used for optical cavities significantly reduce the amount of transmitted light and as a result, the SNR will be reduced. This reduction in SNR based on intensity can be related to the light transmitted through the optical cavity using Equation 3.20 [Fiedler, 2005]:

$$\begin{aligned}
\mathrm{SNR}_{\mathrm{CEAS}}(I) &= \sqrt{I_{\mathrm{out,CEAS}}} \\
&= \sqrt{I_{\mathrm{in}} \frac{(1-R)^2(1-A)}{1-R^2(1-A)^2}} \\
&= \sqrt{\frac{(1-R)^2(1-A)}{1-R^2(1-A)^2}} \sqrt{I_{\mathrm{in}}}.
\end{aligned} \tag{3.25}$$

Equation 3.25 can be simplified in the high reflectivity ($R \to 1$, thus $1 + R \approx 2$), low absorption ($A \to 0$, thus $1 - A \approx 1$) limit. Making the substitution for the single-pass intensity, $\mathrm{SNR}_{\mathrm{SP}} = \sqrt{I_{\mathrm{in}}}$, gives:

$$\mathrm{SNR}_{\mathrm{CEAS}}(I) \approx \sqrt{\frac{1-R}{2}} \mathrm{SNR}_{\mathrm{SP}}(I). \tag{3.26}$$

The above relation needs to be related to absorption. Comparisons of the equations for single-pass (Equation 3.2) and CEAS (Equation 3.23) absorption coefficients show that use of an optical cavity increases pathlength by a factor $\frac{1}{1-R}$.

As a result, the SNR for a given absorption coefficient will be greater than for a single-pass measurement.

$$\begin{aligned} \mathrm{SNR}_{\mathrm{CEAS}}(\alpha) &= \frac{1}{1-R}\sqrt{\frac{1-R}{2}}\mathrm{SNR}_{\mathrm{SP}}(\alpha) \\ &\approx \sqrt{\frac{1}{2(1-R)}}\mathrm{SNR}_{\mathrm{SP}}(\alpha). \end{aligned} \tag{3.27}$$

The maximum enhancement factor, Q, of CEAS over single-pass measurements, in the absence of losses, can be written as $Q = \sqrt{(2(1-R))^{-1}}$.

In reality, background losses originating from either the measurement (e.g. detector noise) or from the sample (i.e. solvent absorption, scattering) will occur. The losses counteract the increase in cavity enhancement brought about by the use of high reflectivity mirrors. This is simulated in Figure 3.14 using Equation 3.25 where the substitution $A = \mathfrak{L}$ is made (where $\mathfrak{L}$ represents intra-cavity loss). Results in Figure 3.14(a) show that, in the absence of intra-cavity losses, the SNR can be increased by using mirrors of higher reflectivity. Figure 3.14(b) now takes into account the effects of intra-cavity absorption for simulated losses of $\mathfrak{L}$ =0 %, 0.1 %, 1.0 % and 4.0 %, for a fixed laser input intensity (I_{in}). The plot shows that at a certain value of $\mathfrak{L}$, intra-cavity losses will dominate and thus increasing mirror reflectivity would not yield SNR improvements. Preliminary measurements can be made to determine losses in a system and thus choose appropriate mirrors. The values chosen here (see Figure 3.14) are representative of those expected for the liquid-phase CEAS being carried out in this work.

Cavity Mirror Transmission

CEAS calculations are based on the fact that light is collected from only one mirror and, furthermore, the same amount of light (i.e. half) exits each mirror for the case of $R_1 = R_2$. This is denoted by the scaling factor of $\frac{1}{2}$ in Equation 3.27. Ouyang and Jones [2012] described cases where use of this constant scaling factor does not hold true. They referred to such cases as "unsymmetrical" transmission of light through the cavity; for instance if the mirror reflectivity were

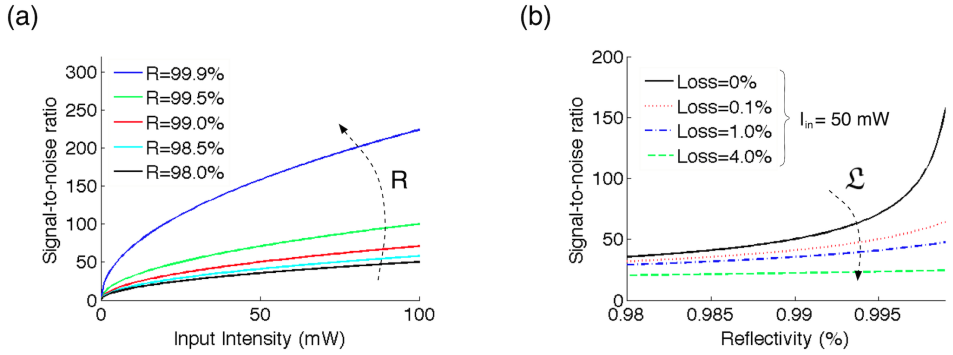

Figure 3.14: *Modelled signal-to-noise (SNR) ratio enhancement based on mirror reflectivity and intra-cavity background losses. (a) SNR as a function of laser input intensity for mirror reflectivity R =98.0 %, 98.5 %, 99.0 %, 99.5 % and 99.9 %. (b) Effect of intra-cavity loss ($\mathfrak{L}$) on SNR enhancement at a fixed laser input intensity (I_{in}) as a function of cavity mirror reflectivity.*

close to zero, then the cavity transmission would be closer to that of a single-pass measurement. In this case there would be a disparity in the intensity of light calculated as exiting the cavity and the actual detected intensity, leading to incorrect data analysis. Their analysis is applied here, assuming non-negligible intra-cavity losses of $\alpha d = 10^{-5}$ and $T = 1 - R$. Figure 3.15 shows the change in intensity $\Delta I = I_{\text{in}} - I_{\text{out}}$ of cavity transmission, normalised against the single-pass case (i.e. $\alpha d I_{\text{in}}$) as a function of mirror reflectivity R for a range different intra-cavity losses. Ouyang and Jones [2012] studied this relationship at a lower limit ($\alpha d = 10^{-7}$ in Figure 5 of [Ouyang and Jones, 2012]) where the ratio ΔI tends to $\alpha d I_{\text{in}}/2$ for reflectivity values of $R > 0.5$. The study in Figure 3.15 of higher intra-cavity losses, which are a feature of liquid absorption spectroscopy, shows that unsymmetrical transmission becomes significant at very high reflectivity too; therefore, care in analysis should be taken. Mirrors of reflectivity R =99.0 % still have symmetric transmission for losses up to $\alpha d = 10^{-3}$, so the simplification made in Equation 3.27 remains valid for most liquid implementations using such mirrors.

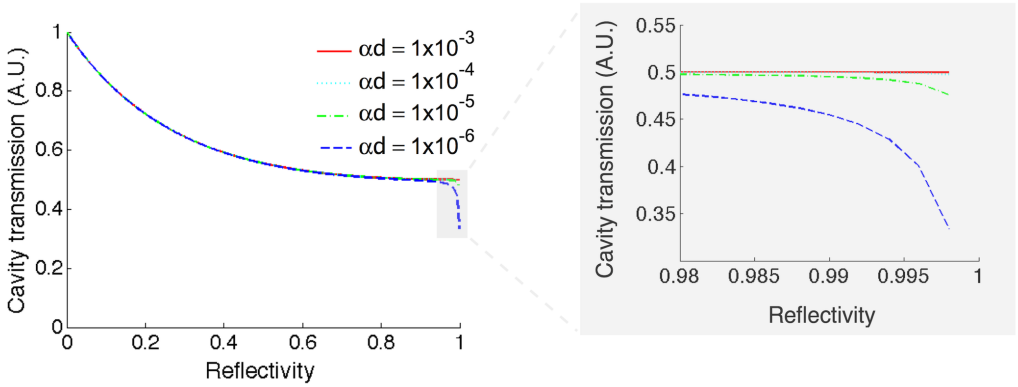

Figure 3.15: *Change in transmitted cavity signal* $(I_0 - I)$*, normalised by the single pass transmission* $(\alpha d I_{in})$*, for different intra-cavity losses as a function of cavity mirror reflectivity. Intra-cavity losses ranging from* $\alpha d = 10^{-6}$ *to* 10^{-3} *are shown on the plot.*

3.5 Summary

Optical cavities have been introduced in the context of liquid spectroscopy. Time-resolved CRDS and its variant CEAS have been introduced and shown to offer theoretical increases in sensitivity of the order of a few magnitudes over single-pass measurements. CRDS has the advantage of not requiring calibration, whereas CEAS does not require complicated electronics or fast detectors. Modelling has shown that both techniques are suitable for liquid-phase studies. SC radiation introduced in Chapter 2 can be coupled with CEAS to obtain significant gains in sensitivity, speed and bandwidth. The following chapters will further discuss design and implementation of this new technique. One final advantage over other light sources is that its inherently pulsed nature also allows for CRDS measurements to be carried out for system calibration.

Chapter 4

Supercontinuum Cavity Enhanced Absorption Spectroscopy

4.1 Introduction

This chapter describes the development of cavity enhanced absorption spectroscopy (CEAS) using a supercontinuum (SC) light source for the detection of liquid analytes at trace concentrations. The properties of SC radiation are discussed in Chapter 2 and optical cavities, which form the basis of CEAS, are introduced in Chapter 3. Applications that motivate the development of such a technique can be found in Chapter 6 of this thesis. These include the monitoring of an oscillating reaction, investigation of the photophysics of trace metal complexes used in high-tech consumer products, study of early-stage protein aggregation and also analysis of blood oxygenation. Application and development of CEAS have been made possible by the increased sensitivity, broad spectral bandwidth and high speed of the technique developed here.

Chapter Summary

This chapter highlights practical design considerations and relates them to the properties of liquids. The experimental design of the optical cavity and liquid

handling components is presented and described along with the overall SC-CEAS set-up. The chapter concludes with the characterisation of performance and proof of principle measurements, which also includes the method of calibration.

4.2 Experimental considerations

There are a number of challenges in first generating broad bandwidth laser-like light and then coupling into the cavity. An additional issue is the introduction of liquid-handling components into the optical path within the cavity which could dramatically reduce potential gains in optical pathlength. Furthermore, the increased density, scattering and absorption losses of the solvent must be overcome. The sample-holding element, or cuvette, must be suitably adjustable in order to optimise the optical alignment and also mechanically stable enough to maintain the alignment over long periods of time. There have been relatively few publications of liquid-phase CEAS or CRDS studies in the literature. Of these, a number of different approaches have been taken with regards to liquid sample handling. The key differences in approach are reviewed below.

Challenge of Liquid Handling and Cavity Design

One of the earliest liquid-phase cavity-enhanced studies used an intra-cavity cuvette placed at the Brewster angle. This was done in order to eliminate reflection losses at the windows of the sample cell of the liquid analyte (see Figure 4.1(a)) [Xu et al., 2002]. CRDS measurements were carried out by Xu et al. using a tunable laser to scan over a relatively narrow bandwidth range of 590 nm to 620 nm. The Brewster angle was fixed to that of the solvent (calculated relative to the refractive index of light in air, $n_{\text{air}} = 1.00$). The Brewster angle, θ_{B}, is defined as $\theta_{\text{B}} = \arctan(n_2(\lambda)/n_1(\lambda))$, where n_1 is the refractive index of light in the first medium and n_2 the refraction of light of the medium about to be entered.

In their paper, Xu et al. [2002] recommended this geometry only for cases in which the refractive index of the solvent matched that of the cuvette/quartz cell. The refractive index of fused silica optical windows used for this work is 1.46 at 590 nm and 20 °C [Malitson, 1965] and 1.54 for the quartz used by Xu et al.. This

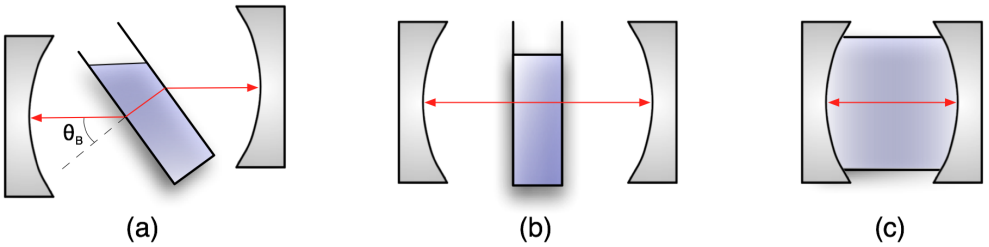

Figure 4.1: *Intra-cavity geometries for liquid-phase cavity-enhanced techniques. (a) Brewster-angle cell. (b) Zero-angle cell. (c) Liquid-filled cavity.*

makes water, which is the most commonly used solvent in this work, less than ideal for this method as it has a refractive index of 1.33 [Hale and Querry, 1973].

A further complication is that solvent index of refraction can change with wavelength [Hale and Querry, 1973]. This means that the corresponding Brewster angle does not remain constant, as can be seen in Figure 4.2 for a range of solvents. The refractive index of water does not change significantly, but for solvents such as ethylene glycol, the difference in refractive index at 400 nm compared to 632 nm [El-Kashef, 2000] results in a change in Brewster angle of more than 1°. In such cases, use of the Brewster angle approach would be problematic.

Fiedler et al. [2003] showed that a zero degree angle of incidence, i.e. normal to the cuvette window surface, (see "zero-angle" design in Figure 4.1(b)) produced relatively small optical losses as light reflected at the optical interfaces is maintained within the cavity. More recent studies simply placed the liquid sample in direct contact with the mirrors to avoid losses due to additional interfaces (see Figure 4.1(c)) [McGarvey et al., 2006; Seetohul et al., 2009].

According to the literature, the sensitivity achieved by Seetohul et al. [2009] is the lowest for liquid absorption spectroscopy at α_{min} =$2.8 \times 10^{-7}\,\text{cm}^{-1}$. The sample pathlength was 20 cm and light emitting diodes (LEDs) were used as the light source. The advantage of LEDs is that they are low in cost. The disadvantage for optical cavity techniques is that they are not easy to collimate and as such the beam size is much larger than a spatially coherent SC or laser beam. This explains why a large cross-sectional sample area, and thus volume (98 mL), was required in Seetohul et al. [2009]. This limits the overall applicability of such a measurement, as precious biological or chemical samples may be available only

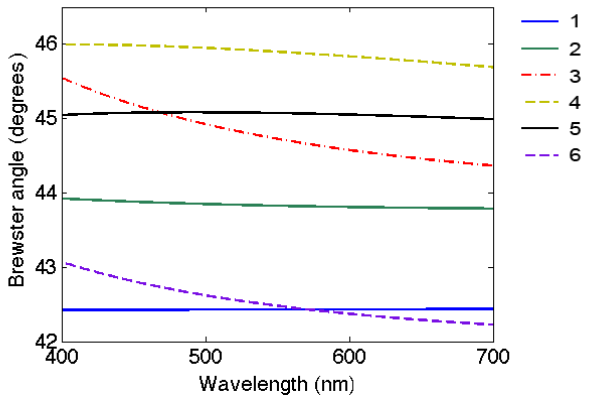

Figure 4.2: *Brewster angle for six aqueous solvents across the visible spectrum (where 1 = water; 2 = butanol; 3 = ethylene glycol; 4 = benzene; 5 = tetrachloromethane; and 6 = methanol). Solvent data at* 20 °C *are taken from El-Kashef [2000]; Moreels et al. [1984], with the Brewster angles for the solvent relative to the refractive index of fused silica [Malitson, 1965].*

in volumes two or more orders of magnitude smaller. Furthermore, the measurement time required with the LEDs was 2.5 s which may be too long for monitoring fast reactions. The use of the liquid-filled cavity configuration achieves very good sensitivity, but does bring up some practical issues. Seetohul et al. [2009] mention in their publication that alignment changes can be introduced when filling or emptying the cavity. Therefore, it would be of benefit to have a system in which sample exchange does not affect alignment and thus the enhancement in sample pathlength, such as in Figure 4.1(b).

Solvent Scattering Effects

Light scattering, spectral broadening and solvent shifts can all influence spectroscopic measurements of liquids. The elastic scattering of light depends on the particle size relative to the wavelength of incident light, λ, and falls into one of three categories, namely Mie, Tyndall or Rayleigh. Mie scattering occurs if the particle size is larger than $\lambda/10$ [Mie, 1908; Wiscombe, 1980]. Tyndall scattering is for particles (or colloids) of a size similar in order of magnitude as λ. It follows the same wavelength dependence as Rayleigh scattering, although Tyndall

scattering is much more intense, due to the larger particles and thus scattering cross-sections involved [Mer, 1948]. The third category of light scattering is Rayleigh scattering. This occurs in samples with particle sizes smaller than the wavelength of light [Rayleigh, 1900]. The extent of Rayleigh scattering, defined by a particle's scattering cross-section, is proportional to λ^{-4} [Cracknell and Hayes, 1991]. As a result, scattering will be stronger at shorter wavelengths in the blue than longer ones towards the red edge of the visible spectrum [Morel, 1974]. The liquid samples being measured with cavity-enhanced techniques are assumed to be homogenous and free of large particles. Ultrapure water ($18\,\mathrm{M\Omega\,cm^{-1}}$, Milli-Q, Millipore, USA) is used to reduce the risk of impurities making their way into samples. Further sample pre-treatment steps, such as filtration, could also be taken if required. For this reason, it is assumed that the effects of Mie and Tyndall scattering are negligible in this work.

Figure 4.3 models the scattering of haemoglobin (Hb) molecules in water at low concentration. In this analysis, the diameter of Hb is taken to be the particle size. The results have been plotted along with water absorption across the visible spectrum. Background absorption is a much bigger issue in the liquid phase than for gas measurements due to the increased optical density of liquid solvents [Pope and Fry, 1997]. Figure 4.3 shows that water (solvent) absorption dominates at longer wavelengths, with Rayleigh scattering only starting to have a significant contribution at around 480 nm and below. Different solvents will have different absorption profiles and also the Rayleigh scattering contribution will increase for larger molecules and higher sample concentrations. This is why light sources of higher spectral power are required to ensure enough light can be transmitted through samples onto the detector. This makes the use of high intensity broadband SC radiation well suited for the purpose (c.f. spectral intensity of different light sources in Figure 1.2).

Spectral Broadening and Shifts

Molecules and thus their chromophores are likely to have slightly different local environments in the condensed phase. This results in more diffuse spectra than say for the equivalent gas phase spectra. The term chromophore is used to de-

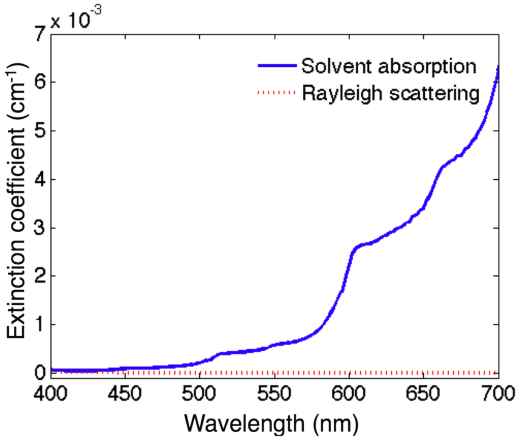

Figure 4.3: *Spectra of pure water optical absorption in the visible spectrum (*400 nm *to* 700 nm*) and modelled Rayleigh scattering of Hb molecules (*2.7×10^{-2} g/L *tetramer concentration) in water calculated over the same spectral region (dotted red line). Water data are from experimental measurements taken by Pope and Fry [1997] (solid blue line).*

scribe the part of a molecule (i.e. group of atoms) that gives rise to an electronic absorption corresponding to a spectral colour. An example of this is given later on in the thesis (see Section 6.2), where energy transitions in europium complexes cannot be resolved into their narrow bandwidth constituent peaks in the liquid phase. Qualitative definitions explaining spectral broadening in liquids, as described in a review by Myers [1998] , can be given. However, accurate quantitative models do not yet exist which is why discussion here is limited.

Spectral shifts are the result of solvent-solute interactions. $n \rightarrow \sigma^*$, $\pi \rightarrow \pi^*$ and $n \rightarrow \pi^*$ transitions in organic molecules can be spectroscopically studied by UV-visible absorption. Shifts to longer wavelengths, known as bathochromic or red shifts, are observed when polar solvents cause conjugation in unsaturated bonds. The π^* orbital is more susceptible to dipole-dipole interactions and the result is a lowering of this energy level [Matyushov and Newton, 2001]. This leads to a reduction in the energy gap between π and π^* orbitals and thus red shift, as shown in Figure 4.4.

Strong $\pi \rightarrow \pi^*$ transitions occur in the UV, whereas $n \rightarrow \pi^*$ transitions occur in the near-UV to visible spectrum. The n electrons are heavily influenced by

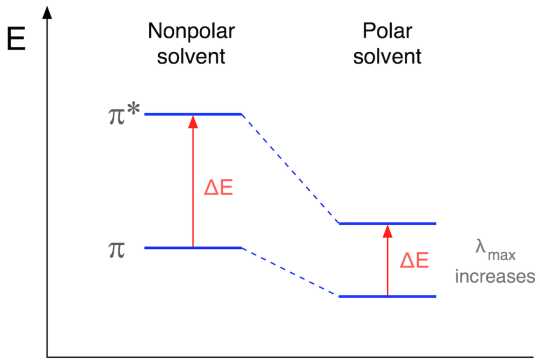

Figure 4.4: *Effects of conjugation in polar solvents. Use of a polar solvent (e.g. alcohol) as opposed to a nonpolar solvent (e.g. hexane) results in a reduction in the π and π^* energy difference and resultant increase in absorption wavelength - bathochromic or red shift.*

strong hydrogen bonding which acts to drastically reduce their energy level, thus increasing the energy gap between the n and π^* orbital. This results in a hypsochromic or blue shift. Hydrogen bonds are the strongest type of intermolecular force and, as a result, blue shifting will dominate over any bathochromic reduction in $n \rightarrow \pi^*$ in solvents capable of forming hydrogen bonds. Examples of suitable solvents include water, alcohols, amines and other molecules with O-H or N-H bonds. Blue shifts can be as much as 25 nm to 50 nm [Robinson et al., 2004]. Therefore, solvent selection is even more important if the spectral bandwidth of the technique is limited. This of course will be less of a problem for broadband techniques.

4.3 Experimental design and set-up

Experimental Set-up

The experimental set-up is shown in Figure 4.5. Output from a 1060 nm fibre laser (5 ps pulse width; FemtoPower 1060, Fianium, UK) operating at 1 MHz repetition rate was launched into a photonic crystal fibre (SC 5.0-1040 PCF, NKT Photonics, Denmark) to generate supercontinuum (SC) light with a spectral bandwidth ranging from around 480 nm to 1800 nm. The specification of the PCF is shown in Tables 4.1.

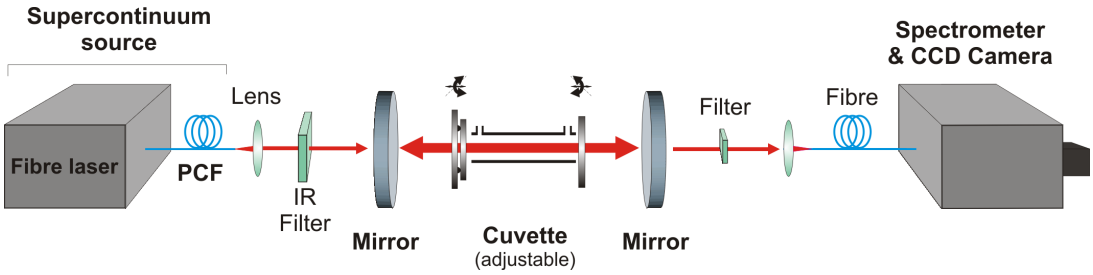

Figure 4.5: *Experimental SC-CEAS set-up for liquid-phase studies. A supercontinuum radiation source consisting of a fibre laser and photonic crystal fibre (PCF) is coupled into the optical cavity formed by a pair of plano-concave mirrors. The IR filter is placed in front of the laser output and any other interchangeable bandpass or short-pass filters are placed after the cavity. The liquid sample is contained in the intra-cavity cuvette. The spectrum of the transmitted light is detected by a grating spectrometer and CCD camera.*

Table 4.1: *Specifications for the photonic crystal fibre used for SC-CEAS.*

Photonic crystal fibre	Parameter value
Manufacturer model	SC-5.0-1040, NKT Photonics
Zero dispersion wavelength	1040 ± 10 nm
Core diameter	4.8 ± 0.2 µm
Cladding diameter	125 ±3 µm
NA @ 1060 nm	0.20 ± 0.05
Material	Pure silica

The IR portion of the SC output is cut out with a short-pass filter (730 IK 25, Comar Optics, UK), and the visible light is subsequently coupled into a 30 cm long linear optical cavity formed by a pair of plano-concave cavity mirrors (0.5 m radius of curvature, 99.0% nominal reflectivity from 400 to 680 nm; Layertec, Germany). The liquid sample is contained in a custom-designed cuvette. The spectrum of the light transmitted through the cavity was recorded using a grating spectrometer (Shamrock SR-303-i, Andor, UK; 50 lines/mm grating) equipped

with an air-cooled charge-coupled device (CCD) camera (iXon DV887ECS-BC, Andor, UK) capable of variable readout rates up to 10 MHz.

Cuvette Design

The cuvette design shown in Figure 4.6 allows independent alignment of each cell window. The intra-cavity cuvette is formed by a 50 mm long poly-methyl methacrylate (PMMA) or glass tube. The tube is placed between the cell windows (WG41050, Thorlabs, USA; $\lambda/10$ surface flatness, 20-10 scratch-dig, $\leq$5 arcsec parallelism) using rubber O-rings as seals. The first set of cuvette tubes had an internal diameter of 8 mm giving a total sample volume of 2.7 mL, including the spacer distance. The internal diameter of subsequent cuvettes was reduced to 5 mm bringing the sample volume down to 1.0 mL. The reduced volume cuvette tubes were used for applications where sample volumes are only available in small quantities (see Chapter 6), without a loss in sensitivity as the optical pathlength within the sample is the same for both tubes. The entire cuvette can be easily disassembled for complete cleaning of the windows and the cuvette tube without affecting the alignment of the cavity mirrors. The output of the SC source is from a single mode fibre and thus has very good beam quality. This means that the light beam can be tightly confined for coupling into the optical cavity [Watt et al., 2009]. The design enables the cuvette material, pathlength and/or total volume to be changed to suit different applications by simply replacing the low cost tube element.

4.4 Results and discussion

4.4.1 Figures of merit

Absorption spectra of Alexa Fluor 633 Hydrazide (AF633H, Invitrogen, USA), commonly employed in antibody labelling and cell tracing, dissolved in ultrapure (18 MΩ cm^{-1}) water are shown in Figure 4.7 at 15 nM and 30 nM concentrations. The plot also includes the water (solvent) baseline, which is well below the measured concentrations, giving an indication of sensitivity of these measurements. The total sample volume was 2.7 mL.

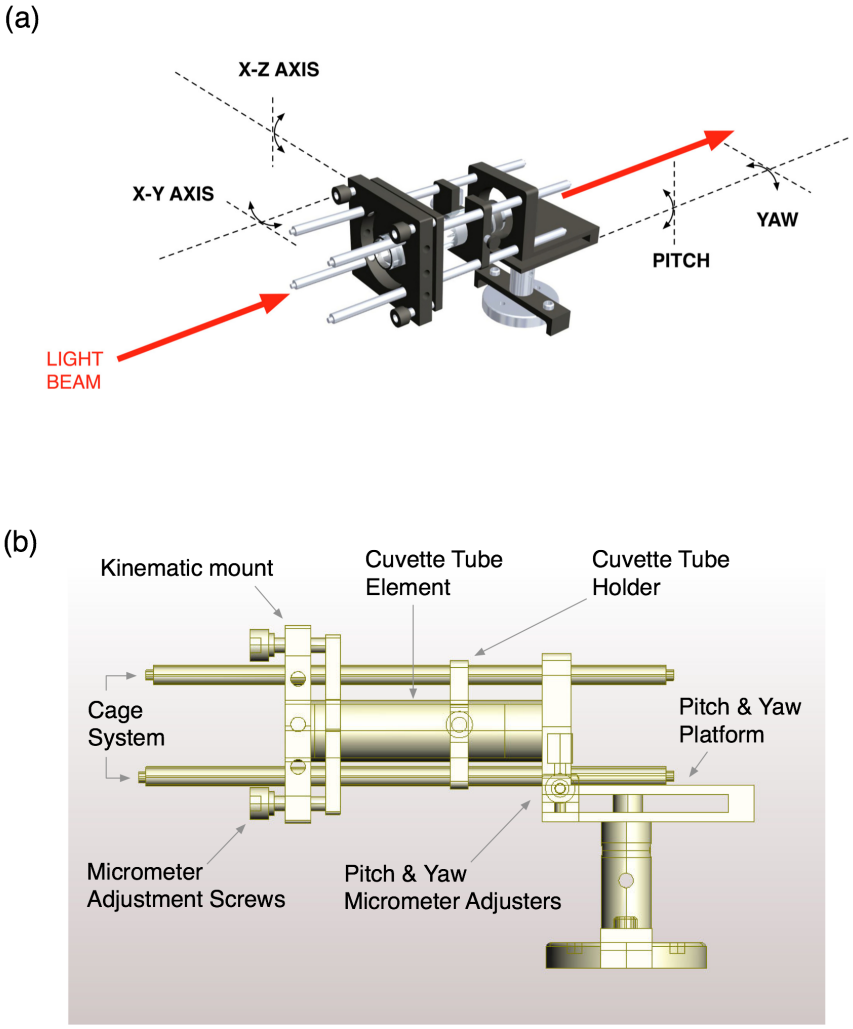

Figure 4.6: *Components and rotational axes of custom-designed cuvette. (a) Rotational axes of cuvette. The front window is placed in a kinematic mount and the back window mounted to a pitch and yaw platform. (b) Cross-sectional illustration of individual components of the cuvette. Cuvette window 1 is held in a kinematic mount (KC1, Thorlabs, USA) and cuvette window 2 is fixed to a pitch and yaw platform (ATP001, Thorlabs, USA). The total liquid sample pathlength is* 5.4 cm *(*5 cm *tube element and two* 0.2 cm *O-ring seals) and the sample volume is either* 2.7 mL *or* 1.0 mL *depending on the cuvette tube chosen.*

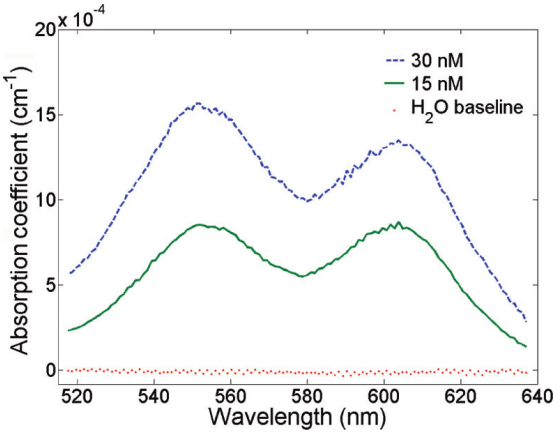

Figure 4.7: *Absorption spectra of Alexa Fluor 633 Hydrazide in* $18\,\mathrm{M\Omega\,cm^{-1}}$ *ultrapure water at* 15 nM *and* 30 nM *concentrations. The spectra were acquired using* 50 ms *single-shot exposure time. Averages of 20 single-shot spectra are shown here corresponding to a* 1 s *total acquisition time. The spectral resolution of the spectrometer was* 1.1 nm.

Quantitative results from SC-CEAS were obtained throughout the broadband detection of transmitted light in the absence, I_0, and presence, I, of the sample. It is from these two quantities that the absorption coefficient, α, was calculated, as derived in Section 3.4.2:

$$\alpha(\lambda) = \left(\frac{I_0(\lambda)}{I(\lambda)} - 1\right)\left(\frac{1 - R(\lambda)}{d}\right), \tag{4.1}$$

where d is the single-pass absorption length in the liquid sample (here $d = 5.4\,\mathrm{cm}$), I is the transmitted intensity in the presence of a sample (analyte and solvent), I_0 is the intensity in the absence of the sample (pure solvent), R is the effective mirror reflectivity and λ is wavelength.

Signal-to-noise ratio (SNR) is used to estimate the minimum detectable concentration from the standard deviation (σ) of the baseline noise of the measurement. This limit of detection (LOD) is defined as the limit at which the analyte can be detected. This is not to be confused with another metric known as the limit of quantification (LOQ). The LOQ is the limit at which the analyte concentration can be quantified to a reasonable degree of accuracy and is defined as LOQ$= 10\sigma$. Values for LOD are more commonly quoted and will thus be used

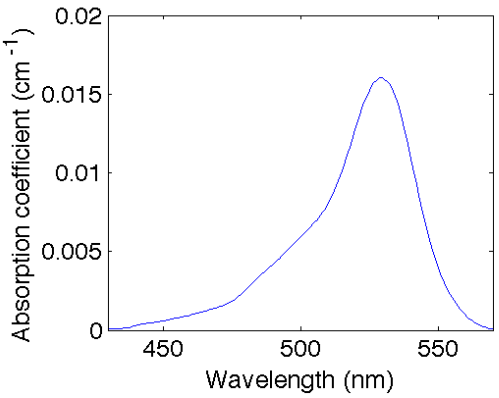

Figure 4.8: *Absorption spectrum of rhodamine 6G in* $18\,\mathrm{M\Omega\,cm^{-1}}$ *ultrapure water at* 246 nM *concentration with a* 5 ms *single-shot exposure time. A total of 200 individual spectra were averaged corresponding to a* 1 s *acquisition time. The spectral resolution is* 0.7 nm.

from hereon in this work.

Rhodamine 6G (Rh6G, Sigma Aldrich, USA) was used to further characterise the performance of the spectrometer, a spectrum of which at 246 nM concentration is shown in Figure 4.8. The sample volume was 2.7 mL. A 3σ minimum detectable absorption coefficient of $9.1 \times 10^{-6}\,\mathrm{cm^{-1}}$ at 550 nm for a total 10 ms signal integration time on the CCD camera (average of 2 single-shot spectra) was thus obtained. This value can be quoted in the normalised form of $9.1 \times 10^{-7}\,\mathrm{cm^{-1}\,Hz^{-1/2}}$ to facilitate easier comparison with other methods. The corresponding minimum detectable Rh6G concentration for this figure is thus calculated as 200 ± 70 pM. Errors can be estimated using the propagation of error method [Ku, 1966]. This method is mainly suitable for cases in which the error cannot be determined directly from experimental results. Here, the error is calculated from measured data and thus provides a more accurate estimate of the minimum detectable absorption coefficient of the system as it is actually configured for each measurement. The overall sensitivity demonstrated here is comparable with the best reported liquid-phase absorption results obtained but with the advantage of broad spectral coverage (see Table 4.2).

Table 4.2: *Comparison of liquid-phase absorption techniques using linear optical cavities.*[†]

Reference	Method	$R(\%)$	d_{abs} (cm)	λ (nm)	t_{meas} (s)	α_{min} (cm^{-1})	$\alpha_{\text{min},\Delta f}$ (cm^{-1} $\text{Hz}^{-1/2}$)
[Kiwanuka et al., 2010]	CEAS	99.0	5.4	400-700	0.01	9.1×10^{-6}	9.1×10^{-7}
[Alexander, 2006]	CRDS	99.98	0.0023	628		5.4×10^{-3}	
[Bahnev et al., 2005]	CRDS	99.98	0.2	532		1.6×10^{-4}	
[Fiedler, 2005]	CEAS	99.0	1	607	5	2×10^{-5}	4.5×10^{-5}
[Hallock et al., 2002]	CRDS	99.98	21	620-670		1×10^{-6}	
[Hallock et al., 2003]	CRDS	99.98	23	655		3.3×10^{-7}	
[McGarvey et al., 2006]	CEAS	99.998	0.175	783	7×10^{-6}	9.1×10^{-6}	2.2×10^{-7}
[Seetohul et al., 2009]	CEAS	99.9	20	630-670	2.5	2.8×10^{-7}	4.4×10^{-7}
[Xu et al., 2002]	CRDS	99.97	1	607		1×10^{-5}	

[†] The table shows the cavity-enhanced method used: reflectivity of cavity mirrors R, single-pass sample absorption length d_{abs}, measurement wavelength range λ, total measurement time t_{meas}, minimum detectable absorption coefficient α_{min}, and the minimum detectable absorption coefficient normalised by the measurement bandwidth $\alpha_{\text{min},\Delta f}$.

4.4.2 Calibration

The determination of the wavelength dependent absorption coefficient, α, requires the mirror reflectivity value, $R(\lambda)$, to be known at each spectral position (c.f Equation 4.1). As a result, CEAS measurements require prior calibration to determine $R(\lambda)$. Calibration can be done by measuring a broadband absorber of known concentration and spectrum. However, this is limited by the availability of suitable calibration species in the spectral regions of interest. Furthermore, mirror reflectivity cannot be determined at spectral positions where the sample absorbance is zero, i.e. in between absorption peaks. An alternative method is to directly measure the reflectivity at a single wavelength or in a narrow wavelength range, e.g. using cavity ring-down spectroscopy (CRDS), and then using published data on the spectral response of the mirrors and solvent to extend the calibration over the required wavelength range.

A broadband mirror reflectivity calibration using phase-shift cavity ring-down spectroscopy (PS-CRDS) has been developed for gas phase measurements [Laurila

et al., 2010]. In this CRDS variant, an acousto-optic tunable filter (AOTF) is used for light modulation and a lock-in amplifier for phase detection. The phase delay, ϕ, on periodically modulated light coupled into the optical cavity is measured sequentially across the mirror reflectivity range [Berden and Engeln, 2009; Lakowicz, 2006]. The sensitivity of this PS-CRDS is maximised when ϕ is $\pi/4$, given the equation $\tan\phi = -\tau\Omega$, where Ω is the angular modulation frequency [Engeln et al., 1996]. The corresponding angular frequency must be chosen to satisfy $\tau\Omega \approx 1$. Unfortunately, this poses practical constraints for the mirrors of relatively modest reflectivity used in the liquid phase (i.e. 99.0% reflectivity), as the nanosecond ring-down times would require correspondingly high light modulation frequencies in order to achieve good sensitivity. The fact that the majority of commercial lock-in amplifiers are limited to around 100 kHz currently precludes this particular calibration method.

Calibration Results

Standard cavity ring-down spectroscopy (CRDS) was performed in this work using spectrally filtered SC pulses [Watt et al., 2009]. In CRDS a pulse of light is coupled into the cavity and the decay rate or ring-down time, τ, is measured [Berden and Engeln, 2009]. The value of τ is obtained by fitting an exponential curve to the ring-down trace. At the limit of high reflectivity ($R \to 1$, thus $\ln R \approx (1 - R)$) the ring-down time is given by [Berden and Engeln, 2009]:

$$\tau = \frac{L}{c[(1 - R) + \alpha d]}, \tag{4.2}$$

where c is the speed of light, R is mirror reflectivity, α is the sample absorption coefficient, d is the single-pass sample length and L is the mirror separation or cavity length.

The mirror reflectivity values determined using CRDS were 98.8% (nominal 99.0%) and 99.9% (nominal 99.9%). The CRDS measurements were taken using the same in-house built SC source described in Section 4.3, but operating the pump laser source at 331 kHz repetition rate. The 99.0% and 99.9% mirrors used in this work operate in different spectral ranges and thus required different band-pass filters for the SC output beam: 500 ± 70 nm (500 IW 12, Comar Optics,

UK) for 99.0% mirrors and 633 ± 40 nm (633 IU 12, Comar Optics, UK) for 99.9% mirrors. Individual light pulses were then detected with a photomultiplier tube, with average decay curves of 500 laser pulses shown in Figure 4.9.

The single-pass losses associated with the cuvette windows β_{window} were calculated using Equation 4.2 in the absence of a liquid sample, using the substitution $\beta_{\text{window}} = \alpha d$. This was measured as $\beta_{\text{window}} = 0.5\%$. Interestingly, this value is much lower than the 4% reflectional losses R_{loss} in the case of a normal incident light beam on a window (of $n_2 = 1.46$), as described by Fresnel's law [Hecht, 2002]:

$$R_{\text{loss}} = \left(\frac{n_1 - n_2}{n_1 + n_2} \right)^2, \tag{4.3}$$

where $n_1 = 1.0003$ for air. This shows that the use of the custom-designed intra-cavity cuvette did not introduce significant losses for this set-up.

Enhancement Effect of the Optical Cavity

In an ideal case, one would increase the pathlength by increasing the reflectivity of the cavity mirrors used (cf. Equation 4.1). However, a point will be reached when the intra-cavity losses become the limiting factor, as previously discussed in Section 3.4.2. In the liquid phase, these intra-cavity losses are primarily due to the introduction of cuvette windows and also the solvent itself, through absorption. Fiedler [2005] derived a relationship for the enhancement factor of CEAS techniques over different background losses. They obtain an empirical relationship for the optimum mirror reflectivity, R_{opt}, for given single-pass intra-cavity losses (see Equation 6 in [Fiedler, 2005]) stating that there is no benefit in using mirrors of reflectivity $R > R_{\text{opt}}$ as no further pathlength enhancement will be gained. Solvent absorption losses have been shown by Cabrera et al. [2006] to be of significance. Results from CRDS were used to determine these losses and thus quantify the enhancement effect of the cavity.

Mirror calibration results show that there are 40 passes in total for the water-filled cavity using 99.0% reflectivity mirrors. This means that the effective sample pathlength of a 5.4 cm cuvette within the cavity is 2.1 m. This is a significant enhancement over the 1.0 cm single-pass pathlength used by spectrophotometers.

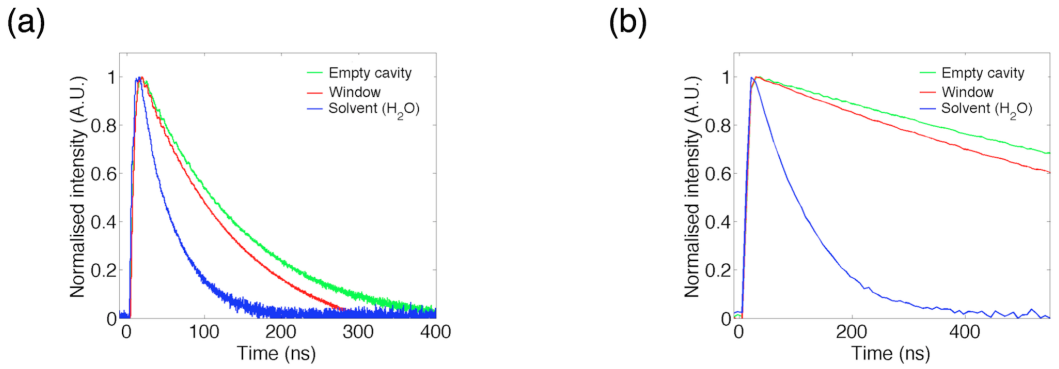

Figure 4.9: *Normalised ring-down profiles for calibration of cavity losses. Profiles are shown for an empty cavity, single window loss, and solvent loss (ultrapure* $18\,\mathrm{M\Omega\,cm^{-1}}$ *water). (a) Nominal 99.0% reflectivity mirror pair measured within the high reflectivity range* 465 nm *to* 535 nm*. (b) Nominal 99.9% reflectivity mirror pair measured within the high reflectivity range* 613 nm *to* 653 nm*.*

The empty 99.9% mirror cavity had a much longer lifetime ($\tau_{99.9\%} = 800\,\mathrm{ns}$ compared with $\tau_{99.0\%} = 90\,\mathrm{ns}$), implying a greater number of passes due to higher reflectivity, as expected. The addition of the liquid solvent drastically reduced the lifetime, as can been seen in Figure 4.9 (sharper gradient of exponential decay for H_2O losses). This limited the number of passes to 120 and an effective sample pathlength of 6.6 m. The results show a threefold increase in pathlength for the order of magnitude increase in reflectivity. Solvent losses dominate, as shown by the ring-down spectra in Figure 4.9. Losses of 2300 ppm for 99.0% mirrors and 7000 ppm with 99.9% mirrors (the latter measured at their longer operating wavelengths) were measured. This agrees with the findings of Pope and Fry [1997]. Absorption varied quite considerably from $5.0 \times 10^{-3}\,\mathrm{cm^{-1}}$ at 692.5 nm (equivalent to 27,000 ppm) down to a minimum of $4.0 \times 10^{-5}\,\mathrm{cm^{-1}}$ at 417.5 nm (216 ppm). Fiedler [2005] suggests that the optimum reflectivity (corresponding to the maximum loss of $5.0 \times 10^{-3}\,\mathrm{cm^{-1}}$) would be 99.0% which is in agreement with the above calibration measurements. The above results confirm that solvent absorption is the limiting factor, as it commonly is with other spectroscopic techniques in the condensed phase.

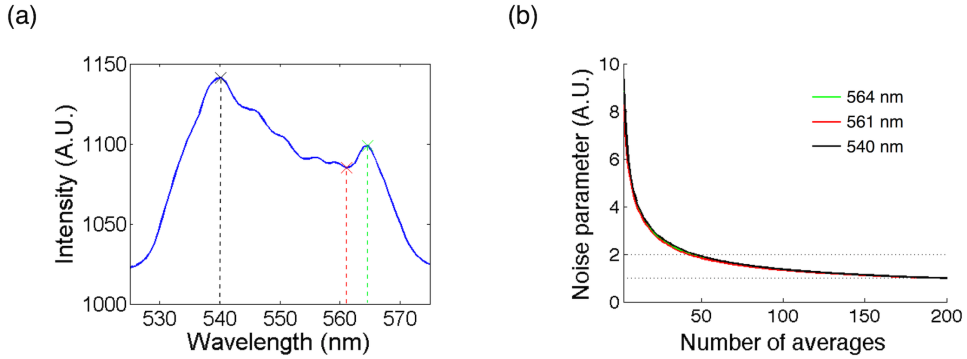

Figure 4.10: *The effect of signal averaging on SC-CEAS measurement noise reduction. (a) Intensity spectrum of light transmitted through an empty optical cavity (where* $L = 40\,\text{cm}$, $R = 99.0\,\%$*). The spectrum is an average of 200 single-shot spectra, taken with an exposure time of 5 ms. Three wavelengths are indicated on the spectrum:* 540 nm, 561 nm *and* 565 nm. *(b) Reduction in signal noise as the degree of spectral averaging is increased.*

Stability Analysis and Detector Averaging

Signal averaging is a well-known method to improve measurement sensitivity, as has been shown in previous studies [Hult et al., 2007; Werle et al., 1993]. However, some applications such as reaction monitoring, require fast acquisition times. Achieving good time resolution is in direct conflict with extensive signal averaging. Therefore, a balance must be struck based on the equipment to be used and system requirements. The required exposure time is dependent on the sensitivity of the CCD camera. Figure 4.10 shows the proportional error as a function of signal averages from which the amount of averaging typically required in this particular set-up can be seen.

Figure 4.10(a) shows a typical spectrum of light transmitted through the cavity and detected on the CCD camera. The set-up is as described in Section 4.3 and, in this case a narrow bandwidth filter (550 IU 12, Comar Optics, UK) is used to limit the spectral bandwidth of light passing through the cavity to 40 nm centred at 550 nm. The intensity spectrum shown is obtained from 200 camera frames with a single-shot exposure time of 5 ms. A comparison is shown for three different wavelengths to demonstrate the effects of signal averaging across

the spectrum. The noise parameter in Figure 4.10(b) is taken as the standard deviation of signals measured with n averages, where the integer n varies from 1 to 200, normalised by the mean error for 190 to 200 averages. The results show a significant reduction in error as a result of signal averaging with an order of magnitude improvement from 2 to 45 averages. There were no discernible differences at the different wavelengths selected in Figure 4.10, as signal intensity is sufficient across the wavelength range. It is worth noting that 100 averages dramatically reduce the noise, but require only a 0.5 s total acquisition time, given the single-frame exposure time of 5 ms.

4.5 Conclusions

A spectrometer for the rapid and sensitive detection of liquid-phase analytes at trace concentrations is presented. Broad spectral bandwidth supercontinuum radiation was coupled into a linear optical cavity incorporating an intra-cavity liquid-sample cuvette. CEAS spectra of trace species covering more than 300 nm were recorded. In this case, the bandwidth is limited only by the high reflectivity range of dielectric mirrors. Single-shot acquisition times of 10 ms to 50 ms are demonstrated here. The effective absorption path length exceeds 2 m in sample volumes measuring 1.0 mL. A key feature of the instrument is that it can be calibrated using cavity ring-down spectroscopy without the requirement of changing the optical alignment. The sensitivity of the instrument is exemplified by measurements of trace concentrations of dye molecules in water. A minimum detectable absorption coefficient of $9.1 \times 10^{-7}\,\mathrm{cm^{-1}\,Hz^{-1/2}}$ at 550 nm was obtained. The capability to capture broad bandwidth absorption spectra on short time scales opens up a number of potential applications, to be presented in forthcoming chapters.

Chapter 5

Broadband Cavity Ring-down Spectroscopy

5.1 Introduction

The previous chapter introduced cavity enhanced absorption spectroscopy (CEAS) for fast, spectrally broad measurements of liquids at low concentration. This chapter investigates the possibility of performing the variant cavity ring-down spectroscopy (CRDS) over a broad spectral bandwidth. Implementation of broadband CRDS (BB-CRDS) poses a number of design challenges which are discussed in the following section.

SC-CEAS demonstrated in Chapter 4 enabled highly sensitive measurements of liquid analytes to be undertaken. Typical acquisition times were of the order of milliseconds for spectra of 120 nm bandwidth. Despite such advantages, accurate broadband calibration of SC-CEAS remains an issue. The method presented in Chapter 4 uses a CRDS measurement taken over a narrow bandwidth spectral range to re-scale reflectivity values from the manufacturer-supplied data. A BB-CRDS technique that measures reflectivity values over all spectral positions simultaneously would provide a more accurate calibration system.

There are a number of challenges that have thus far hindered the development of BB-CRDS in the liquid phase. CRDS requires fast measurement of cavity ring-down events, as mentioned in the introduction to optical cavities (see

Chapter 3). The SC sources used in this work are pulsed, with variable repetition rates (∼0.5 MHz to 40 MHz). Consequently, the same sources used for SC-CEAS are suitable to be used for time-resolved BB-CRDS measurements. Narrowband CRDS measurements have already been demonstrated in Chapter 4 using a single-channel photomultiplier tube (PMT) and SC source. The advent of new detectors and latest developments in photon counting technologies could offer opportunities in further developing a broadband variant, as discussed later in this chapter.

Chapter Summary

BB-CRDS is presented as a calibration method for the SC-CEAS technique developed in the previous chapter. This chapter discusses the specific challenges associated with liquid CRDS in greater detail. Methods of simultaneously recording multiple time-resolved ring-down times at different spectral positions are analysed along with the current detectors being used. The chapter concludes with a discussion of the enabling technology and implementation of a novel single photon avalanche diode (SPAD) array. Preliminary data, system validation and proof of principal measurements conclude the chapter.

5.2 Background

Simultaneous CRDS measurements over wide spectral ranges have until recently been limited by two key technological factors. The first has been the unavailability of pulsed, broad spectral bandwidth sources and the second, a lack of suitable detectors. Sources that have routinely been used in optical cavity techniques, such as tunable lasers [Hult et al., 2005], filament lamps [Fiedler et al., 2003; Hamers et al., 2002], and light emitting diodes (LEDs) [Kebabian et al., 2005, 2007] suffer from low spectral power density and/or limited spectral bandwidths. The recent advent of high brightness laser frequency combs [Cundiff and Ye, 2003; Udem et al., 2002] and supercontinuum (SC) sources [Alfano, 2006], is leading to a paradigm shift in the field [Stelmaszczyk et al., 2009, 2011].

The ability to resolve multiple ring-down events in parallel and at high speed remains a major challenge. However, there are now opportunities to replace the

detectors that have traditionally been used for spectroscopy with novel arrays. These arrays need to have the time-resolved capabilities of single-channel detectors such as photodiodes or photomultiplier tubes (PMTs), but also the ability to collect and process such data simultaneously.

Theory of Cavity Ring-down Spectroscopy

The cavity ring-down time is defined as the average time taken for the intensity of a light pulse leaving the cavity to decrease to $1/e$ of its initial value, as derived in Section 3.4.1. The absorbance is calculated for ring-down times measured in the presence (τ) and absence (τ_0) of the absorbing sample, using [Lehmann et al., 2010]:

$$A(\lambda) = \frac{\alpha(\lambda)d}{2.303} = \frac{L}{2.303c}\left[\frac{1}{\tau(\lambda)} - \frac{1}{\tau_0(\lambda)}\right], \tag{5.1}$$

where c is the speed of light, L is the optical length of the cavity, α is the sample absorption coefficient, and d the single-pass optical length inside the liquid sample. Here, $L = L_{\text{air}}n_{\text{air}} + dn_{\text{liquid}}$, where L_{air} is the free-space intra-cavity length in air and n represents the related refractive indices. Equation 5.1 is valid for $\alpha \ll 1$. We use this equation to obtain calibration measurements and absorption spectra. As mentioned in the calibration section of the previous chapter (see Section 4.4.2), the value of τ is obtained by fitting the ring-down trace with an exponential decay.

Challenges for BB-CRDS in Liquids

Early implementers of CRDS took measures to ensure only single-exponential ring-down times were recorded [Newman et al., 1999; Romanini and Lehmann, 1993]. They achieved this by using probe lasers with a spectral bandwidths narrower than the linewidth of the absorbing sample. This eliminated potential errors due to the detection of "multi-exponentials" which it also precluded the use of broadband light sources. Multi-exponential decay occurs when significant differences in τ values (due to its wavelength dependence - c.f. Equation 5.1) result in decays which can no longer be described by a single-exponential [Hodges et al., 1996; Jongma et al., 1995; Zalicki and Zare, 1995]. The effect

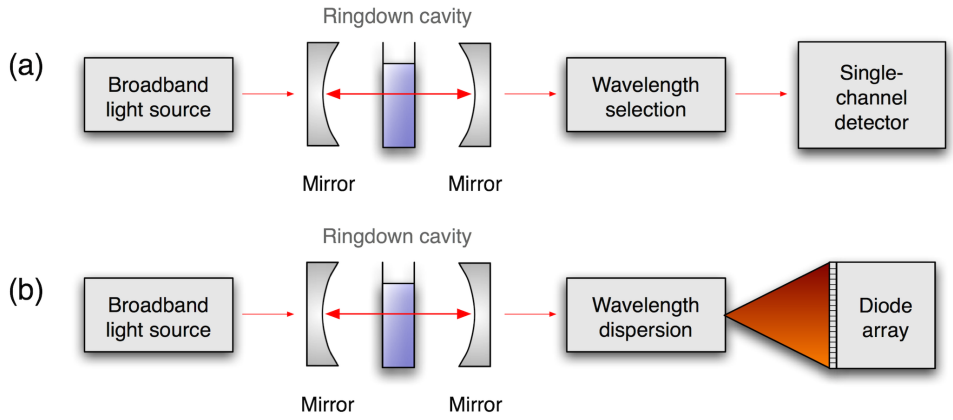

Figure 5.1: *Broadband cavity ring-down spectroscopy schemes using time-resolved detectors. (a) Wavelength selection method for a single-channel detector for point or sequential analysis. (b) Spectral dispersion onto an array for simultaneous wavelength- and time-resolved measurements.*

of this is an incorrect estimation of absorbance calculated using Equation 5.1. Reducing the number of different wavelengths incident on a single detector is one way of reducing the likelihood of multi-exponential decays. This does of course reduce the spectral bandwidth of the measurement, which may be undesirable. Sequentially scanning across different spectral positions is thus required to build up a broadband picture. An alternative is to use an array of detectors and then disperse light across the array, with each individual channel or pixel detecting only a narrow portion of the broadband light. Broadband measurements using the latter method can thus be carried out simultaneously, i.e. without scanning, as shown in Figure 5.1. Another possibility is a streak detection system, which is introduced and discussed in the following section of this chapter.

The most commonly used mirrors in the previous chapter had a nominal reflectivity of 99.0% for most wavelengths in the visible spectrum. A ring-down time of 90 ns was recorded for an empty cavity using a single-channel PMT over a spectrally filtered narrowband range (see Section 4.4.2). The introduction of the liquid sample reduces this. Differences in ring-down times of τ and τ_0 may be on the order of nanoseconds. Therefore, any proposed broadband scheme will need to achieve nanosecond resolution. Sensitivity also needs to be considered as

spectral dispersion or the use of narrowband filters reduces the spectral intensity in each detector channel. A broadband detector should also have a relatively uniform sensitivity and spectral response in each channel. Other challenges involve the speed of data transfer. Detector arrays record data from individual ring-down events across multiple channels. This greatly increases the computational processing demands. Finally, it is important to consider the required detector sensitivity.

5.3 Multi-channel cavity ring-down detection

Certain technologies have been used for simultaneous detection of ring-down times over multiple wavelengths in the gas phase. However, BB-CRDS has not previously been demonstrated for liquids. As mentioned in the previous chapter, the spectroscopic demands of measuring liquids differ from those imposed by gas phase measurements (c.f Section 4.2 with regards to solvent effects and broadening). Therefore, the two-dimensional (2D) detector technology used in the gas phase may not be suitable for liquid analysis. An overview of such technology is given below.

Current Detectors for 2D Measurements

Special detection schemes have been implemented in order simultaneously to record data in two dimensions (2D), i.e. wavelength- and time-resolved measurements. Three different commercially-available technologies that have been used for gas analysis are presented below.

Multi-anode photomultiplier tube array: Photomultiplier tubes (PMTs) are single-channel detectors that achieve high electron gain through a process called secondary-electron emission (see Figure 5.2). Unfortunately, they do not provide information on spectral distributions. For this reason, multi-anode PMTs were developed for measurements over broader spectral bandwidths [Pan and Chang, 2001]. Wavelength dispersion (as shown in Figure 5.1) can then be used to distribute the signal across the detector. Photoelectrons incident on the photocathode have their location recorded. Electron multiplication then occurs such that the

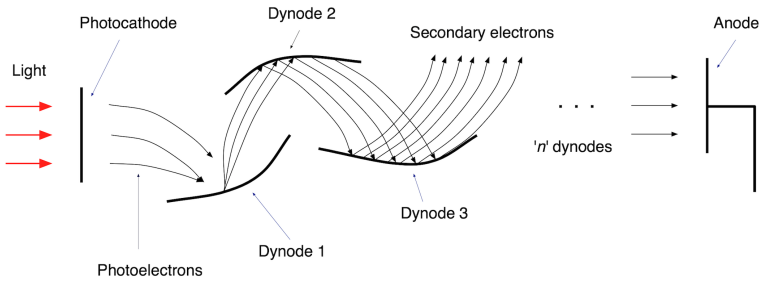

Figure 5.2: *Operation principal of a photomultiplier tube using secondary-electron emission electrons. Typical detectors achieve maximum electron number gains of* 10^6 *to* 10^8 *through the use of 9 to 12 dynode stages.*

readout from a specific pin at the base of the PMT housing can only correlate to one specific anode and corresponding to a specific location on the photocathode. As a result, spectrally-varying intensity data from a linear array of anodes can be recorded [Pan and Chang, 2006]. Linear multi-anode PMTs are of interest but at the time of writing these arrays are available only in 16-anode and 32-anode forms.

Clocked CCD: Charge-coupled devices (CCDs) are commonly used in spectroscopy for capturing intensity images for spectral imaging, where intensity distributions are spread across the wavelength range using dispersion optics, e.g. grating or monochromator. CCDs are available with single-photon detection capability over arrays featuring up to 512 and even 1024 pixels along a single axis. Such large pixel arrays have slow data transfer rates which can be limited to the order of 100 Hz. For this reason, Ball and Jones [2003] used a so-called "clocked" CCD (EEV 37-10) camera. This CCD has a small portion of its 512×1024 pixel arrangement exposed (10 rows) and the majority masked to protect it from incident light. The clocking mechanism of the pixel voltages shifts the charge on the exposed rows down on the masked area, as shown by Povey et al. [1998]. It is only these exposed rows that are actually photo-active, i.e. used for detection. Once detected, the signals are then periodically transferred to the masked "storage" section of the array. Ball and Jones [2003] used a clocking rate of 0.5 µs per row and thus had a time resolution of 5 µs for the 10 rows used. Ring-down times of between 1 µs to 4 µs were recorded for the measured sample of the gas sample

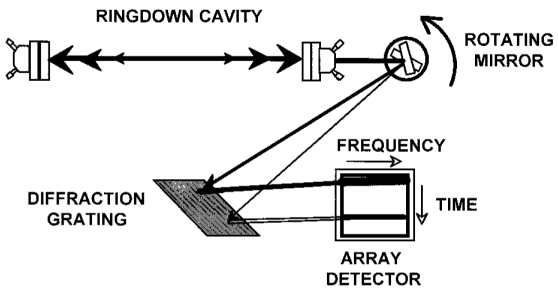

Figure 5.3: *Streak camera principal based on a high speed scanning mirror used to vertically disperse the monochromator/diffraction grating output. Figure taken from Scherer et al. [2001].*

(470 pptv NO_3). Repeated clocking then enabled a 2D time-wavelength picture to be obtained.

Streak camera detection system: Streak detection systems were designed to circumvent certain electronic constraints associated with detectors such as CCD cameras. Scherer et al. [2001] designed the system depicted in Figure 5.3 combining a scanning mirror with a CCD to obtain simultaneously two-dimensional information at high acquisition rates for gas phase frequency comb measurements. As with most spectroscopic methods, a monochromator is used to disperse spectral components along one axis, e.g. horizontally. A scanning mirror placed at the output plane of the monochromator deflects light onto different orthogonal rows of the CCD, in this case vertically. It is then possible to build up a spectrally dispersed, time-resolved image on the CCD by adjusting the oscillation frequency of the mirror. Thorpe et al. [2006] used a frequency of 355 Hz to collect ring-down times every 1.4 ms. The rate of mechanical mirror scanning then becomes a limiting factor in acquisition speed. A novel galvo-mirror scanning method has recently been demonstrated in a sensitive large image array CCD streak system. This approach has overcome traditional rotating mirror limitations and is capable of 2.4 MHz acquisition rates [Buckner and L'Esperance, 2013].

5.3.1 Design objectives for analysis of liquids

The design objectives for BB-CRDS are broadly similar to those outlined in the introduction to optical cavities (see Chapter 3). Although BB-CRDS and SC-CEAS (see Chapter 4) share some common features, e.g. cavity geometry, there are significant technical differences that need to be overcome in the development of a viable BB-CRDS system, e.g. detection system. The specific requirements are discussed below in more detail:

(i) *Time resolution*: CEAS is a continuous wave technique involving the measurement of integrated light intensity. CRDS, on the other hand, requires the use of pulsed light sources to measure time-resolved decays. As previously mentioned, ring-down times in the liquids are very short and thus any suitable technique must have a detector with nanosecond (10^{-9} s) resolution. As a broadband technique, this is the timing resolution required for each individual channel of a detector or array in BB-CRDS.

(ii) *Spectral bandwidth*: Solvent broadening in liquids results in spectra that are much broader than in gases, as previously discussed in Section 4.2. The two peaks of Alexa Fluor 633 Hydrazide (see Figure 4.7) for instance require a measurement bandwidth spanning 120 nm. Much greater spectral coverage would be required for mixtures of analytes that absorb at different wavelengths in the visible spectrum. The challenge for BB-CRDS is simultaneously to record time-resolved measurements over these multiple spectral positions. Some detectors may have fast time resolution, but lack the spectral channels to take real advantage of spectrally broad and pulsed SC sources. The mirrors used in this research have a high reflectivity bandwidth of ∼300 nm (99.0% mirrors, Layertec, Germany) and ∼100 nm (99.9% mirrors, Layertec, Germany) respectively. Therefore, a CRDS measurement bandwidth of 100 nm to 240 nm should be achievable.

(iii) *Spectral resolution*: The spectral resolution of the technique is constrained in practice by the spectral bandwidth divided by the number of available channels on the detector. Liquids generally have broad spectral bandwidths, although there are cases of molecules with more defined spectral features.

One such example is holmium chloride for which a resolution of ∼3 nm is required to resolve spectral detail. A 128-channel detector would be able to cover the entire visible spectrum at this resolution and a 64 channel detector could cover over 190 nm. As ever, there is a trade-off between spectral coverage and resolution and thus a suitable balance must be struck.

(iv) *Sensitivity*: The sensitivity of the detector is an important factor. Wavelength discrimination limits the amount of light per spectral channel on an array. Detectors need to be sensitive enough to detect light from a single pulse. Note that this is light that has passed through the optical cavity and is then dispersed onto different spectral channels for detection, i.e. of low intensity. As a result, it may be advantageous to use mirrors of lower reflectivity, i.e. 99.0% reflectivity rather than 99.9% reflectivity, to allow greater transmission of light onto the detector.

5.3.2 Single-photon avalanche diode array

The detectors introduced in Section 5.3 do not meet all of the design objectives set out in the previous sub-section. Although they meet the requirements of BB-CRDS in the gas phase, they are not suitable for use in this work. Current multi-anode PMTs do not have enough spectral channels and CCD cameras systems (both clocked and streak detection) nor do they meet the fast nanosecond acquisition rates required for liquid-phase analysis. A single-photon avalanche photodiode (SPAD) array on the other hand may provide an opportunity to overcome these current limitations.

Background to SPAD Array Development

The SPAD array used in this work was developed at the Fondazione Bruno Kessler, Trento, Italy, specifically for high-speed, time-gated fluorescence imaging [Esposito, 2012; Pancheri and Stoppa, 2009]. SPADs are capable of fast photon counting and time-resolved detection (sub-nanosecond). The sensors are capable of measuring fluorescence intensity in addition to lifetime across multiple spectral components. It is not commercially available yet but a prototype was

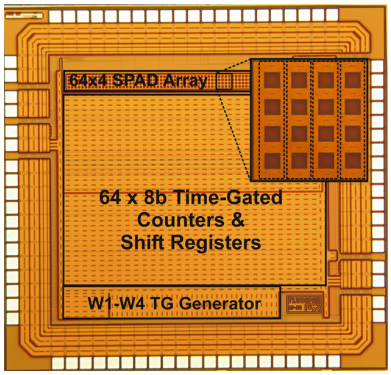

Figure 5.4: *Micrograph of the SPAD chip architecture used in the current work. The entire chip measures* 3.3 × 3.2 mm*, with the linear actively quenched array measuring* 1.6 mm × 100 µm*. Each of the 64 spectral elements can be time gated in rapid succession and consists of four light sensitive SPADs which are read out in parallel.*

made available for the present work, the architecture of which is shown in Figure 5.4. The SPAD array features 64 lifetime measurement channels, each of which has fast time resolution, high frame rates and low noise.

The aim in this chapter was to test this device's capabilities as a detector for BB-CRDS. SPADs are based on complementary metal-oxide semiconductor (CMOS) technology. CMOS technology has certain advantages and disadvantages, which are set out in an extensive review by Bigas et al. [2006]. The properties of a CMOS sensor are intrinsically linked to its architecture with individual circuits for each pixel enabling exceptionally fast readouts compared to CCDs, which scan individual pixels sequentially. Furthermore, CMOS on-chip processing enables operations such as time-gating, image processing, analogue-to-digital conversion to be executed rapidly. CCDs require additional external circuitry adding complexity and data throughput rates are much slower that for CMOS chips.

There are a few current disadvantages of CMOS technology compared to CCD technology which has been the dominant technology in the field. The increased circuitry for each pixel reduces the percentage of the light sensitive area and thus the so-called fill factor. This reduces sensitivity compared to CCDs which could have fill factors approaching 100%. CMOS sensors also have smaller dynamic ranges and are less sensitive to low-light levels. Recent advances have reduced

this gap in performance between CMOS and CCD sensors, with huge strides over the past few years driven by the miniaturisation of consumer electronic devices. Further advantages of CMOS sensors include lower power consumption, operational voltages and cost of manufacture. From a practical point of view, they have smaller pixels and can be readily integrated into different devices, as found in all new camera phones, camera-enabled tablet computers and compact lightweight digital single-lens reflex (dSLR) cameras entering the consumer market. In the past, SPAD arrays have been implemented or custom-built for particle experiments such as nuclear resonant scattering [Kishimoto, 2004] and X-ray detection [Hara et al., 1996; Nonaka et al., 1996; Shah et al., 2001]. The avalanche photodiode (APD) arrays used in these works are comprised of up to only 32 diodes with time responses in the range of $\sim$0.4 ns to 3 ns.

SPAD Array Operation

CMOS technology allows for complex operations and circuits to be integrated into the SPAD array to enable on-chip processing. All this functionality is maintained within the 3.3×3.2 mm chip, as can be seen on the micrograph in Figure 5.4. Each pixel of the SPAD array used here is made up of four SPADs. Having four SPADs per spectral element as opposed to one large SPAD reduces the dead time. Larger SPADs are prone to longer dead times due to the increased operational voltage required. This has the overall and undesirable effect of reducing count rate. More detailed technical information relating to the SPAD and initial development can be found in Pancheri and Stoppa [2009]. A brief overview is given in the text below.

SPADs are set to operate biased at a reverse voltage, V_A (at 'A' in Figure 5.5), above a particular threshold (breakdown voltage, V_B). At this voltage, the arrival of a single photon is enough to set off an avalanche (at 'B' in Figure 5.5), which is then detected [Cova et al., 1991; Dautet et al., 1993; Haitz, 1965]. The leading edge of the avalanche denotes the photon arrival time. The SPAD must then be reset or "quenched" before the arrival of the next photon. This is achieved by increasing the reverse voltage to a value above V_B and then restoring it to the original operating voltage V_A (from 'C' to 'A' in Figure 5.5). The speed of

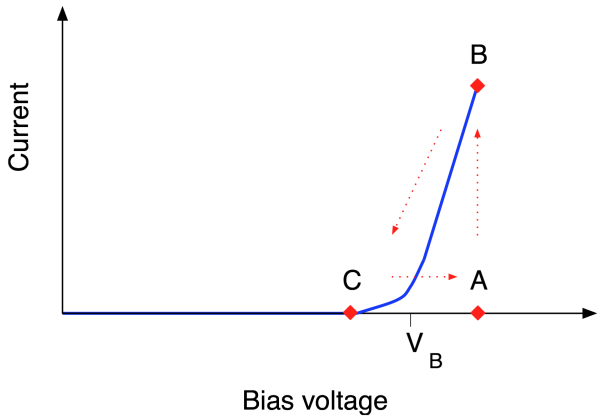

Figure 5.5: *Current-voltage characteristics of SPAD operating in Geiger mode, where V_B is the breakdown voltage. 'A' - SPAD is set to its operating voltage. 'B' - arrival of one photon is enough to trigger avalanche multiplication when in Geiger mode. 'C' - avalanche quenched by lowering the bias voltage below that of the breakdown voltage and avalanche multiplication stops. The SPAD is then reset by restoring the reverse voltage above V_B and back to point 'A' ready for the arrival of the next photon.*

the quenching process is important, especially if photons are arriving at a fast rate. A SPAD can quench itself passively, but this process is relatively slow. As a result, active quenching was introduced to apply a quenching pulse almost instantaneously instead of waiting for a passive voltage drop to occur [Cova et al., 1981].

Upon successful photon detection, data are stored by 8-bit time-gated counters and are then, after a specified signal accumulation time, transferred in parallel to shift registers for output (see Figure 5.6). Not only is this parallel transfer fast, but also it can occur without having to stop data acquisition. As a result, the only operational dead-time occurs during the resetting of counters which takes just a few nanoseconds.

The SPAD array receives external trigger signals from electronic pulse and waveform generators. This enables data accumulation time and initial time delay (with respect to the pump laser pulse), t_0, to be adjusted. Adjustment of t_0 permits different sections along the exponential ring-down decay to be sampled. There is an on-chip delay generator; however, an external generator, with a higher

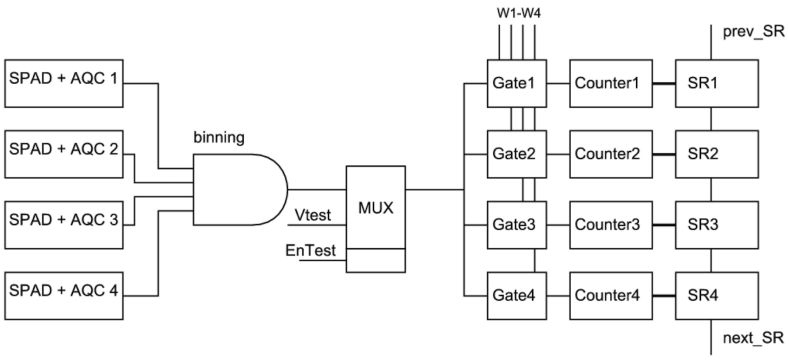

Figure 5.6: *Individual pixel circuitry for fast data capture, transfer and on-chip processing. Signals from the four SPADs are actively quenched and then binned. A multiplexer is included to enable external testing of the circuit and its response to test voltages V_{test}. The time-gates (Gate1 - Gate4) generate an output pulse when a signal is detected in the time windows (w_1 - w_4). Data accumulate on the counters and are transferred to shift registers in parallel. AQC=active quenching circuit, MUX=multiplier, SR=shift register. Figure reproduced courtesy of Pancheri and Stoppa [2009].*

resolution of delay control is used here with this prototype SPAD. The individual widths of the time gates w_1 to w_4 are adjustable from 0.7 ns to 10 ns (see Figure 5.7). Different combinations of gate widths can be set to ensure signals are recorded near the start of the decay rather than towards the end, where the signal intensity is much lower, thus improving the SNR.

5.4 Experimental design and set-up

Cavity Length and Sensitivity Limit of CRDS

The ability to distinguish and quantify small changes in ring-down time is what determines the sensitivity of CRDS. The minimum detectable absorption coefficient, α_{min}, as defined in Equation 5.1, can be re-written in the limit $\tau \to \tau_0$ as Equation 5.2 [Mazurenka et al., 2005].

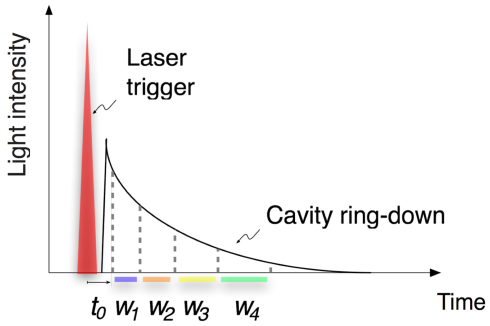

Figure 5.7: *SPAD time-gating principal for ring-down measurement. The ring-down time is determined from integrated signals during gates w_1 to w_4 for each of the 64 spectral channels. The time delay between the laser trigger and the opening of the first gate, t_0, can be adjusted in order to measure different sections along the decay.*

$$\begin{aligned}\alpha_{min}(\lambda) &= \frac{L}{cd}\left(\frac{\tau_0 - \tau}{\tau_0^2}\right) \\ &= \frac{1-R}{d}\left(\frac{\Delta\tau_{min}}{\tau_0}\right),\end{aligned} \tag{5.2}$$

given $\tau_0 = L/c(1-R)$. Equation 5.2 shows that the value of $\Delta\alpha_{min}$ can be reduced, thus increasing sensitivity, by increasing the mirror reflectivity or by increasing the sample path length. It is worth noting that the ultimate sensitivity depends on the ability of the detector to distinguish changes in ring-down time $\Delta\tau_{min}$. If τ_0 is small, then the absolute value of $\Delta\tau_{min}$ will also be small, perhaps even on the sub-nanosecond scale. The cavity ring-down time is directly related to the cavity length, L (c.f Equation 3.14 in Section 3.4.1). Measurements were performed to investigate this for a cavity formed of mirrors with nominal reflectivity 99.0% in the range 300 nm to 600 nm. The experimental set-up is shown with the PMT arm of the proposed test BB-CRDS set-up in Figure 5.8(a). Figure 5.8(b-c) shows the corresponding ring-down times for a range of cavity lengths measured with a PMT (R636-10, Hamamatsu, Japan) across a filtered narrow bandwidth range of 40 nm. As predicted, an increase in cavity length results in a linear increase in ring-down time. For short cavities this either increases the

demands on the detector in terms of timing resolution or decreases the ultimate sensitivity of the technique. It is worth noting that for a cuvette-based CRDS technique, an increase in cavity length does not mean a simultaneous increase in sample volume. This may be an added advantage.

According to Figure 5.8(c) the expected ring-down time for such a cavity (assuming a mirror reflectivity value of $R = 98.2\%$) would be $\sim$50 ns. The SPAD array, with a maximum time gate width of 40 ns, is capable of recording a significant portion of the ring-down decay for such a set-up. The mirrors used in this work have a radius of curvature of 0.5 m and so cavities of length $L \leq 1$ m would satisfy the cavity stability parameter (see Section 3.3). Figure 5.8(c) shows that ring-down times would be greater than 80 ns, i.e. twice the maximum total measurement bandwidth of the SPAD array, for cavity length above 45 cm. For this reason, cavity lengths shorter than 45 cm were used in this work, so that the SPAD could record as much of the ring-down decay as possible. This discussion shows that values for α_{min} are dependent on the cavity parameters. The theoretical minimum absorption coefficient, calculated from Equation 5.2 using results from Figure 5.8(c) (where the PMT $\Delta\tau_{\text{min}} = 2$ ns and $\tau_0 = 70$ ns), is estimated as $\alpha_{\text{min}} \approx 1 \times 10^{-3}\,\text{cm}^{-1}$. Values in the range $\alpha_{\text{min}} = 10^{-3}\,\text{cm}^{-1}$ to $10^{-7}\,\text{cm}^{-1}$ have been demonstrated in the liquid phase in previous published work [Alexander, 2006; Bahnev et al., 2005; Hallock et al., 2003; McGarvey et al., 2006; van der Sneppen et al., 2006; Xu et al., 2002]. It is worth noting that these values were obtained for single-channel CRDS measurements. The aim is to demonstrate sensitivity towards the higher end and across a broadband spectral range using the SPAD array rather than a single-channel detector.

SPAD Photosensitivity

Photon detection characteristics provided by the SPAD manufacturers are shown in Figure 5.9. The detection probability is the probability of a photon triggering an avalanche after it hits the SPAD active area. Note that this value does not include the fill factor efficiency, nor has the quantum efficiency been measured by the manufacturers for this prototype SPAD array. The array has its greatest photon detection sensitivity in the visible range [Stoppa and Mosconi, 2009] which

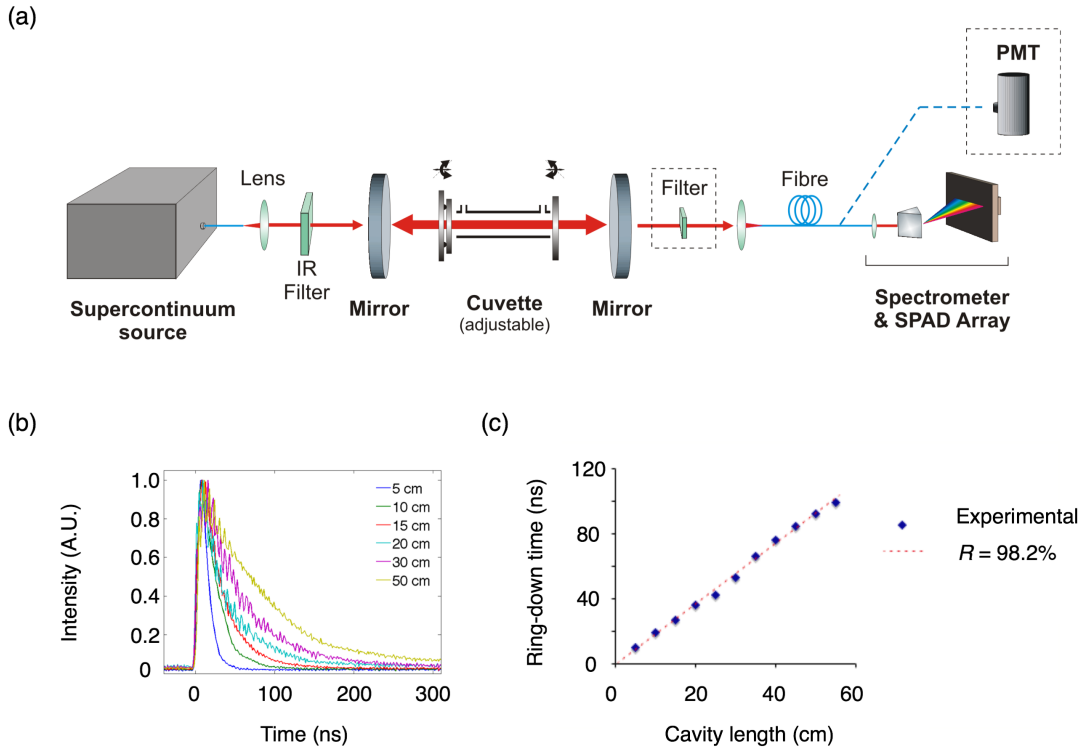

Figure 5.8: *(a) Test set-up for comparison of BB-CRDS measurements using the SPAD array with single channel CRDS (PMT arm). An IR short-pass filter is placed before the cavity, whilst interchangeable bandwidth filters are placed after the cavity to select different spectral ranges. (b) Measured ring-down times for optical cavities of different lengths over the narrowband spectral range* 530 nm *to* 570 nm *recorded using the PMT arm and a fast oscilloscope. Normalised experimental ring-down traces for* 5 cm, 10 cm, 15 cm, 30 cm *and* 50 cm *cavities. (c) Corresponding ring-down times for cavity lengths from* 5 cm *to* 55 cm. *Experimental data appear as points (blue); the modelled fit (red dotted line) is obtained for* R =98.2 %.

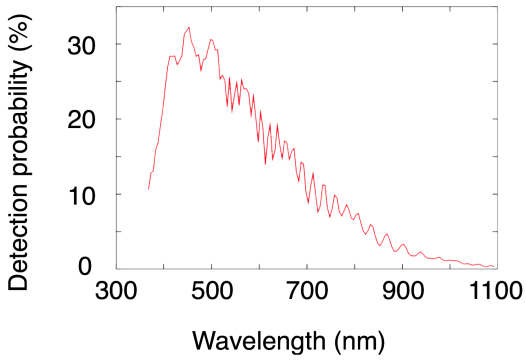

Figure 5.9: *SPAD photon detection characteristics for visible wavelengths. Figure reproduced courtesy of Stoppa and Mosconi [2009].*

makes it highly suited for liquid absorption techniques, due to the lower solvent absorption in this range (see previous discussion on solvent effects in Section 4.2 for more detail). By way of comparison, current multi-anode PMTs have quantum efficiencies ∼1 % to 10 % (taking into account the fill factor) in the visible range [Esposito, 2012].

Experimental Set-up

The set-up for the broadband cavity ring-down spectrometer is shown in Figure 5.10 [Kiwanuka et al., 2012]. A commercial supercontinuum source (SC-390, Fianium, UK) was used featuring a 1 MHz pulse repetition rate (variable from 500 kHz to 40 MHz) and 3 W average power in the wavelength range from 390 nm to 2400 nm. An interference filter (hot mirror, 716 GK 25, Comar Optics, UK), limited the SC output to visible wavelengths. The light was coupled into a 40 cm optical cavity formed by a pair of plano-concave mirrors (Layertec, 0.5 m radius of curvature, 99.0% nominal reflectivity from 400 nm to 680 nm). Details of the liquid sample cuvette can be found in Section 4.3 of the previous chapter. As previously discussed in Chapter 3, the use of higher reflectivity mirrors does not yield greater sensitivity as the absorption length in liquid samples is limited by intra-cavity losses due to solvent extinction [Pope and Fry, 1997] and also the presence of cuvette windows [Kiwanuka et al., 2010].

Light transmitted through the cavity was coupled with a lens (f = 50 mm)

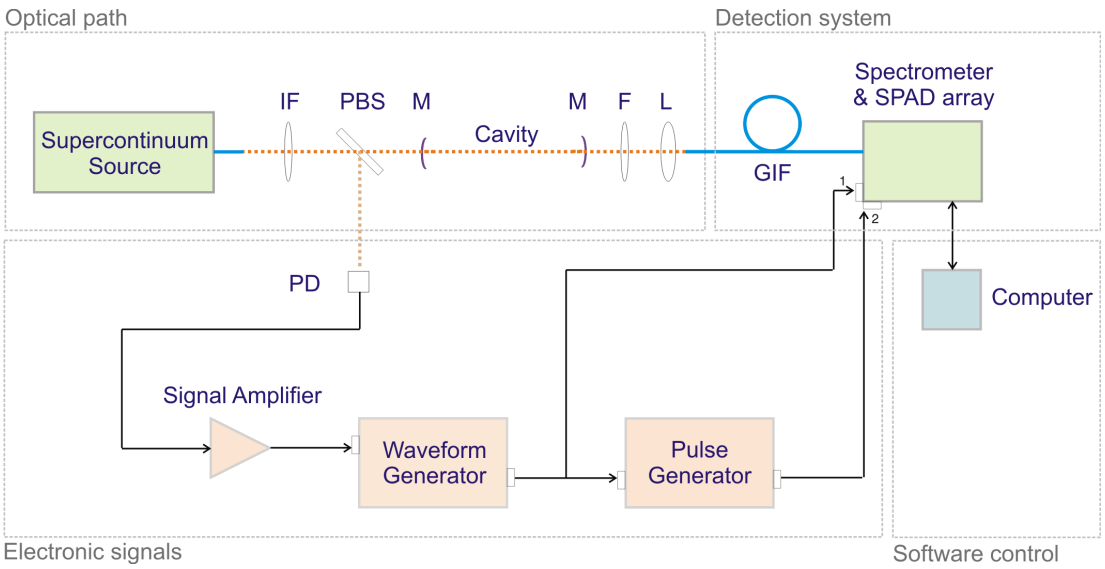

Figure 5.10: *Experimental BB-CRDS set-up for the study of liquid analytes. The collimated output from the SC source (SC-390, Fianium, UK) is spectrally filtered (IF= short-pass interference filter) to remove the IR light. The broadband light is coupled into the optical cavity formed by a pair of plano-concave mirrors (M). The optical cavity is used to pass light multiple times through the liquid sample contained in the* 5.4 cm *long intra-cavity cuvette. Narrow bandwidth spectral filters (F) are placed after the cavity, when required. This enables filters to be introduced and exchanged without disrupting the path or alignment of light entering the cavity. Light transmitted from the cavity is then coupled (L=lens) into a multimode fibre (GIF=graded index fibre) and then passed through a spectrometer and onto the SPAD array for detection. Electronic signals: A pellicle beam splitter (PBS) is used to select a portion (∼8%) of the SC light to enable individual pulse detection on a photodiode (PD). The signal from the detected pulses is amplified and then used to trigger the required waveforms and pulses which are then sent to the SPAD array (where 1=trigger signal, 2=SPAD clock signal). SPAD control software is operated with a standard computer.*

into a multimode fibre (GIF 625, Thorlabs, USA) and dispersed and focused onto the SPAD array to record individual cavity ring-down signals in up to 64 spectral channels. The power inside the cavity was ∼50 mW and <1 mW on the detector. The custom-built spectrometer comprised a lens (f = 6 mm), dispersion prism (SF11 - MgF_2 25 mm glass, Edmund Optics, USA), and a focusing lens (achromatic doublet, f = 20 mm). The width w_n and time point t_n of the four time gates were measured from the detector response to a short input laser pulse (<200 ps) at different time delays, t_0. Two electronic signals were fed to the SPAD array. A function generator (Agilent 33521A) set the initial delay, t_0, and a pulse generator (Stanford Research DG535) set the readout rate. Both units were triggered by individual supercontinuum pulses, as shown in Figure 5.10. A photodiode (DET210, Thorlabs, USA) and signal amplifier (SR445A, Stanford Research Systems, USA) were used for pulse detection. The use of external control electronics provided increased flexibility for testing the performance capabilities of the SPAD array in the proof of concept measurements presented in subsequent sections. The performance parameters of the used SPAD array are shown in Table 5.1.

Table 5.1: *Performance parameters of SPAD array [Pancheri and Stoppa, 2009].*

Parameter	Value
Active pixels	1 × 64
Pixel pitch	26 μm
Fill factor	34%
Maximum throughput rate	320 Mbps
Maximum output frame rate	150 kfps
Current consumption	200 mW @ 150 kfps
Chip size	3.3 × 3.2 mm
Time resolution	≤160 ps FWHM

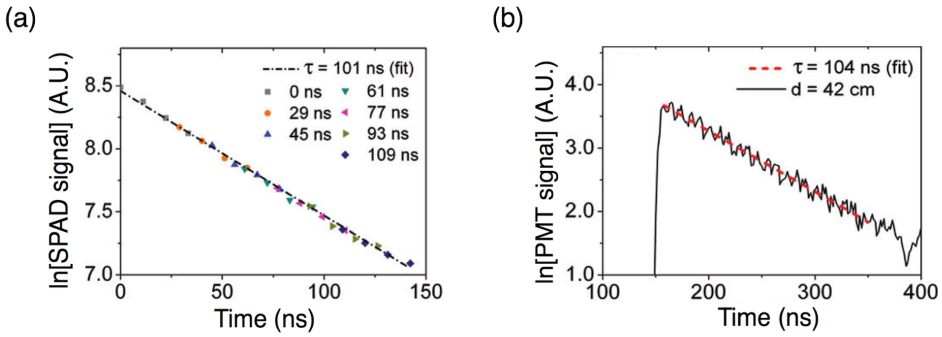

Figure 5.11: *Cavity ring-down measurements of pure water using a* 70 nm *band-pass filter centred at* 500 nm*. (a) Composite semi-log decay plot of SPAD array data obtained for different laser trigger time delays* t_0*. For each* t_0*, 4 individual data points are obtained (corresponding to* w_1 *to* w_4*). Each data point corresponds to spectral averages across all pixels over 250 shots. (b) Corresponding ring-down trace obtained with a PMT detector.*

5.5 Results and discussion

The ability of the BB-CRDS spectrometer to correctly sample different portions of a ring-down curve was first determined. In the configuration used in this work, the SPAD array was set-up to sample only a portion of the ring-down. The first test was to see whether the same ring-down time was measured when different sections of the ring-down decay were sampled. This was achieved by changing the initial laser trigger delay, t_0, so that the measurement time window fell over different portions of the exponential decay. The decay times for nine different trigger delays were plotted in Figure 5.11(a). By linear fitting of the slope one obtains $\tau = 101 \pm 5$ ns. For validation, the signal decay was also measured with a photomultiplier tube (PMT; R636-10, Hamamatsu, Japan) and an 8 GHz bandwidth digital oscilloscope (TDS6804B, Tektronix, USA), as depicted by the PMT arm in Figure 5.8. A ring-down time of 104 ± 1.8 ns was obtained with the PMT (see Figure 5.11(b)), which is within 4% agreement with the SPAD data. The bandwidth of the transmitted light was filtered to a width of 70 nm centred around 500 nm for both SPAD and PMT measurements in Figure 5.11.

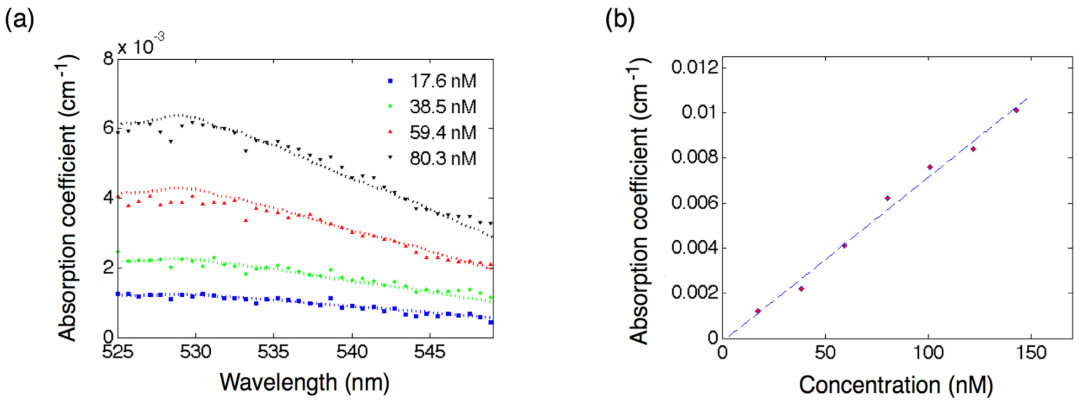

Figure 5.12: *(a) Broadband CRDS spectra of rhodamine 6G at concentrations from* 17.6 nM *to* 80.3 nM *in* 18 MΩ cm^{-1} *ultrapure water. Signal integration times were* 100 ms*, corresponding to ∼100,000 individual supercontinuum pulses. Dashed lines represent reference spectra obtained with SC-CEAS. (b) Calibration curve for rhodamine 6G (Rh6G) measurements in the concentration range* 17.6 nM *to* 142.9 nM *obtained from BB-CRDS using the SPAD detection system. Absorption coefficient values are taken at the peak value for absorption coefficient.*

Proof of Principal Measurement

The detection limit was estimated from measurements of various concentrations of rhodamine 6G (Rh6G; Sigma Aldrich, USA) dissolved in ultrapure water (18 MΩ cm^{-1} Milli-Q, Millipore, USA), as shown in Figure 5.12(a). The total sample volume in these measurements was 1.0 mL. The value of $\alpha_{\min}$ was determined from the 1σ baseline noise in measurements of α (obtained from Equation 5.1) for different measurements of blank samples. This was found to be 3.2×10^{-6} cm^{-1} Hz$^{-1/2}$ at a spectral resolution of 0.7 nm per pixel. The limit of detection (LOD) for these time-resolved measurements was calculated using LOD=$3\alpha_{\min}/2.303\epsilon$ [Seetohul et al., 2009], giving a minimum detectable concentration of 360 pM for rhodamine 6G ($\epsilon = 116\,000$ M^{-1} cm^{-1} at 529.75 nm).

These BB-CRDS results are comparable to those achieved using single wavelength liquid-phase CRDS techniques [van der Sneppen et al., 2010; Xu et al., 2002]. An increase in effective path length of approximately 50 times the cuvette length

enabled higher sensitivity to be achieved. A linear response was obtained for Rh6G measured in the concentration range 17.6 nM to 142.9 nM, with a root mean square error of RMSE = $2.8 \times 10^{-4}\,\mathrm{cm}^{-1}$, as shown in Figure 5.12(b). Figure 5.12(a) shows BB-CRDS spectra of Rh6G and, for comparison, broadband SC-CEAS measurements as described in Kiwanuka et al. [2010] and Chapter 4. The general agreement between the results obtained by these independent techniques is very good although some wavelength-dependent systematic differences can be seen. This is most likely caused by differences in the relative pixel sensitivities and spectral throughput between the two approaches. The signal from each time-gate was integrated for 100 ms (∼100,000 shots) before the SPAD array was read out. Stelmaszczyk et al. [2009] showed integral smoothing to be effective for exponential signals.

5.6 Conclusions

A spectrometer for sensitive absorption measurements in liquids across broad spectral bandwidths that is both insensitive to spectral intensity variations and calibration-free is presented here. The spectrometer combines the unique spectral properties of incoherent supercontinuum light sources with the advantages of cavity ring-down spectroscopy using a custom-built avalanche photodiode array for detection. This enables the simultaneous measurement of ring-down times for up to 64 different spectral components at nanosecond temporal resolution. The minimum detectable absorption coefficient was measured to be $3.2 \times 10^{-6}\,\mathrm{cm}^{-1}\,\mathrm{Hz}^{-1/2}$ at 527 nm.

In comparison, the SC-CEAS technique achieved higher sensitivity and the detection CCD featured a larger number of pixels to enable either higher resolution or broader spectra to be recorded. By contrast, BB-CRDS measurements taken here are self-referencing and insensitive to light source fluctuations. The SPAD array detector used is much less expensive and more compact than the EM-CCD and spectrometer used for SC-CEAS in Chapter 4. However, both techniques have their own relative advantages. Based on the demonstration here in this chapter of liquid-phase BB-CRDS, believed to be the first, this technique shows its potential as a compact, calibration-free sensor. Due to the scalability of CMOS

production methods the technique could be developed into a flexible and cost-effective sensor technology in the future. Further enhancements in CMOS-based SPAD detector technology can be envisaged, leading to sensitivity improvements. For example, improved fill factors could be achieved through the use of microlens arrays [Randone et al., 2009] and better performance through increases in the number of time-gates and photosensitive pixels.

Chapter 6

Application of Cavity-enhanced Liquid Sensing

Introduction

The development of two cavity-enhanced techniques has been described in Chapters 4 and 5. This chapter focuses on the application of both techniques. The overall aim of this thesis is not only to develop a sensitive spectroscopic techniques, but also to demonstrate their capabilities as applied to scientific problems. Four applications have been selected for this purpose:

(i) Spectroscopic monitoring of an oscillating reaction (p. 98).

(ii) Detection of technologically important trace metal lanthanide ions to aid further investigation of their luminescent properties (p. 107).

(iii) Near-UV sensing of protein aggregation related to research into neurodegenerative conditions such as Alzheimer's Disease (p. 116).

(iv) Use of liquid BB-CRDS for analysis of blood samples (p. 127).

The following sections highlight the recent technological advancements that have enabled the above studies to be undertaken, along with any additional experimental considerations.

6.1 Monitoring oscillating reactions

Introduction: Aims and Objectives

The aim of this section is to investigate the potential of SC-CEAS in its use in reaction monitoring. Spectral measurements of non-reacting liquid species were made in Chapter 4. The motivation here is to monitor an oscillating reaction. This is to provide an initial demonstration of the technique's ability to measure dynamic systems.

6.1.1 Background to reaction monitoring

In the process industry it is often important to control the consumption rate of reagents or the formation rate of products. More detailed analysis of reactions can provide information on the overall reaction mechanism, intermediate states and/or whether equilibrium has been reached. These factors can help one better understand how to further optimise the process. Furthermore, a number of these factors can be externally influenced by controlling physical parameters such as temperature, pressure or the use of a catalyst. Therefore, quantitative analysis can be used in the evaluation of the effects of such changes.

Chemical reactions proceed from an initial state to a final state over a given period of time. Take for instance, the timescales of different biological processes. Photobiology is a key process in nature and methods such as photosynthesis can occur on the order of 1 ps [Rentzepis, 1978]. Neurotransmitter binding is a few orders of magnitude slower in the microsecond range whereas protein emergence after gene expression may take up to 100 s [Lodish et al., 2000]. The reagents and products may absorb different wavelengths of light, thus requiring broad enough spectral bandwidth to detect their respective spectra during the reaction. Detection sensitivity would also be required if concentrations of constituents involved in the reaction are low.

There are a number of analytical techniques for reaction monitoring such as conductivity for measurement of ionic mixtures, mass spectrometry, polarimetry, gas chromatography and titration. Such techniques may have specific constraints such as requiring paramagnetic samples or fluorescent molecules. Optical absorp-

tion techniques have the advantage that most molecules interact with light and, assuming sufficient sensitivity, can be detected. Spectrophotometry is one particular technique that is widely used for reaction monitoring, based on the amount of light absorption of different molecules. For this initial proof of concept it is, therefore, necessary to find a suitable reaction.

Requirements for Initial Demonstration

Optical change: SC-CEAS is capable of sensitive measurements across the visible range in a single-shot, i.e. without the need for sequential scanning. Therefore, a reaction that undergoes a distinct spectral change should be chosen in order to demonstrate the optical capabilities of the technique across the visible spectrum, i.e. spanning 200 nm to 300 nm in bandwidth.

Time resolution: The single-shot spectral acquisition times demonstrated in Chapter 4 were on the scale from 10 ms to 50 ms. The chosen reaction should thus occur on the suitable timescale so that changes can be captured by the technique.

6.1.2 What are oscillating reactions?

Some reactions do not simply proceed in one forward direction from initial to final state. Instead, they oscillate back and forth from one state to another in a rhythmic fashion. These so-called oscillating reactions were first discovered in 1950 by Boris Pavlovich Belousov, who noticed a periodic colour change in a reaction mixture. Heterogeneous oscillating reactions had of course been discovered electrochemically over a century earlier by Fechner [1828] and then Ostwald [1899, 1900] who followed the corrosion mechanism of chromium and iron in different acids. Belousov [1959] noticed oxidation of citric acid with brominated sulphuric acid exhibited an oscillatory behaviour in the condensed phase. This was only when cerium ions acted as a catalyst. The solution changed from yellow to colourless and then back again over a period of oscillations. The reaction is often referred to as a "chemical clock reaction" exhibiting periodic oscillations which can be monitored in time [Hegedus et al., 2002]. It was the work of A.M. Zhabotinsky that created a theory for these oscillations through further modelling based on extensive experimental data that proved their importance for later study of

thermodynamics and equilibrium systems [Zhabotinsky, 1964; Zhabotinsky and Zaikin, 1971]. Zhabotinsky was able to observe oscillation of larger amplitude by replacing citric acid with malonic acid.

The Belousov-Zhabotinsky (BZ) reaction is unique in that it provides spatial and temporal information. The spatial propagation can provide information on chemical wave formation and pattern propagation in media, whereas temporal information can be provided by composition. The importance of this is clear from the stand point of chemistry or physics, but there is also biological significance. Oscillating reactions are a form of self-organisation in time, similar to embryonic formation. The focus in this work is on the temporal evolution. The advantage of using an oscillating reaction is that it provides multiple opportunities to detect spectral changes for the purpose of this initial demonstration. The response of the system can also be checked and compared across a number of oscillations.

6.1.3 Methodology: Belousov-Zhabotinsky reaction

Temporal Behaviour of Oscillations

The BZ reaction will be modelled first to see whether oscillations occur on a suitable timescale for the technique in its current configuration. The "Oregonator" is one of the simplest models for modelling oscillatory behaviour in a chemical reaction [Noyes and Field, 1974]. The dynamics are based on coupled stoichiometries of the system and a set of differential equations can be set out to describe the concentration change of the reactants and products as a function of time [Epstein and Pojman, 1998]. The model used to simulate the BZ reaction in this work was taken from Deuflhard and Bornemann [2002]. The reaction scheme is presented on the following page.

$$\mathrm{BrO_3^-} + \mathrm{Br^-} \longrightarrow \mathrm{HBrO_2}, \tag{6.1}$$
$$\mathrm{HBrO_2} + \mathrm{Br^-} \longrightarrow \mathrm{P}_\alpha, \tag{6.2}$$
$$\mathrm{BrO_3^-} + \mathrm{HBrO_2} \longrightarrow 2\,\mathrm{HBrO_2} + \mathrm{Ce(IV)}, \tag{6.3}$$
$$2\,\mathrm{HBrO_2} \longrightarrow \mathrm{P}_\beta, \tag{6.4}$$
$$\mathrm{Ce(IV)} \longrightarrow \mathrm{Br^-}. \tag{6.5}$$

where P stands for organic products (where $\mathrm{P} = \mathrm{P}_\alpha + \mathrm{P}_\beta$). The rate of change of reactant concentration is given by the following set of equations:

$$d[A]/dt = -k_1[A][X] - k_3[A][Y], \tag{6.6}$$
$$d[X]/dt = -k_1[A][X] - k_2[X][Y] + k_5[Z], \tag{6.7}$$
$$d[Y]/dt = k_1[A][X] - k_2[X][Y] + k_3[A][Y] - 2k_4[Y]^2, \tag{6.8}$$
$$d[P]/dt = k_2[X][Y] + k_4[Y]^2, \tag{6.9}$$
$$d[Z]/dt = k_3[A][Y] - k_5[Z]. \tag{6.10}$$

where k_i is the rate of reaction for Equation 6.i (for $i = 1 - 5$), [A] = $\mathrm{BrO_3^-}$, [X] = $\mathrm{Br^-}$, [Y] = $\mathrm{HBrO_2}$, [P] = P and [Z] = Ce(IV). The evolution of $\mathrm{Br^-}$ and $\mathrm{HBrO_2}$ concentration, along with other reactants, is shown in Figure 6.1. After an initial delay, oscillations appear within a period of about 40 s to 45 s. Continuous measurement with SC-CEAS over a few minutes will be sufficient to detect a number of oscillations.

Detecting Spectral Changes

The BZ reaction studied here involves the reduction of cerium(IV) to cerium(III) ions by malonic acid and the oxidation using bromate(V) back to cerium(IV) ions. The Ce(IV) oxidation state is yellow in colour whereas Ce(III) is colourless; therefore, oscillations in colour occur which correlate with Ce(IV) concentration. Peaks in CE(IV) concentration coincide with those of both $\mathrm{HBrO_2}$ and $\mathrm{Br^-}$ throughout the reaction, as shown in Figure 6.1. The equilibrium for the Ce(IV)/Ce(III)

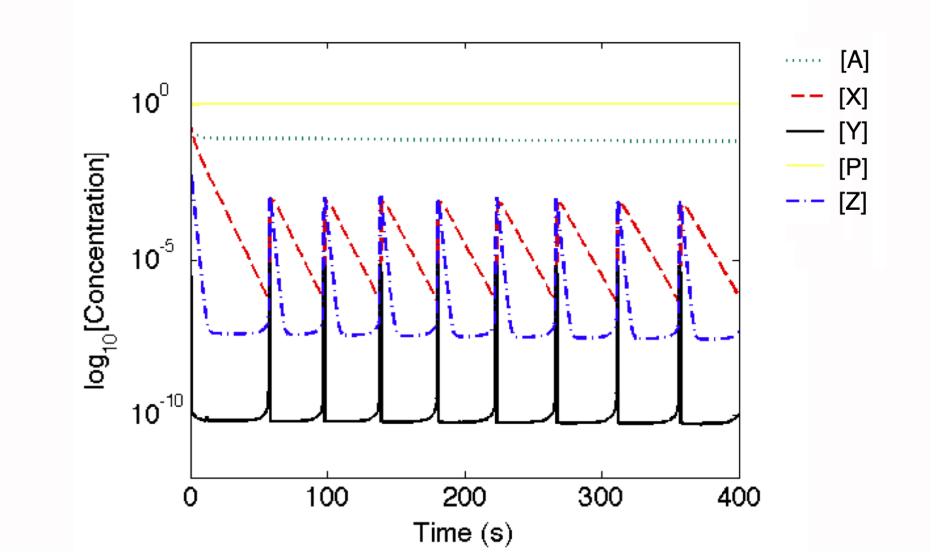

Figure 6.1: *Modelled temporal evolution of BZ reactant concentration as a function of time. Initial concentrations are [A]* $= BrO_3^- = 0.17\,\mathrm{M}$, *[X]* $= Br^- = 0.26\,\mathrm{M}$, *[Y]* $= HBrO_2 = 0.085\,\mathrm{M}$, *[P]* $= P = 0.83\,\mathrm{M}$ *and [Z] = Ce(IV)* $= 0.008\,\mathrm{M}$. *The reaction constants (taken from Deuflhard and Bornemann [2002]) are* $k_1 = 1.34\,\mathrm{M}^{-2}\,\mathrm{s}^{-1}$; $k_2 = 1.6 \times 10^9\,\mathrm{M}^{-2}\,\mathrm{s}^{-1}$; $k_3 = 8.0 \times 10^3\,\mathrm{M}^{-2}\,\mathrm{s}^{-1}$; $k_4 = 4.0 \times 10^7\,\mathrm{M}^{-2}\,\mathrm{s}^{-1}$; *and* $k_5 = 1.0\,\mathrm{M}^{-1}\,\mathrm{s}^{-1}$.

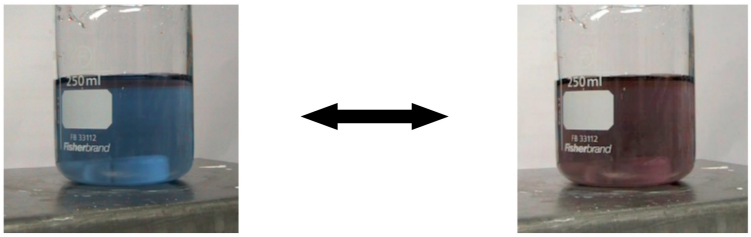

Figure 6.2: *Ferroin indicator colour change at either extremity of the oscillating Belousov-Zhabotinsky (BZ) reaction. The oxidised form $[Fe(phen)_3]^{3+}$ appears in blue, as shown on the left, and the reduced form $[Fe(phen)_3]^{2+}$ appears red, shown on the right.*

couple is summarised in Equation 6.11.

$$BrO_3^- + 4\,Ce(III)_{(aq)} + 5\,H_3O^+ \rightleftharpoons 4\,Ce(IV)_{(aq)} + 7\,H_2O, \tag{6.11}$$

$$\underset{\text{yellow}}{Ce(IV)_{(aq)}} + \underset{\text{red}}{[Fe(phen)_3]^{2+}} \rightleftharpoons \underset{\text{colourless}}{Ce(III)_{(aq)}} + \underset{\text{blue}}{[Fe(phen)_3]^{3+}}. \tag{6.12}$$

The oxidation step of the reaction involves bromomalonic acid, an autocatalytic intermediate, which is critical to the self-propagating oscillations. For spectroscopic analysis of the reaction, ferroin indicator is used as it exhibits a stronger colour change from red to blue upon oxidation in the reaction step. The role of ferroin as an electron transfer agent for this BZ reaction is shown in Equation 6.12 [Franck, 1978]. The oxidised form of ferroin has a blue colour, whereas the reduced form is red. This colour change is shown in Figure 6.2 at the bench scale and much higher concentration. Traditionally, the change in electrode potential has been used to determine this redox change, using platinum working electrodes and saturated Hg_2SO_4 at the reference electrode. The colour change which was replicated at much higher concentrations at bench-scale volumes (see Figure 6.2), is distinct enough to be monitored spectrally.

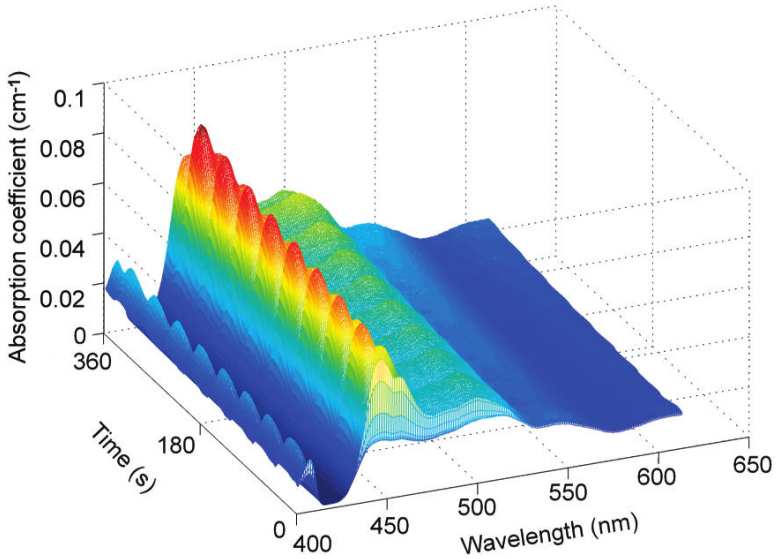

Figure 6.3: *Oscillating Belousov-Zhabotinsky reaction recorded using SC-CEAS. The periodic transition between Fe^{II} and Fe^{III} oxidation states is easily observed in the closed (unstirred) cuvette. Spectra (averaged over 1,000 single-shots) with* 250 nm *spectral bandwidth were acquired at* 2.75 Hz *rate using* 50 ms *exposure time. The period of oscillation of the medium is* 44 s*, as shown in the above 3D plot. Initial concentrations in* 1.0 M H_2SO_4 *solvent were potassium bromate* = 0.17 M*, potassium bromide* = 0.26 M*, malonic acid* = 0.83 M*, ceric ammonium nitrate* = 0.008 M*, ferroin indicator* = 1.0 M*.*

6.1.4 Results and discussion

In this work, the BZ reaction was monitored over a period of 6 min using 50 ms exposure time per spectral reading. The experimental set-up is exactly as described in Section 4.3. Figure 6.3 shows 1000 single-shot spectra ranging from 400 nm to 620 nm, acquired at 2.75 Hz repetition rate. Higher acquisition rates are clearly possible at 50 ms exposure time but not required here as the oscillation period of the reaction was measured to be 44 s (see Figure 6.3). The changes in spectra permit the relative proportions of ferroin in its unoxidised (red) and oxidised form (blue) to be detected at any time point during the reaction. This is a clear advantage of the multiplexing capability of the technique. In this work, up to 50 individual spectra have been averaged. The total sample volume was 2.7 mL.

The theoretical models used in the previous section are based on continuously stirred systems [Field et al., 1972]. An effective method of stirring has yet to be implemented in the current experimental design, therefore the sample in this SC-CEAS measurement remained unstirred. This may account for the slight discrepancy between the experimental results and theoretical simulations. Measurements in Figure 6.3 were taken once the system was oscillating, i.e. after the "induction phase", which is defined as the sometimes extended period of time before the first oscillation (see Figure 6.1). Information on the effects of malonic acid, bromate ion and cerium initial concentrations can be found in more detailed studies and discussions by Field et al. [1972], based on their investigations of a stirred system.

Summary and Future Work

The oscillating Belousov-Zhabotinsky reaction was successfully monitored with SC-CEAS as an initial demonstration of the technique's potential for reaction monitoring. This result extends the previous broad spectral bandwidth measurements of non-reactant species at low concentration (see Chapter 4), further demonstrating the broad applicability of the technique. Dynamic measurement, or so-called "on-line" analysis, of products is important in process industry for a number of different reasons, for example, quality control, pollutant detection and/or health and safety monitoring.

The BZ reaction and the Oregonator model are also of interest outside the realm of basic chemistry. Biologists are interested as the BZ reaction may be used to develop models of biological events. Two such examples are the dynamics of slime mould in a petri dish and the onset of ventricular fibrillation as manifested by waves of contraction in heart tissue [Shanks, 2001]. SC-CEAS could thus represent an experimental tool that could be used in corroborating results from adjustments to and re-interpretations of the theoretical Oregonator model.

Future work could involve either integrating the SC-CEAS technique into current process systems or, alternatively, modifying the current set-up to enable more detailed studies. For instance, simple adaptation of the apparatus, e.g. addition of heating elements and thermocouples around the cuvette would permit

the temperature-dependent behaviour of this and other systems to be observed. The spectral bandwidth is broad enough to detect simultaneously different analytes in the condensed phase and even faster reactions than the one shown here can be observed on millisecond timescales. One potential limitation is the sample volume size, which at 2.7 mL is relatively small but may be too large for reactions occurring on the micro-fluidic scale. Nevertheless, recent cavity-enhanced micro-fluidic set-ups can achieve microlitre volumes but do so by sacrificing sensitivity, with sensitivity in the $10^{-3}\,\mathrm{cm}^{-1}$ to $10^{-2}\,\mathrm{cm}^{-1}$ range [Neil et al., 2011].

6.2 Europium and the quantification of Lanthanides

Introduction: Aims and Objectives

Lanthanides are rare earth metals used in a number of high-tech applications as well as for more basic manufactured products. They are of scientific interest due to their photophysical properties, in particular, their high luminescence. Use of lanthanide has increased in recent decades and, as a result, researchers are looking at ways to improve the design of such complexes. At present, there are few methods capable of detecting lanthanides at low concentration in order to quantify their absorbance properties. Consequently, the author was approached by a researcher within the field to see whether SC-CEAS could provide a solution. The aim here was to detect different lanthanide species in solution at low concentration. SC-CEAS was used to quantify absorbance of different complexes and see which electronic transfers can be detected in order to provide designers of lanthanide complexes with previously unobtainable information. The results of this investigation are set out in Section 6.2.4.

6.2.1 Background to Lanthanides and their uses

The lanthanide series contains the rare earth elements of atomic number 57 to 71, as shown in the periodic table (Figure 6.4). There are a multitude of uses of lanthanides and they have found even more applications in recent decades. The emergence of novel technologies has seen their application as part of high-temperature superconductors, in batteries for hybrid cars and next-generation magnetic refrigeration schemes, as well as more traditional applications such as lighter flints and glass polishing [Haxel et al., 2002]. Lanthanides are gradually replacing other metals due to their low toxicity and weight. Praseodymium (Pr), neodymium (Nd), samarium (Sm), gadolinium (Gd) and dysprosium (Dy) have all been used in miniaturised, high strength magnets for consumer electronics devices and telecommunication systems [Haxel et al., 2002; Naumov, 2008].

Lanthanides are categorised according to whether they are found in minerals in the Earth's crust (predominantly so-called light lanthanides, e.g. cerium) or in

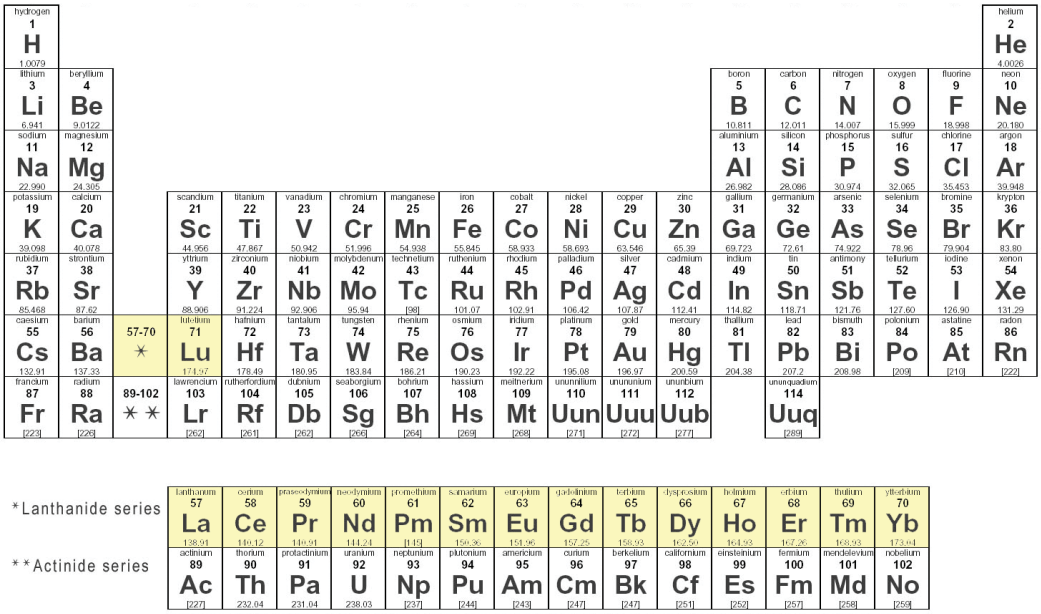

Figure 6.4: *Periodic table of elements with the lanthanide series (atomic numbers 57-71) highlighted.*

the mantle (heavy lanthanides, i.e. Gd to Lu). Even so, they display remarkably similar chemical properties across the entire group [Moeller, 1970; Pimentel and Sprately, 1971]. From a photophysical perspective, lanthanides are of extreme interest due to their heightened response to specific wavelengths of light in the visible and near-IR. This is fundamentally due to their electronic configuration. Lanthanides predominantly exist as trivalent cations Ln^{III} ([Xe]$4f^n$, n = 0-14) in aqueous form and it is these transitions of electrons in the f-orbital that give rise to the unique properties of lanthanide ions, including sharp absorption and emission lines in addition to strong luminescence with long lifetimes [Pimentel and Sprately, 1971].

Ytterbium is a well-known dopant for the active medium in solid state lasers [Lacovara et al., 1991]. The 1060 nm fibre laser used in this work (see Chapter 4) in fact contains two lanthanides in its neodymium-doped yttrium aluminium garnet (Nd:YAG) crystal, first demonstrated as a laser gain medium by Geusic et al. [1964] at Bell Laboratories. Lanthanides also play an important role in the telecommunications industry. Long runs of fibre-optic cabling are commonly interspliced with erbium-doped fibre sections and amplifiers.

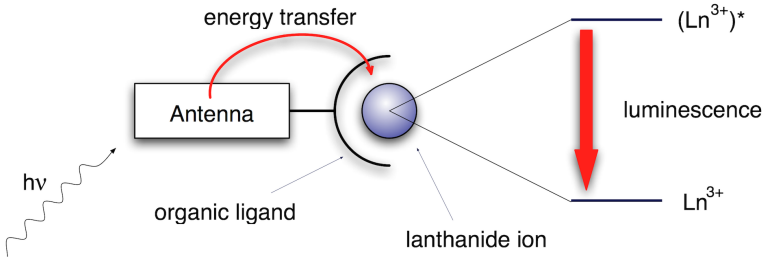

Figure 6.5: *Schematic diagram of lanthanide ion excitation via organic ligand acting as an "antenna" and subsequent luminescence. Light absorbed by the ligand is transferred to its triplet state and then to the lanthanide ion.*

6.2.2 Lanthanide photophysics and electronic transitions

Absorption spectroscopy is an important tool in the study of lanthanides as it can be used to determine electronic structure [Görller-Walrand and Binnemans, 1998]. The difficulty is that lanthanide ions do not readily absorb light which is why their molar extinction coefficients are very low. Direct excitation is difficult as $f - f$ electronic transitions are forbidden by the Laporte rule [Laporte and Meggers, 1925; Morrison and Leavitt, 1982]. Energy transfer must then occur via an alternative pathway where the overall quantum yield is dependent on the ease with which excited state(s) can be populated. Organic chromophores are much better at absorbing light and when used as ligands on a lanthanide ion, can act as "antennae", transferring absorbed energy to the lanthanide ion, as shown schematically in Figure 6.5.

Indirect excitation, also referred to as antenna effect or sensitisation, is what ensures Ln^{III} have high luminescence. The three stages of the process are: (i) absorption of light by attached organic ligands; (ii) energy transfer to one or more of the excited states of Ln^{III}; and (iii) emission of light [Latva et al., 1997; Wilson et al., 2010]. This process of ligand(S_1) $\rightarrow$ ligand(T_1) $\rightarrow$ Ln^{III*} energy transfer is shown in Figure 6.6 in terms of the different energy levels [de Sá et al., 2000; Gonçalves e Silva et al., 2002; Gutierrez et al., 2004]. The energy gap between the lowest lying excited (emissive) state of the lanthanide ion and highest sublevel of its ground multiplet dictates the intrinsic quantum yield. Lanthanides display large enough energy gaps which make them less likely to close due to

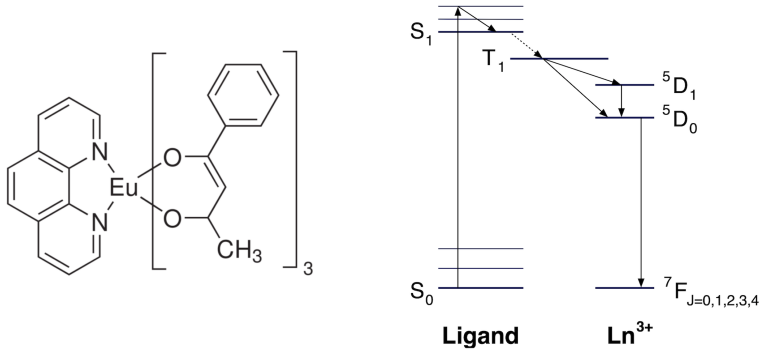

Figure 6.6: *Chemical structure of the Eu-tBA complex and energy transfer path for lanthanide luminescence via ligand excitation and resonance energy transfer. Absorption and emission processes are shown.*

non-radiative deactivation.

Researchers of lanthanides ions and their complexes are interested in determining their quantum yield (QY). Accurate determination of QY will aid the design of new complexes with improved photophysical characteristics. The emission lifetime is straight-forward to measure via fluorescence techniques [Frank et al., 2007]. However, QY determination requires calculation of the radiative lifetime. The radiative lifetime is defined as the radiative decay of an electronic state by spontaneous emission only and in the absence of any non-radiative effects [Edwards, 1966; Fowler and Dexter, 1962]. Eu^{3+} ions have non-degenerate ground states and absorption in the visible, making them attractive for spectroscopic analysis. Although Eu^{3+} has a number of absorption peaks in the visible, many are too weak which is why complexes and compounds generally appear colourless in solution and white in powder. The work here focuses on the detection of Eu^{3+} in solution, to see whether SC-CEAS can provide a better method for initial spectroscopic analysis.

6.2.3 Methodology: Detection of Europium

There are four main questions to be addressed in this section:

(i) Does SC-CEAS have the required sensitivity to detect weak lanthanide absorption peaks in the visible?

(ii) How many transitions can be detected within the given spectral bandwidth of the technique?

(iii) Is there sufficient spectral resolution to resolve the different transitions?

(iv) Can different solvents be used with the current SC-CEAS set-up?

A previous investigation by Sawada et al. [1979] identified several spectral features of Eu^{3+} aqueous ion in the visible spectrum from 400 nm to 600 nm. This will be the spectral region of investigation in this work. Different ligand environments require different solvents. The only modification to the SC-CEAS set-up described in Section 4.3 is the use of a glass cuvette tube element instead of an acrylic one. The glass cuvette tube is suitable for use with almost all conceivable solvents which is important as corrosive solvents, such as dichloromethane, have been used with Eu^{3+} complexes [Moudam et al., 2009]. The glass cuvette tube has the same dimensions as the PMMA version and is also easy to replace. All other aspects of the set-up, e.g. equipment configuration and optical pathlength, remain the same as in Section 4.3.

6.2.4 Results and discussion

Europium Salt

A europium salt was first investigated in order to identify whether different transitions could be detected with SC-CEAS. Figure 6.7 shows a spectrum of europium(III) nitrate hydrate ($Eu(NO_3)_3 \cdot 5H_2O$, Sigma Aldrich, UK) dissolved in ultrapure water (18 $M\Omega\,cm^{-1}$ Milli-Q, Millipore, USA) at 50 and 100 mM concentrations in the spectral range 410 nm to 600 nm. The total cuvette sample volume was 1.0 mL. Sawada et al. [1979] used photo-acoustic spectroscopy to detect Eu^{3+} oxide dissolved in nitric acid at 200 mM and estimated a limit of detection of 100 mM. The results here show SC-CEAS to be more sensitive than those measurements. A minimum detectable absorption coefficient of $3.0 \times 10^{-6}\,cm^{-1}\,Hz^{-1/2}$ at 591 nm was estimated for a 1 s total acquisition time. This corresponds to a limit of detection (3σ) of $150 \pm 50\,\mu M$. The spectra cover nearly two-thirds of the visible.

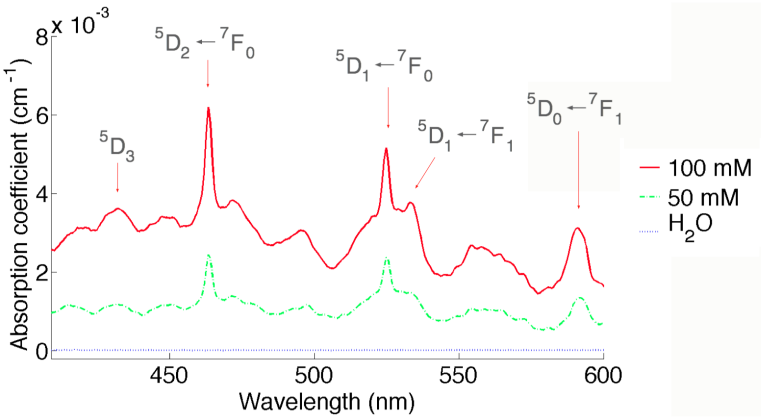

Figure 6.7: *Absorption spectrum of europium(III) nitrate hydrate at* 50 mM *and* 100 mM *dissolved in* 18 MΩ cm^{-1} *ultrapure water. The water (solvent) baseline is shown on the plot in blue. The spectra were acquired using* 20 ms *single-shot exposure time. Averages of 50 single-shot spectra are shown for each concentration corresponding to a total acquisition time of* 1 s.

Figure 6.7 shows five Eu^{3+} transitions from 415 nm to 600 nm in the visible. The $^5D_0 \leftarrow {}^7F_1$ transition appears at 592 nm. Spectral broadening in aqueous solutions, as discussed in Section 4.2, prevents individual peaks in this and other transitions from being resolved. This same transition would appear as three distinct peaks in absorption spectra of single crystals doped with lanthanide ions and solid lanthanide salts [Binnemans and Görller-Walrand, 1997]. The transition $^5D_0 \leftarrow {}^7F_0$ is spin forbidden and thus does not appear in the spectrum. The weak transition $^5D_1 \leftarrow {}^7F_1$ is at 535 nm and $^5D_1 \leftarrow {}^7F_0$ appears at 526 nm. The transition $^5D_2 \leftarrow {}^7F_0$ appears at 464 nm with transitions to $^5D_3$ in the violet (i.e. <450 nm).

The lanthanide ion has only weak interactions with the ligand. The $4f^N$ electrons of the lanthanide ion have a smaller radial extension and are thus strongly shielded from external charge by the more diffuse filled $5s^2$ and $5p^6$ orbitals [Dunlap and Lander, 1974]. As a result, overlap with ligand electronic orbitals is small. However, there is sufficient interaction to produce the fine spectral structure observed in spectra. Detailed discussion of transitions and associated photophysics can be found in Görller-Walrand and Binnemans [1998]. Some transitions in the visible spectrum are highlighted in Figure 6.7 to demonstrate the sensitiv-

ity achievable and spectral information obtainable with SC-CEAS. For example, the positions of the peaks will correspond to the $4f^N$ structure and the relative intensity of peaks reflects interaction between the lanthanide ion and its environment.

Europium Complex

The measurement of europium salts provides a starting point in this investigation, but it is europium complexes that are of greater interest as they have more exotic spectroscopic properties [Gutierrez et al., 2004]. Electronic excitation in lanthanides has briefly been discussed, yet in reality deactivation through non-radiative processes can also occur. For example, temperature-dependent multi-phonon processes can also lead to deactivation [Hüfner, 1978], and O-H vibration in aqueous solutions leads to severe quenching [Beeby et al., 1999]. Quenching effects can be minimised by limiting high-energy vibrations, collision-induced deactivation and solvent interactions. One method of achieving all of this is through rigid design of ligands [Bünzli and Piguet, 2005].

The europium(III) complex $C_{42}H_{35}Eu(No_3)_2$ (Sigma Aldrich, USA; referred to from hereon as Eu-*t*BA) was chosen for analysis. Its chemical structure is shown in Figure 6.6. Eu-*t*BA was dissolved in dimethyl sulphoxide (DMSO) and its resultant spectrum shown in Figure 6.8. The total sample volume was again 1.0 mL. Werts et al. [2002] showed that the spectra of aqueous Eu^{3+} vary depending on the surroundings, i.e. ligand environment. However, the absorption strength of the $^5D_0 \leftarrow {}^7F_1$ transition was shown to be independent of the ligand environment [Werts et al., 2002]. This transition, highlighted in Figure 6.8, is often taken as the reference for dipole strength. The 3σ standard deviation of each measurement is shown on the plot, denoted by the grey shaded region.

As part of general experimental observations, a very slight pink hue was observed in the light beam as it passed through the sample. This the result of Eu^{3+} luminescence [Cotton, 1991; Lagowski, 1973; Main Smith, 1927; Shriver and Atkins, 1999]. Pink is not a spectral colour, but in fact red when viewed in strong white light or against a strong white background. It is this phosphorescence that has long been exploited for cathode ray tubes in traditional television

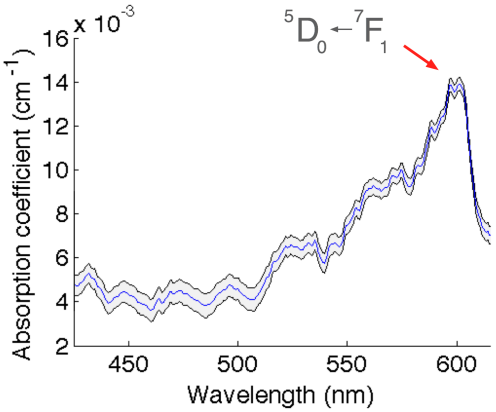

Figure 6.8: *Absorption spectrum of* 2 mM *Eu-tBA complex dissolved in DMSO. One standard deviation (1σ) of the calculated absorption coefficient is represented with the grey shaded area. The spectrum was acquired using* 20 ms *single-shot exposure time and an average of 50 frames, corresponding to a total acquisition time of* 1 s.

sets using YVO_4:Eu^{3+}, Y_2O_3:Eu^{3+} and Y_2O_2S:Eu^{3+} [McColl and Palilla, 1981].

Summary and Future Work

In this work, Europium ions were detected in solution at low concentrations (50 mM to 100 mM) and a limit of detection of $3.0 \times 10^{-6}\,\mathrm{cm^{-1}\,Hz^{-1/2}}$ at 591 nm calculated for $Eu(NO_3)_3 \cdot 5H_2O$ dissolved in ultrapure water. To the best of the author's knowledge, this is lower than any value quoted in the literature. Five key transitions in the spectral range 400 nm to 600 nm were detected. This investigation has shown that the technique is capable of handling a variety of different solvents and thus analysing lanthanides in different ligand environments. A europium complex (Eu-*t*BA) at 2 mM concentration was detected in DMSO. There is sufficient spectral resolution and bandwidth to identify key electronic transitions, as highlighted in the spectra shown from experimental analysis. The small sample volumes of 1.0 mL are also important in this application as complexes may either be very expensive, or difficult to synthesise and, therefore, available for analysis only in small quantities.

The spectral information here can enable the radiative lifetime of Eu^{3+} to be calculated using the strength of the $^5D_0 \leftarrow {}^7F_1$ transition to correct the emis-

sion spectrum [Werts et al., 2002]. This in turn enables the overall luminescent quantum yields and observable lifetimes to be calculated for different europium complexes. The specific aims are to help develop ligands that have high radiative rates. Experimental measurements obtained from SC-CEAS can also be used to confirm or refine existing transition theory, such as Judd-Ofelt model [Judd, 1962; Ofelt, 1962].

Europium and other lanthanides have been used in a number of industries over the past few decades but are also predicted to have a role in future advancements. For example, the lighting industry has seen organic LEDs using lanthanides replace lamp phosphors [Kido and Okamoto, 2002]. There are also completely new exciting areas of growth such as biological assay development [Yam and Lo, 1999] and medical imaging [Faulkner et al., 2005]. As a result, research into lanthanide complexes is likely to expand as increasing demands are placed on their photophysical capabilities and tools such as SC-CEAS have the potential to be of increasing benefit.

6.3 Near-UV supercontinuum for Amyloid detection

Introduction: Aims and Objectives

There are a number of biological substances and small compounds, for instance many organic compounds, that have absorption peaks in the blue and near-UV spectral range. These currently cannot be detected with SC-CEAS presented in Chapter 4 or current methods presented in the literature. Current commercial SC sources do not extend below 390 nm and as a result a recent focus for PCF fabricators and SC source designers has been to push the blue edge further into the UV [Stark et al., 2011] to enable further applications in spectroscopy and imaging to be made. Novel custom-drawn PCFs have been used to demonstrate SC extending down to 350 nm and lower either by tailoring the cross-sectional fibre dimensions [Udem et al., 2002] or through producing "tapered" PCF, with a dimensions varying along the axial fibre length [Stone and Knight, 2012].

The motivation here is to use novel dispersion-engineered tapered fibres to generate near-UV supercontinuum to be used in SC-CEAS. The target analyte is hen egg white lysozyme (HEWL) which is an amyloidogenic protein. The study of HEWL aggregation is important for research into neurodegenerative diseases such as Alzheimer's and Parkinson's disease and, at present, quantitative results are difficult to obtain for early-stage aggregation.

6.3.1 Background: Tapered photonic crystal fibres

The dispersive properties of photonic crystal fibres were first adjusted by altering the cross-sectional dimensions of a uniform fibre, as discussed in Section 2.2. It was then shown that tapering PCF along the axial length of the fibre could produce supercontinua that could not be generated in uniform fibres [Kudlinski et al., 2006; Stone and Knight, 2012]. Tapered fibre research has had particular focus on extending the blue-edge of SC light into the UV [Travers, 2010].

Stone and Knight [2012] stated that the introduction of a taper does not alter the underlying physics involved in SC generation, i.e. those discussed in Chapter 2. Instead, tapering enables the zero-dispersion wavelength (ZDW) to be shifted

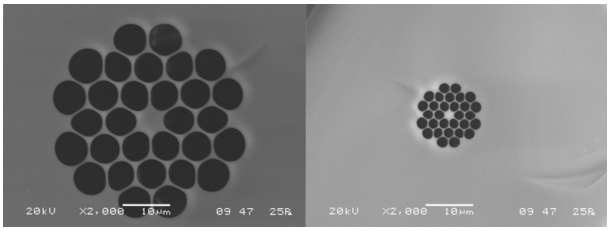

Figure 6.9: *Scanning electron micrographs of tapered PCF in cross-section. Fibre input with* 6 µm *core (left) and fibre output with* 2 µm *core (right). Figure reproduced courtesy of Stone and Knight [2012].*

along the axial length of the fibre, whereas it is fixed throughout a uniform fibre. This allows different nonlinearity to be amplified at different points along the fibre. The custom-designed PCF described in Stone and Knight [2012] was used in this work, courtesy of Dr Jim Stone of Centre for Photonics & Photonic Materials (CPPM), University of Bath. The 6 µm fibre core is tapered down to 2 µm over a fibre length of 5 m. Scanning electron micrographs of the fibre ends are shown in Figure 6.9.

A detailed discussion of the effects of tapering is given by Travers [2010]. A key finding of Stone and Knight [2012] is that the SC generated at the 6 µm input end of the fibre is broad enough to extend to the blue-shifted ZDW near the 2 µm tapered end of the fibre. This light also has enough spectral intensity to seed SC generation of light that extends down to 330 nm at the fibre output (see Figure 6.10), giving the spectrum its symmetrical appearance. The output of the taper used in this work was recorded by the author at CPPM, University of Bath, using a pump laser (FemtoPower1060-20-PP, Fianium, UK) very similar to that used for SC-CEAS measurements in Chapter 4, but with a lower average power of ∼350 mW.

6.3.2 Neurodegenerative diseases and Amyloid aggregation

Alzheimer's Disease (AD) is a neurodegenerative disease that affects 35.6 million people worldwide, with this number expected to double by 2030 [World Health Organistion, 2012]. The annual cost of treatment was estimated as US$604 bil-

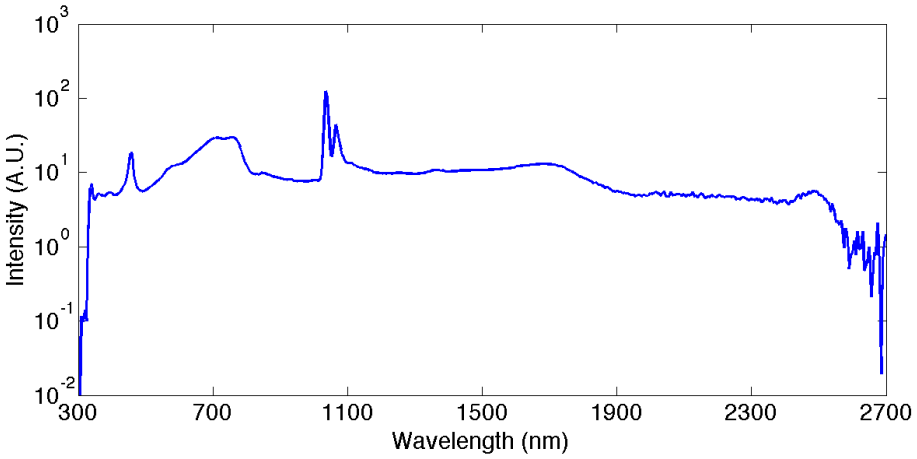

Figure 6.10: *Spectral output of* 5 m *tapered PCF covering* ∼330 nm *to* 2700 nm. *The core size was* 6 µm *and* 2 µm *at the input and output respectively. The fibre was pumped using a ytterbium-doped fibre laser (FemtoPower1060-20-PP, Fianium, UK) emitting* 5 ps *pulses at* 1060 nm *wavelength and* 1 MHz *repetition rate.*

lion in 2010. In the UK, the figure for the current annual cost of treatment is expected to rise to £23 billion [Alzheimer's Society, 2009]. AD is the most common cause of dementia. Dementia is not actually a disease, rather a description of the symptoms that develop when neurons in the brain die or stop functioning correctly. Such symptoms are memory loss and loss of other cognitive functions, which ultimately lead to death. It mainly effects those over 65 which is why it is a growing issue for countries with ageing populations.

The causes of AD are currently attributed to protein misfolding; very little is known about the actual pathology [Gidalevitz et al., 2011]. Proteins within a living organisms have a target conformation into which they must form, with their structures defining their functionality. It is this aggregation that can inhibit regular cellular function within a cell [Gidalevitz et al., 2011]. Misfolded proteins can go on to form fibrillar-structured so-called protein amyloids. It is believed that the formulation of these species, either as extracellular deposits or intracellular inclusions with amyloidogenic characteristics are responsible for the onset of AD [Chiti and Dobson, 2006]. Further details and biological aspects of protein folding are discussed in Anfinsen [1972, 1973], with discussion here limited to the

case where proteins are misfolded leading to aggregation.

In addition to AD, there are other diseases linked to protein amyloid formation, such as Parkinson's Disease (PD) and type II diabetes [Westermark et al., 1990]. There is an urgent need to study amyloid formation in order to find out how better to treat and prevent such diseases occurring. The World Health Organistion [2012] called research into AD a public health priority, along with U.S. Department of Health and Human Services [2012] and Department of Health [2012] in the UK, with both governments announcing significant increases to research funding. Unfortunately, current research has been limited by the absence of suitable non-invasive experimental techniques capable of monitoring the process of amyloid formation *in vitro* [Alzheimers Association, 2013]. The ultimate aim would be to study *in vivo*, i.e. in live cells of organisms, but this is still much further away in the future. The aim here is to utilise the high sensitivity of SC-CEAS to make *in vitro* measurements of amyloids and obtain quantitative data.

Techniques for Monitoring Protein Aggregation

A number of different experimental techniques have been used to study amyloid aggregation [Harper and Lansbury, 1997]. Dynamic light scattering and circular dichroism (CD) have been used to determine aggregation kinetics through particle size distribution [Bitan et al., 2003; Lomakin et al., 1996; Uversky et al., 2002]. Other studies have used techniques such as atomic force microscopy (AFM) and transmission electron microscopy in order to take time-lapsed images of amyloids both before and during fibril formation [Goldsbury et al., 1999; Huang et al., 2000; Mastrangelo et al., 2006]. Amyloid fibril structure has also been studied in 3D using nuclear magnetic resonance spectroscopy (NMR). This is necessary to observe structural changes on a molecular level and, most importantly, provide information for the design of aggregation inhibitors [Lührs et al., 2005].

In terms of optical methods, Fourier transform infrared spectroscopy (FTIR) has been employed to infer structural behaviour during fibril formation through analysis of spectral changes [Bouchard et al., 2000; Zandomeneghi et al., 2004]. FTIR does not have the resolving power of X-ray crystallography or NMR, but is

used for its fast measurement times and broader applicability for studying aggregates with natural isotope distributions. Fluorescence techniques are also widely employed, with congo red and thioflavin T (ThT) identified as two dyes that bind specifically to amyloids [Klunk et al., 1989; Naiki et al., 1989]. Fluorescent dyes or stains are popular because they are sensitive and convenient to use, but there are problems concerning their use. First, the magnitude of fluorescence was shown to vary with fibrillar morphology. Secondly, ThT was found to be most suitable for detecting mature fibrils. Results from AFM and TEM images have shown that a number of oligomers form well before they can be detected with these methods [Huang et al., 2000; Mastrangelo et al., 2006].

Research is now focussing on this early stage aggregation, as studies have shown that this stage of oligomer formation causes greater cytotoxity [Caughey and Lansbury, 2003; Haass and Selkoe, 2007; Kirkitadze et al., 2002]. Further work is needed in order to confirm the findings of these studies and also to find the cause of toxicity, as this remains unknown [Petkova et al., 2005]. New fluorescent tags designed specifically for early stage oligomers, for instance, are being developed [Lindgren and Hammarström, 2010; Yushchenko et al., 2010]. Amyloid research would benefit if a sensitive technique capable of label-free detection was available too. This particular area is where SC-CEAS could be applicable with results of experiments described in this thesis demonstrating its potential.

6.3.3 Methodology: Extending into the blue and near-UV

Fibre Coupling

As previously discussed in Section 2.2 efficient coupling laser light into PCF requires matching of the light beam to the mode size (i.e. core) and ensuring that the numerical aperture (NA) of the fibre is larger than the NA of the focused beam. The fibre laser (FemtoPower 1060, Fianium, UK), emits a Gaussian beam of diameter 1.1 mm. A lens of focal length, f, can be used to focus a Gaussian beam of waist, D_i down to spot size, D_0:

$$D_0 = \left(\frac{4\lambda}{\pi}\right)\left(\frac{f}{D_i}\right), \tag{6.13}$$

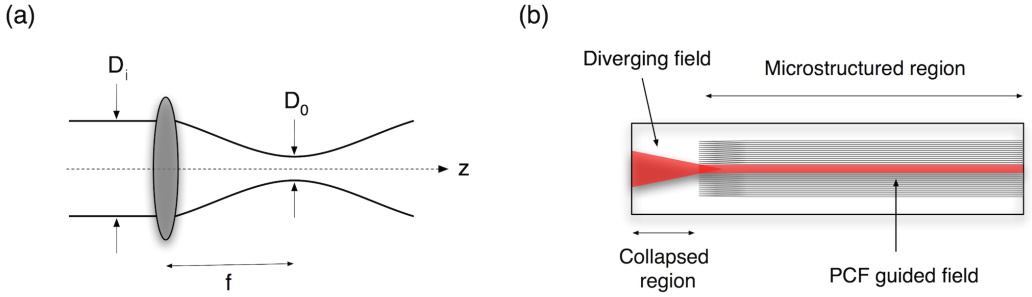

Figure 6.11: *Schematic of focused beam dimensions and PCF regions for effective light coupling. (a) Lens effects on a Gaussian beam and resultant beam dimensions. (b) Axial cross-section of a PCF showing the collapsed and microstructured regions.*

where λ is the wavelength of the laser (see Figure 6.11). In this case, the 1060 nm fibre laser would require a lens of 6.2 mm focal length to match the ∼6 µm core of the tapered fibre. Microscope objectives are commonly used for fibre coupling. Here, an aspheric lens of $f = 6.2$ mm (5723-H-C, Newport Corporation, USA) was used in this set-up. Aspheric lenses have higher transmission than a microscope objective with the same magnification. The NA can be calculated using the equation $\mathrm{NA}_{\mathrm{lens}} = n \sin\left(\arctan\frac{D}{2f}\right)$. The calculated value in this particular case, $\mathrm{NA}_{\mathrm{lens}} = 0.13$, is less than the NA of the fibre, $\mathrm{NA}_{\mathrm{PCF}} = 0.20$.

The bare fibre must be cleaved in order to ensure clean fibre faces at both ends. PCF come with a standard acrylate coating which must first be removed before cleaving. Standard mechanical stripping tools are available, but these may not be effective for fibres with non-standard diameters. In such cases, stripping must be done by hand using a bare razor blade carefully to remove the coating, especially at the thin end of the taper. This was the approach used for the tapered fibre here. Fibre cleaving can be done with diamond scribers or high precision cleavers. In this work, a ceramic tile was used to cut the PCF by hand with a stereo microscope (SZX10, Olympus, Japan) used to check the quality of each cleave. Again, a manual method was more effective for this non-standard fibre.

A set-up for fibre coupling is shown in Figure 6.12. A collimation lens is needed for lasers that do not have collimated outputs. Beam attenuators may also be required for lasers without in-built power control. The two steering mirrors are used to ensure the laser beam travels directly along the axis of the focussing lens

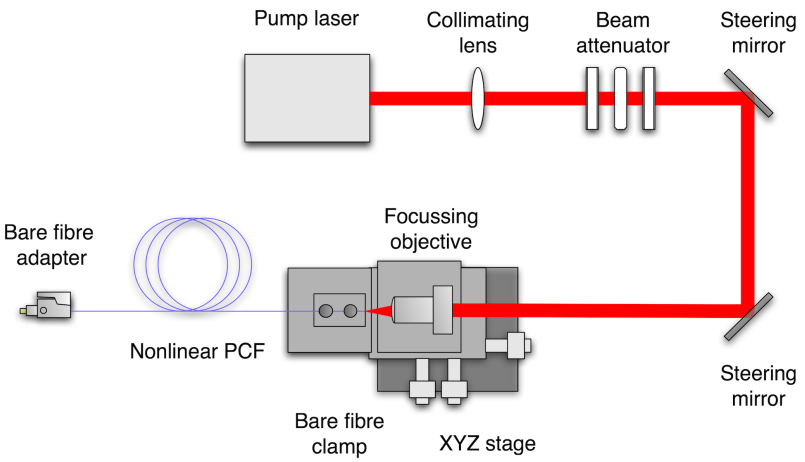

Figure 6.12: *Fibre launching set-up for UV-SC generation. The beam attenuator consists of a polariser, half-waveplate and analyser.*

and into the fibre. It may be necessary to employ a telescope if the collimated beam requires an expansion or reduction in beam waist in order to correctly fill the focussing lens. The bare fibre input end of the tapered fibre is placed on a high-precision 3-axis stage with differential micrometer adjusters (MAX303, Thorlabs, USA) with the focusing lens mounted on its adjustment platform. The output end of the PCF is fitted with an FC-PC connector (Bullet Bare Fiber Adapter, Fiber Plus International, USA) to enable easy integration into the existing SC-CEAS set-up.

Special care must be taken when coupling light from the pump laser into the PCF, in order to avoid fibre damage. Optical damage can be detected by a sudden drop in output power and beam quality. Fibre ends are more fragile and are not covered by the protective coating. Consequently, they are more prone to damage and susceptible to dust and dirt [Smith and Do, 2008]. The main risk comes from coupling itself and the challenge of coupling a high energy input beam into tiny cores. High pulse energies can cause melting or fracturing of the fibre [Smith et al., 2009]. The manufacturer specified damage threshold of a standard commercial PCF (SC-5.0-1040, NKT Photonics, Denmark) is 15 µJ, although this should be viewed as an upper limit and thus users are instructed always to operate below such a value. If necessary, the damage threshold can be increased by increasing the mode field diameter of the PCF input. This can be

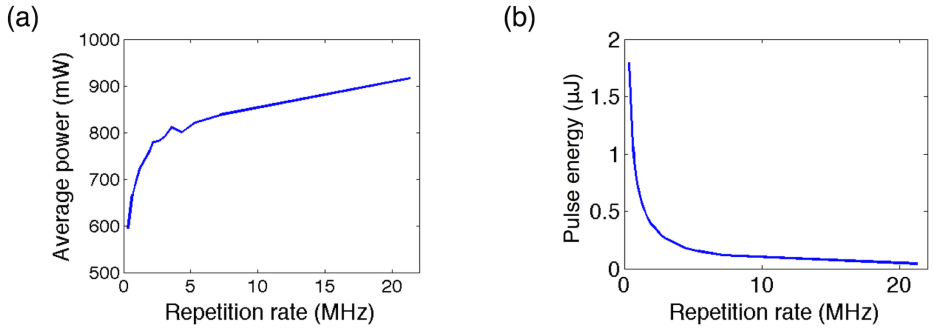

Figure 6.13: *Pump laser characteristics for the fibre laser used as the pump source for SC generation (Fianium FemtoPower 1060). (a) Average power vs. repetition rate. (b) Pulse energy vs. repetition rate of laser.*

achieved by collapsing the microstructured air-holes in the cladding. This creates a diverging field larger than the actual core size at the PCF input face. The energy from the coupled laser beam is then spread over a larger area.

Pump Laser Characteristics for UV-SC Generation

The characteristics of a pump laser which was used for SC generation (FemtoPower 1060, Fianium, UK) are shown in Figure 6.13. The laser is a passively mode-locked ytterbium fibre laser and the repetition rate is adjustable in the range 330 kHz to 21 MHz by means of an in-built acousto-optic pulse picker. Figure 6.13(a) shows the measured variation in average output power with repetition rate. The power increases rapidly up to about 7 MHz and then more gradually until a maximum output of around 900 mW. Figure 6.13(b) shows a plot of pulse energy against repetition rate. As mentioned in Chapter 2, higher pulse energies powers are desirable for generation of broader SC. Therefore, any repetition rate below 1.35 MHz would be suitable to generate a pulse energy greater than 0.5 µJ. Given the above, repetition rates in the range 0.33 MHz to 1.08 MHz were used.

UV-SC-CEAS Set-up Modifications

SC-CEAS was initially designed and optimised for measurements in the visible spectrum. The successful generation of UV-supercontinuum provided a number

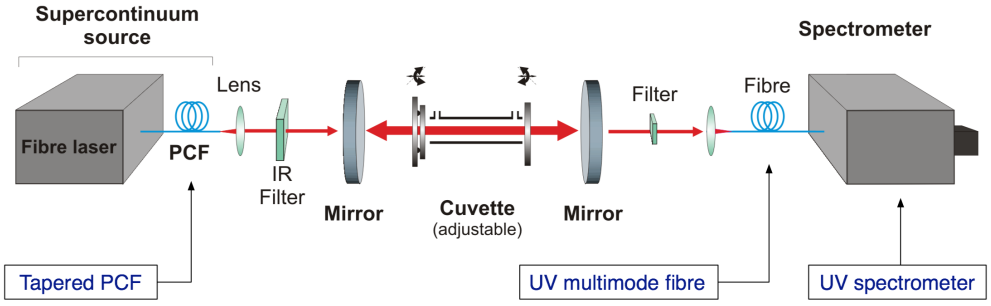

Figure 6.14: *Modified SC-CEAS set-up for near-UV and visible absorption. Modifications include the use of UV-enhanced optics, fibres and fibre optic spectrometer.*

of opportunities, yet at the same time introduced a few challenges with regard to the equipment and optical components used. The key component alterations from the set-up used for previous measurements (as shown in Section 4.3) are highlighted in Figure 6.14. The main challenge was on the detection side. The quantum efficiency of the EM-CCD previously used dropped half its peak value at 400 nm and continued to drop significantly below this. This type of spectral response is common for most current CCD chips currently on the market, which is why a UV-enhanced spectrometer was used instead (USB2000, Ocean Optics, USA). This compact spectrometer is less sensitive, but it has a wavelength range (where the quoted efficiency >30%) from 200 nm to 850 nm. Light from the cavity was coupled into a UV-vis multimode fibre (180 nm to 1150 nm FC patchcord, Edmund Optics, USA) and then connected straight to the FC port of the spectrometer. The cavity mirrors used were custom-designed with 99.0% nominal reflectivity in the range 300 nm to 600 nm (1.0 m radius of curvature; Layertec GmbH, Germany), with appropriate filters used to cut out SC light outside of this range. UV-enhanced optics were used where available, although the issue of glass degradation caused by UV light was not observed to be a problem.

Hen Egg White Lysozyme (HEWL) as a Model for Protein Aggregation

Hen egg white lysozyme (HEWL) is used as a model for amyloid aggregation. HEWL aggregation has been studied by Guptasarma [2008] with fluorescence emission shown to increase with aggregation time. HEWL is commonly used

as it is available in large quantities at low cost, but also due to the fact that aggregation time is slow enough to observe changes. Chan et al. [2013] measured spectral changes in fluorescence measurements after 0, 2, 4, 6 and 11 days of aggregation which was achieved through incubation at 60 °C and pH 2.2. Their results were in agreement with fluorescence measurements made by Guptasarma [2008]. Complete aggregation of HEWL under these conditions was found to require 10 days of incubation and the first insoluble amyloid fibrils were found to form after ∼36 hours of aggregation.

6.3.4 Results and discussion

The focus of the results presented here was on studying very early stage aggregation, to take advantage of the high sensitivity of SC-CEAS. The oligomers being formed which are responsible for the absorption, may contain only 10 to 100 molecules [Chiti and Dobson, 2006]. Therefore, high sensitivity is required to detect these very small changes in absorption on a scale of hours rather than days. Hen egg white lysozyme (L-6876, Sigma-Aldrich, UK) was dissolved in glycine-HCl buffer, pH 2.2, and then filtered using 0.2 µm microfilters (Millipore, USA). The samples of initial monomer concentration of 1 mM were incubated at 60 °C for a maximum of 24 hours. The samples were diluted before measurement to a concentration of 250 µM. All of the measured samples were prepared and supplied by Fiona Chan (further information can be found in [Chan et al., 2013]). Figure 6.15 shows the resultant spectra of samples that had been aggregated for 0, 4, 15 and 24 hours. Samples were first flash frozen in liquid nitrogen after incubation to prevent further aggregation after the designated incubation time. Measurements were carried out at room temperature and sample volumes were 1.0 mL. The results show a distinct peak form at 387 nm after 4 hours of aggregation in addition to the appearance of a shoulder from 440 nm to 550 nm. Absorption clearly increases with total aggregation time. The main peak could not have been detected by commercial supercontinuum sources which are currently limited to a minimum wavelength of 390 nm. Nor, to the best of the author's knowledge, have any broadband cavity-enhanced techniques demonstrated spectral measurements spanning over 200 nm with a minimum wavelength of 330 nm. The spectral data

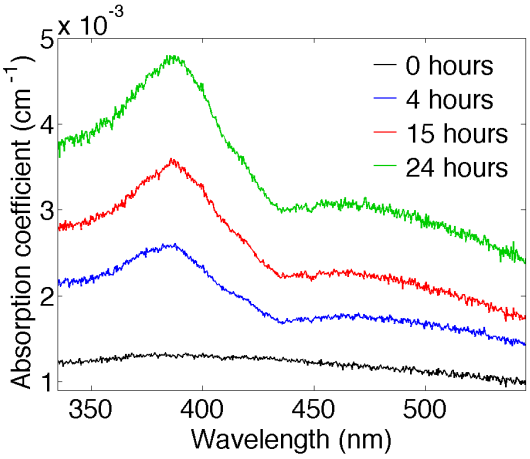

Figure 6.15: *Near-UV spectra of* 250 µM *hen egg white lysozyme after 0, 4, 15 and 24 hours of aggregation.*

are in agreement with the fluorescence measurements made by Chan et al. [2013] with the same trend and position of the spectral maximum. These SC-CEAS measurements have the additional advantage in that they are quantitative. For example, the peak absorption of the sample aggregated for 24 hours at 387 nm has an absorption coefficient of $4.8 \times 10^{-3}\,\mathrm{cm}^{-1}$. This equates to a molar absorption coefficient of $19.2\,\mathrm{M}^{-1}\,\mathrm{cm}^{-1}$ for a monomeric concentration of 250 µM.

Summary and Future Work

The development of UV-SC-CEAS has opened up many possibilities for the study of liquid species. Amyloid aggregation is one such example of how the technique can be used to answer important scientific questions. The sensitivity also opens up the possibilities of further label-free studies of proteins and other biological species to provide more detailed information on the molecular level. Future experimental improvements should focus on the sensitivity of the UV detection system and also the development of UV optics of higher efficiencies. The full extent of UV-SC expansion into the blue has yet to be determined, but this initial demonstration of and increase of 60 nm into the near-UV represents a significant spectral advancement in high-sensitivity liquid-phase spectroscopy. The measurements made here are the first absorption measurements taken in this spectral region for the analysis for these types of protein.

6.4 Blood sensing - initial demonstration

Introduction: Aims and Objectives

The development of BB-CRDS liquid-phase spectrometer was outlined in Chapter 5. The inherently self-calibrating nature and substantial increase in sensitivity over single-pass absorption techniques makes BB-CRDS attractive for a number of liquid-phase applications. In contrast to the EM-CCD detectors used for SC-CEAS, it is far more compact and even at this prototype stage it represents a more financially attractive proposition. Although results presented here have shown SC-CEAS to be more sensitive, the difference between the techniques were less than an order of magnitude. For some applications, BB-CRDS may have sufficient sensitivity, as a result of which its other attributes become significant advantages. One such example, is the analysis of blood at low concentration. A BB-CRDS spectrometer could potentially be developed into a spectrometer capable of recording spectral differences in trace levels of blood before and after haemolysis. The aim of the work here is to demonstrate this and further highlight the applicability of the novel single photon avalanche photodiode (SPAD) array, as introduced in Chapter 5.

Analysis of Red Blood Cells

Blood is a physiologically important medium responsible for the transportation of nutrients and molecules around the body to the vital organs. Blood also has a secondary, yet equally important role in the removal of waste products. Analysis of blood is important not only for medical diagnosis but also for biological research into pathological disease mechanisms. However, it is a complex medium that can both absorb and scatter EM radiation such as light. At times it may be necessary to investigate samples of blood with a low red blood cell content, i.e. low concentration. Furthermore, it may be necessary to detect both lysed and whole blood whereas a number of current traditional analytical techniques require haemolysis.

6.4.1 Spectroscopic analysis of blood

Blood contains many important physiological components, but its spectroscopic properties are dominated by haemoglobin (Hb). Absorption spectra of blood vary according to the oxygenation state of the heme group in Hb [Horecker, 1943; Rother et al., 2005]. Co-oximetry [Vreman et al., 1988; Zijlstra et al., 1991] and photometry [Neville, 1987; Rippmann et al., 1997] are the routine methods for Hb analysis in blood and are popular due to their portability, small sample volume, relatively low cost, and simplicity. However, their limited sensitivity only allows Hb tetramer concentrations from 50 g/L to 150 g/L to be detected. Furthermore, their application requires haemolysis of blood cells prior to measurement and their spectral resolution is limited. The development of a more sensitive method for quantifying blood concentration with the ability to monitor variations in composition by measuring changes in absorption spectra at trace levels would constitute a significant advance in biomedical diagnostic capabilities.

Haemolysis of Red Blood Cells

The haemolysis of red blood cells can be a result of a number of different physiological abnormalities within the human body, as shown in Figure 6.16, taken from Rother et al. [2005]. The first step is usually dimerisation followed by oxidation into methaemoglobin and then ferric haemoglobin. An alternative involves the formation of haptoglobin-haemoglobin complexes in an irreversible process. This complex is then removed from the plasma through endocytosis by macrophages or monocytes (cells that protect the body by ingestion of unwanted particles or cells) [Kristiansen et al., 2001; Nagel and Gibson, 1971]. The common result of chronic or acute haemolysis is an increase of cell-free haemoglobin and heme in the blood plasma. One further consequence of this is an increase in nitric oxide scavenging by plasma haemoglobin [Olson et al., 2004]. This can have serious effects for smooth muscle regulation, potentially leading to vasoconstriction, intravascular thrombosis and neurological movement disorders. More details can be found in Rother et al. [2005] and references therein.

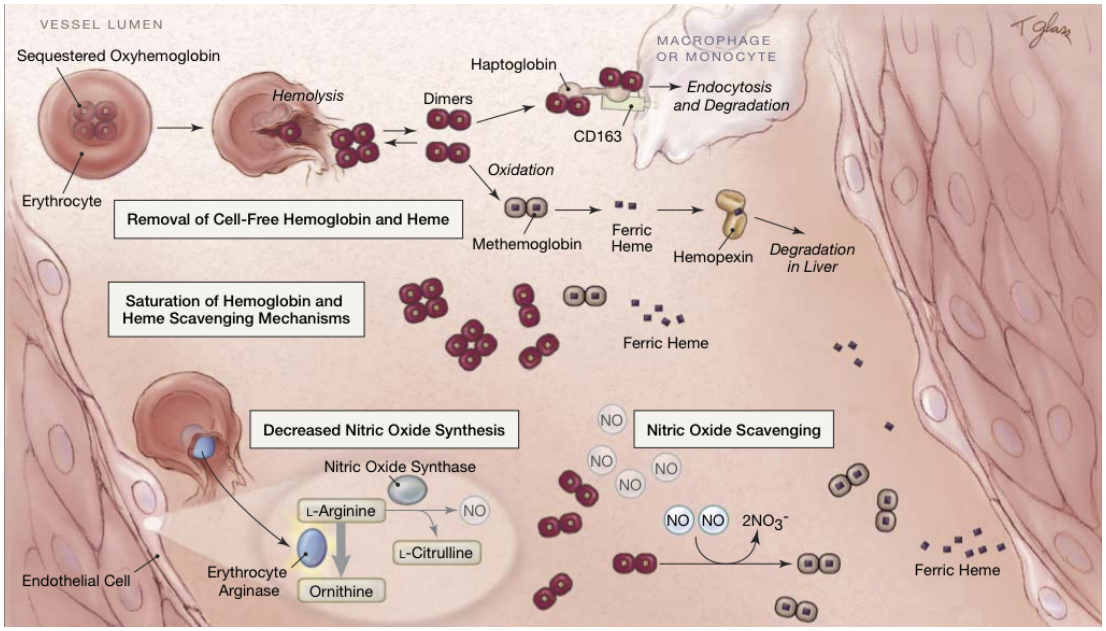

Figure 6.16: *Pathobiological effects of cell-free plasma haemoglobin during intravascular haemolysis. Figure reproduced from Rother et al. [2005].*

6.4.2 Methodology: Sample details

The blood samples were obtained from healthy volunteers by venipuncture into a syringe with heparin after informed, written consent. Whole blood was diluted with 50% RPMI-1640 buffer solution. Haemolysis was achieved osmotically with samples diluted in ultrapure water ($18\,\mathrm{M\Omega\,cm^{-1}}$, Milli-Q, Millipore, USA) from 50% haematocrit. In complex media such as blood, scattering from suspended particulates can present a problem and filtering to remove large particulate matter prior to conducting an absorption experiment may be beneficial. For the high dilution ratios used in the present experiments, such effects are negligible, as was previously shown in Horecker [1943]. The predicted amount of Rayleigh scattering from a sample of this concentration is modelled in Chapter 4 (c.f. Figure 4.3) and shown to be lower than the expected solvent absorption contribution, which becomes the limiting variable in terms of the sample itself.

6.4.3 Results and discussion

Figure 6.17(a) shows spectra of both whole blood (at 2.7×10^{-2} g/L tetramer concentration, corresponding to 5.0×10^4 RBC/mL concentration) and lysed blood (at 1.35×10^{-2} g/L tetramer or 1.0×10^5 RBC/mL concentration) acquired using the BB-CRDS technique (N.B. 100% packing = 1.0×10^{10} RBC/mL). The technique presented here can be used to detect spectral differences in absorption features. Spectra shown in Figure 6.17 were integrated over 2 s ($\sim 2 \times 10^6$ pulses). Detection limits of 1.5×10^4 RBC/mL for whole blood and 5.8×10^4 RBC/mL for lysed blood, respectively, were obtained. The sample volume was 1.0 mL for both cases. Note that even higher sensitivity could be achieved by shifting the excitation wavelength to 415 nm, which lies in the Soret excitation band of haemoglobin and features an approximately 10-fold increase in the absorption cross section. In the present set-up this potential improvement could not be realised because of power limitation in the available light source. A spectrum of lower resolution but featuring broader wavelength coverage of 130 nm across the pixel array is also shown (see Figure 6.17(b)). It corresponds to lysed blood at 1.0×10^5 RBC/mL concentration and was obtained during 2 s of integration.

Summary and Future Work

Chapter 5 introduced BB-CRDS in the liquid phase as a calibration method. In this chapter, the technique has been used in the measurement of liquid analytes at low concentration. As shown in this work, its use in the sensitive detection of blood has highlighted its potential in medical analysis. The method offers good sensitivity with high spectral resolution and is self-referencing, obviating the need for extensive calibration protocols. The technique could be developed into a flexible and cost-effective sensor technology due to the scalability of CMOS production techniques. There are many potential applications ranging from blood-based medical assays to applications in the basic sciences and process industries.

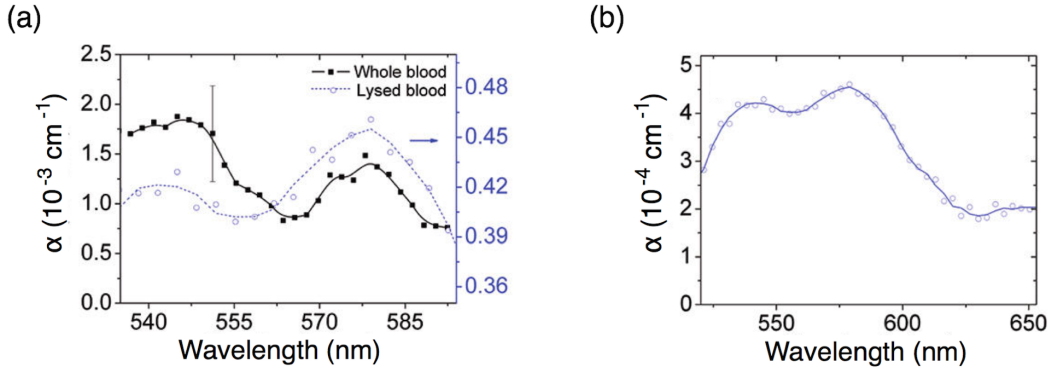

Figure 6.17: *(a) BB-CRDS spectra of whole blood at* 5.0×10^4 RBC/mL *concentration and lysed blood at* 1.0×10^5 RBC/mL *concentration. Data are an average of 20 spectra acquired at* 0.1 s *per spectrum giving a total* 2 s *acquisition time. The error bar included represents the uncertainty* (1σ) *associated with the linear fit to the four data points of each spectral channel and is representative for all other data points shown. (b) Spectrum of lysed blood at* 1.0×10^5 RBC/mL *concentration spanning* 130 nm. *Data are fitted with a 5-point Savitzky-Golay convolution for visualisation (solid and dashed lines). Spectral data were acquired at a resolution of* 2.0 nm *nm per pixel for whole blood and* 3.3 nm *per pixel for lysed blood.*

6.5 Conclusions

The cavity-enhanced techniques developed in this work were designed to address the current scientific need for a quantitive method for the measurement of liquid samples at low concentration. Previous chapters focus on the technical aspects and scientific background of the technique, with measurements demonstrating the features and capabilities thereof. The results presented in this chapter show the implementations of both SC-CEAS (introduced in Chapter 4) and BB-CRDS (introduced in Chapter 5). There are some significant findings that either open up potential new areas of research or provide new information in the study of existing problems. The highlights from this chapter are summarised below:

(i) Demonstration of a sensitive method for reaction monitoring across 220 nm of the visible spectrum with millisecond single-shot acquisition times using SC-CEAS. The oscillating Belousov-Zhabotinsky reaction was monitored here.

(ii) Detection of electronic transitions of trace lanthanide complexes in solution enabling more detailed analysis of the photophysics. These lanthanide complexes are important to the design of many high-tech devices.

(iii) Label-free *in vitro* measurement of protein aggregation as a model for early stage peptide dynamics. This research is involved in dementia research, in particular the study of Alzheimer's Disease.

(iv) Implementation of BB-CRDS based on a SPAD array as a self-calibrating, compact sensor. This demonstration, as a first, involved the analysis of blood samples with different oxygenation states.

(v) First implementation of near-UV CEAS for broadband analysis of analytically important species over 200 nm and down to 330 nm in the UV. To the best of the author's knowledge, this extends the current lower wavelength limit of published results by 60 nm from the visible into the UV.

All measurements were made at low concentration and the use of supercontinuum radiation (see Chapter 4) is key to the performance of the technique based on the implementation of optical cavities (see Chapter 3).

Chapter 7

Conclusions

7.1 Thesis overview

There are three main contributions that are likely to have an impact on future scientific research and engineering practice. The first is the exploitation of cavity-enhanced techniques in liquid-phase analytics for sensitivity enhancements. Both SC-CEAS and BB-CRDS techniques were designed and successfully implemented for high sensitivity concentration measurements. The latter technique overcame the technological challenge of measuring ring-down times as short as tens of nano-seconds, which is a requirement for BB-CRDS of liquids. The second contribution is the demonstration of a broad range of applications, from biomedical with blood and amyloidogenic proteins, to chemical monitoring of an oscillating reaction and trace detection of an industrially important metal. The third is the introduction of supercontinuum radiation and discussion of the benefits it may offer liquid-phase absorption measurements. Furthermore, the application of novel PCF to extend greatly SC measurements into the near-UV. These accomplishments are discussed in greater detail below.

Implementation of Liquid SC-CEAS

In this work, a broadband spectrometer using a supercontinuum source and cavity enhanced absorption spectroscopy has been developed and applied to liquid-phase measurements. Detection sensitivities at picomolar levels were obtained in the

visible range for absorbers with signal integration times in the lower millisecond range. Liquid samples can easily and quickly be exchanged during measurements for fast, convenient analysis of multiple samples or coupling to complex fluid handling systems. The set-up is straight-forward and allows for high sensitivity, rapid acquisition of broad bandwidth spectra, from which components in mixtures can be identified.

The liquid-phase SC-CEAS developed in this work detects spectral features of analytes dissolved in liquids at resolutions down to 1.1 nm with millisecond measurement times. A 50-fold increase in sample pathlength leads to a minimum detectable absorption coefficient of $9.1 \times 10^{-7}\,\mathrm{cm}^{-1}\,\mathrm{Hz}^{-1/2}$ at 550 nm can be obtained for a measurement bandwidth of 250 nm. This result compares to the most sensitive detection limits obtained using monochromatic sources that are reported in literature. The applications demonstrated, e.g. oscillating reaction monitoring (Belousov-Zhabhotinsky reaction) and the detection of trace levels of industrially important metals (lanthanide complexes), have highlighted the unique combination of sensitivity, speed and bandwidth offered by this technique. This opens up potential applications in a range of different industries and areas of scientific research.

Development of Liquid BB-CRDS

Previous liquid-phase cavity-enhanced techniques had not fully addressed the issue of calibration for broad spectral bandwidth measurements. The implementation of SPAD array technology has enabled the experimental challenge of measuring multiple ring-down events at nanosecond time resolution to be overcome. Calibration is an important issue, especially in the case of cavity-enhanced techniques involving the use of potentially lossy interfaces, i.e. a cuvette. BB-CRDS allows for the quantification of all "losses" and evaluation of the optical properties and components shows that high precision alignment maintains light within the cavity and thus these so-called losses are negligible.

To the author's knowledge, this is the first implementation of this novel CMOS technology for liquid absorption spectroscopy, introducing an effective alternative in detector technology which has predominantly been reliant on CCD develop-

ment. These CMOS-based SPAD arrays are solid-state photodetectors capable of detecting low light intensity, down to just a single-photon.

Extension of SC-CEAS into the Near-UV

The successful implementation of UV-SC (see Section 6.3.1) for SC-CEAS presents a breakthrough in terms of the spectral range of truly broadband (>100 nm) CEAS in liquids. Tapered PCF have been used to generate UV-SC that extended down to 330 nm in the near-UV, representing an extension of 60 nm over what has been demonstrated in other published broadband CEAS results. These tapered fibres designed and fabricated by collaborators at the University of Bath allow the same benefits of sensitivity, speed and bandwidth offered by SC-CEAS to be extended into the near-UV. This opens up the potential of the technique to a number of new applications requiring quantitative analysis. This may range from the study of small organic compounds to biological samples like the amyloids presented here.

7.2 Proposed future developments

The field of liquid sensing and the use of supercontinuum radiation has been discussed in this thesis. Advancements have been made within the scope of this research, however, a number of potential future opportunities exist, some of which are discussed below.

Pump Laser Source Development

The two previous advancements centred on PCF design and fabrication. Pump laser development would further enhance the development of SC sources for sensing. One such example is the further investigation of SC generation using microchip laser sources [Zayhowski, 1999]. Stone and Knight [2008] generated an SC spectrum spanning from 400 nm to 2450 nm by using 10 m PCF and a 600 ps (pulse width) microchip laser pumping pulses at 1064 nm. Kudlinski et al. [2010] recently demonstrated the use of a microchip laser and a a high-Δ tapered PCF to

generate blue-optimised light, i.e. where 30% of the total average output energy was in the band 350 nm to 600 nm. These advancements, having built on earlier work [Leon-Saval et al., 2004; Xiong et al., 2006], demonstrate why microchip lasers are seen as the future of compact, efficient SC generation. Use of low cost microchip laser pump sources will also drive down the cost of SC systems.

High Stability (All-normal GVD) SC Generation

The SC radiation utilised in the techniques presented in this thesis was generated through nonlinear processes associated with anomalous group velocity dispersion (GVD) PCF. It is possible to achieve spectral broadening, admittedly not to the extremes shown here, using PCFs with all-normal GVD [Heidt et al., 2011]. Spectral broadening is achieved primarily through self-phase modulation and Raman scattering. The resultant radiation has greater temporal coherence, as noise-seeded solitonic processes are not involved. A smooth, flat spectrum spanning 800 nm has been demonstrated [Hooper et al., 2011]. This greatly addresses the stability issue of SC by reducing the pulse-to-pulse shot variation. One current limit of using such PCFs is that the short wavelength range reaches only around 650 nm. For the liquid applications here, it would be useful if the spectrum from all-normal PCF could be extended further into the visible, as solvent absorption is too strong in the near-IR.

CEAS for Solids and Thin Films

The work in this thesis focused on liquid analysis due to the lack of previous work done in the area and the vast number of future possibilities and applications that presented themselves. A similar statement could be made for thin films and solids. Thin samples are of interest in solid state physics and semi-conductor production. The ever growing demand for consumer electronics increases the need for advancements in component and semiconductor development. Novel methods, such as applying the film to the cavity mirror itself, have already been demonstrated [Kleine et al., 2001]. Single-channel CRDS has also been demonstrated in the near-IR [Aarts et al., 2004; Logunov, 2001; Smets et al., 2002] and visible

range [Muir and Alexander, 2003], but overall research remains limited.

The sensitivity of cavity-enhanced techniques is required due to the low absorbance of thin films. In fact, initial demonstrations to monitor film thickness spectrally were made by Engeln et al. [1999]; Pipino et al. [1997]. Analysis of solid samples was also carried out in this thesis on 5 mm thick optical samples in the visible spectral range, helping to characterise window losses during calibration (see Section 4.4.2). Use of BB-CRDS for thin films and solid samples should thus be feasible and offer up a new tool for analysis. Fast measurement timescales mean that such a system could be incorporated into manufacturing lines for on-line monitoring during fabrication. The cost of such a system would be relatively low when compared to techniques such as terahertz (THz) imaging. However, THz systems are currently unrivalled in terms of sensitivity and real-time analysis of semiconductor materials [Mittleman et al., 1996]. Furthermore, if pre-emptive detection is required earlier on in the manufacturing chain, then plasma sensing analysis may is more suitable [Yue et al., 2000].

Integration with Alternative Techniques

There are a number of innovative techniques outside the realm of line-of-sight sensing, that can still take advantage of cavity-enhancement. Two such examples are microfluidic devices (MFDs) and in-fibre sensing.

Microfluidic devices: The growth of lab-on-a-chip technologies has seen a rapid expansion in the application of microfluidic devices (MFDs) for surface plasmon resonance [Hassani and Skorobogatiy, 2006], electrochemistry [Trojanowicz, 2009], Raman spectroscopy [Cristobal et al., 2006; Leung et al., 2005], as well as classic fluorescence [Dittrich and Manz, 2005] and absorbance applications [Kuswandi et al., 2007; Nguyen and Wereley, 2002]. MFDs have enabled large complex processes to be scaled down dramatically from the bench scale to fractional volume amounts 10^{-9} L to 10^{-18} L [Whitesides, 2006]. MFDs permit high throughput of samples or reagents, whilst also enabling high selectivity and control through specifically designed channels [DeMello, 2006]. Consequently, there has been wide ranging interest from specialist scientific users interested in microanalysis [Mogensen et al., 2004], to those developing commercial point-of-care

devices for low-cost healthcare solutions [Myers and Lee, 2008].

There are a few issues with MFD in terms of sensitivity when related to liquid-phase sensing, predominantly due to the dramatically reduced pathlength. Neil et al. [2011] placed an MFD inside an optical cavity with the beam passing through a point in a microfluidic channel in a CEAS set-up. The quality of the MFD surface was not optimised in this first demonstration, and although the pathlength was improved over a single-pass measurement, the overall limit of detection was relatively modest ($\alpha_{\min} = 10^{-2}$). A recent review by Rushworth et al. [2012] shows alternative steps taken to couple light into the MFD channels and detect the transmitted light at the exit, in order to increase the pathlength, with some studies using intra-channel mirrors and even prisms to increase the sample pathlength. The lowest reported detection limit to date for all these multi-reflection schemes was 3.8×10^{-4} for an MFD with mirror-coated capillaries using an LED light source [Mishra and Dasgupta, 2007]. Opportunities thus exist to build on an MFD-CEAS scheme or the development of multi-reflection capillaries.

In-fibre sensing: The maximum achievable pathlengths in microfluidic devices are limited to the millimetre range [Rushworth et al., 2012]. Therefore, the sensitivity enhancement is bound to be limited, even with exotic multi-reflection capillary schemes. Consequently, alternative methods using larger-core capillary fibres ($\sim$200 µm to 400 µm) have been used to confine liquid sample [Waechter et al., 2011]. Small sample volumes (100 nL) were still obtainable by Waechter et al. [2011] using a capillary fibre of 9.25 m to perform a novel implementation of CRDS over multiple wavelengths through a multiplexing technique.

Photonic crystal fibres have been mentioned thus far in this thesis only as light waveguides. However, they have several advantages over capillary fibres in terms of in-fibre sensing, specifically hollow-core PCF (HC-PCF). First, they have very low waveguide losses and thus much longer fibre lengths can be used compared to straight glass capillaries of the same internal diameter [Chen et al., 2010]. Alternatively, a smaller internal diameter, and thus volume, can be used for the same equivalent length of glass capillary fibre. The second point is that they are almost completely insensitive to bend losses, which allows for more flexible and robust experimental set-up. Thirdly, light can propagate in a single mode with a constant transverse intensity profile. This latter point is very important when it

comes to the use of HC-PCF as nanoreactors for photochemical reactions [Chen et al., 2010; Cubillas et al., 2012; Williams et al., 2012]. The first application of PCF sensing envisage the used of evanescent wave field created in the cladding of soild-core sample PCF pumped with radiation from an SC source for sensing [Euser et al., 2008]. These recent advancements show the potential of PCFs for sensitive in-fibre detection of miniscule sample volumes.

Appendix A

Origins of the Soliton

The generalised nonlinear Schrödinger equation (GNLSE), as shown in Equation A-1, is routinely used to model the propagation of laser pulses in optical fibres [Agrawal, 2001].

$$-i\frac{\delta u}{\delta z} = \frac{1}{2}\frac{\delta^2 u}{\delta t^2} + |u|^2 u - i(\alpha/2)u, \tag{A-1}$$

where the pulse is represented here by $u = \mathrm{sech}(t)$. Changes to the pulse during propagation are simulated in steps. The rate of change of the pulse envelope is dependent on both dispersion and nonlinearity. Dispersion is represented by the first term on the right-hand side of the Equation A-1, with the second term representing nonlinearity and the final term representing fibre attenuation, where α is the linear loss constant. Fibre losses are taken to be negligible (i.e. $\alpha = 0$).

The following relationship enables the temporal phase change to be obtained from Equation A-1 [Mollenauer and Gordon, 2006], assuming $f(z,t)$ is real:
If

$$\frac{\delta u}{\delta z} = if(z,t)u,$$

then

$$\delta\phi(t) = f(0,t)dz. \tag{A-2}$$

Appendix A

Effect of Dispersion

In the absence on nonlinearity, Equation A-1 becomes:

$$\begin{aligned} \frac{\delta u}{\delta z} &= \frac{i}{2}\frac{\delta^2 u}{\delta t^2}, \\ \frac{\delta u}{\delta z} &= (\frac{i}{2u}\frac{\delta^2 u}{\delta t^2})u. \end{aligned} \tag{A-3}$$

Using Equation A-2, this becomes:

$$\delta\phi_{disp} = (\frac{1}{2u}\frac{\delta^2 u}{\delta t^2})dz. \tag{A-4}$$

Taking the second derivative of $u = \text{sech}(t)$:

$$\begin{aligned} u &= \text{sech}(t), \\ \frac{\delta u}{\delta t} &= -\text{sech}(t)\tanh(t), \\ \frac{\delta^2 u}{\delta t^2} &= \text{sech}(t)\tanh^2(t) - \text{sech}^3(t), \\ &= \text{sech}(t)[1 - \text{sech}^2(t)] - \text{sech}^3(t), \\ &= \text{sech}(t) - 2\text{sech}^3(t). \end{aligned} \tag{A-5}$$

Substituting Equation A-5 into Equation A-4 yields:

$$d\phi_{disp}(t) = \left[\frac{1}{2} - \text{sech}^2(t)\right] dz. \tag{A-6}$$

Effect of Nonlinearity

In the absence on dispersion, Equation A-1 becomes:

$$\frac{\delta u}{\delta z} = i|u|^2 u. \tag{A-7}$$

Using the substitution in Equation A-2, Equation A-7 becomes:

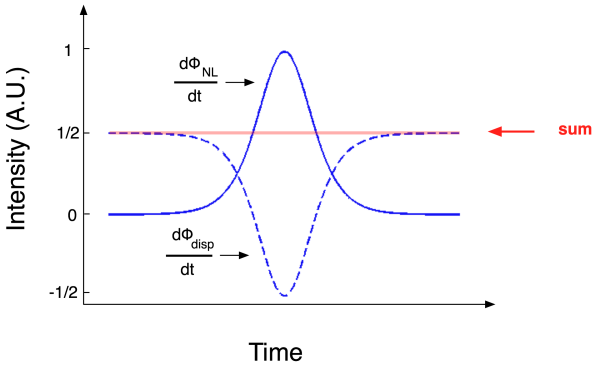

Figure A.1: *Theoretical origin of the soliton. The nonlinear ($d\phi_{NL}/dt$) and dispersive ($d\phi_{disp}/dt$) phase shift of a pulse in the anomalous dispersion regime and the resultant sum (red line).*

$$d\phi_{NL}(t) = |u(t)|^2 dt,$$
$$d\phi_{NL}(t) = |\mathrm{sech}^2(t)|dt \tag{A-8}$$

Soliton Generation

Figure A.1 shows Equations A-6 and A-8 plotted showing the combined effects of nonlinearity and dispersion in terms of phase shift. The two effects balance each other out, resulting in a pulse that maintains its shape in both the temporal and frequency domain during propagation. This is called a soliton.

Appendix B

Conference contributions

- T.K. Laurila, S.-S. Kiwanuka, J. Frank, and C.F. Kaminski, "Broadband cavity-enhanced spectroscopy using supercontinuum radiation," in Laser Applications to Chemical, Security and Environmental Analysis (LACSEA), **LT5B**. Optical Society of America. San Diego, USA. January 30, 2012.

- C.F. Kaminski, S.-S. Kiwanuka and T.K. Laurila, "Molecular sensing with supercontinuum radiation," in Conference on Lasers and Electro-Optics (CLEO). Optical Society of America, San Jose, USA. 1-6 May 2011.

- S.-S. Kiwanuka, T.K. Laurila and C.F. Kaminski, "Cavity enhanced absorption spectroscopy of liquid-phase reaction kinetics using broad bandwidth supercontinuum radiation" in 18th International Conference on Advanced Laser Technologies (ALT'10), **O59**. General Physics Institute of the Russian Academy of Sciences. Egmond aan Zee, the Netherlands. 11-16 September 2010.

- S.-S. Kiwanuka, T.K. Laurila and C.F. Kaminski, "Ultrasensitive cavity enhanced absorption spectroscopy of reaction kinetics in liquids with broad bandwidth supercontinuum radiation" in Photon 10, **OPD**. Institute of

Physics. Southampton, UK. 23-27 August 2010.

- E.J. Rees, C. Liu, S.-S. Kiwanuka, T.K. Laurila, C.F. Kaminski and G.D. Moggridge, "Anomalies of supercontinuum light analysed by experiment and simulation" in Photon 10, **OPD/QEP**. Institute of Physics. Southampton, UK. 23-27 August 2010.

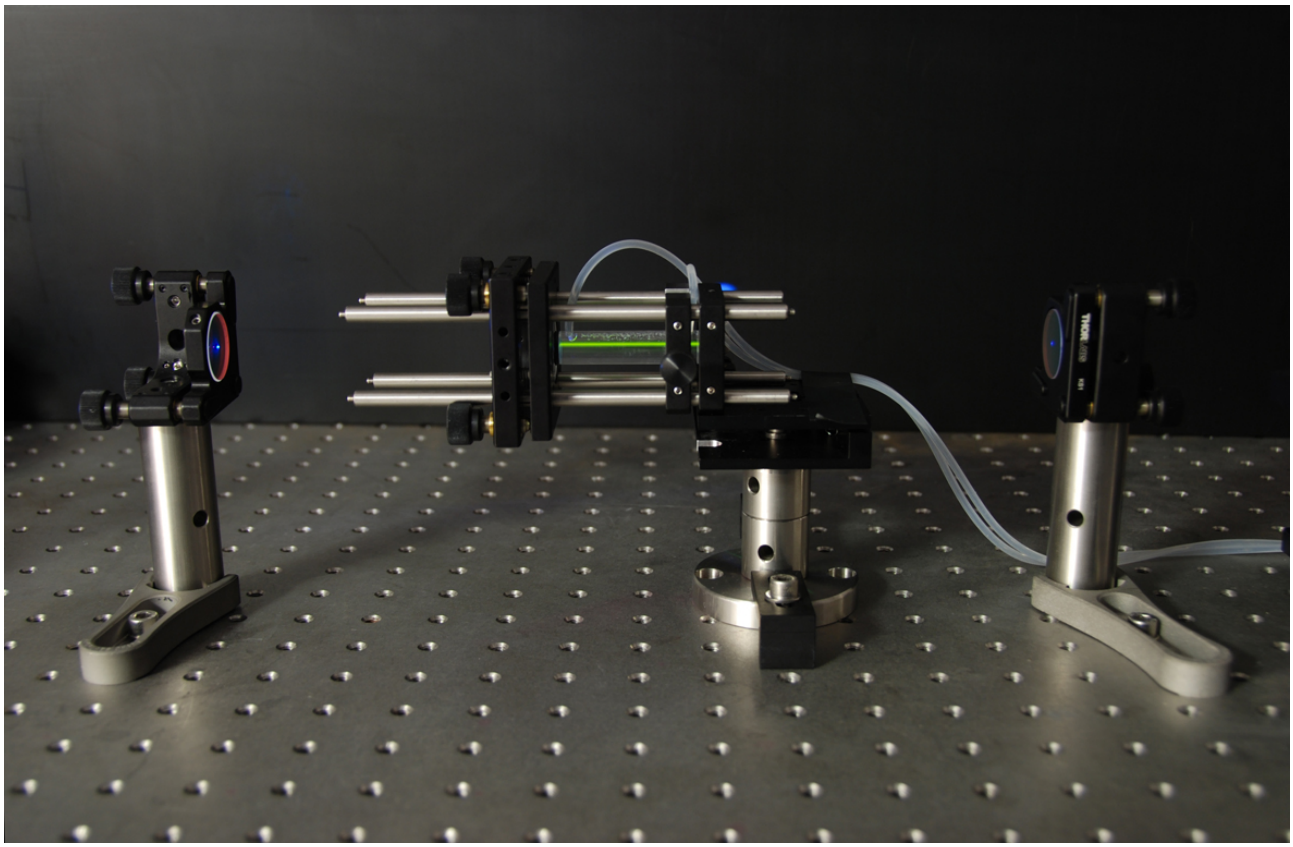

Supercontinuum light beam passing through a sample of rhodamine 6G dye solution

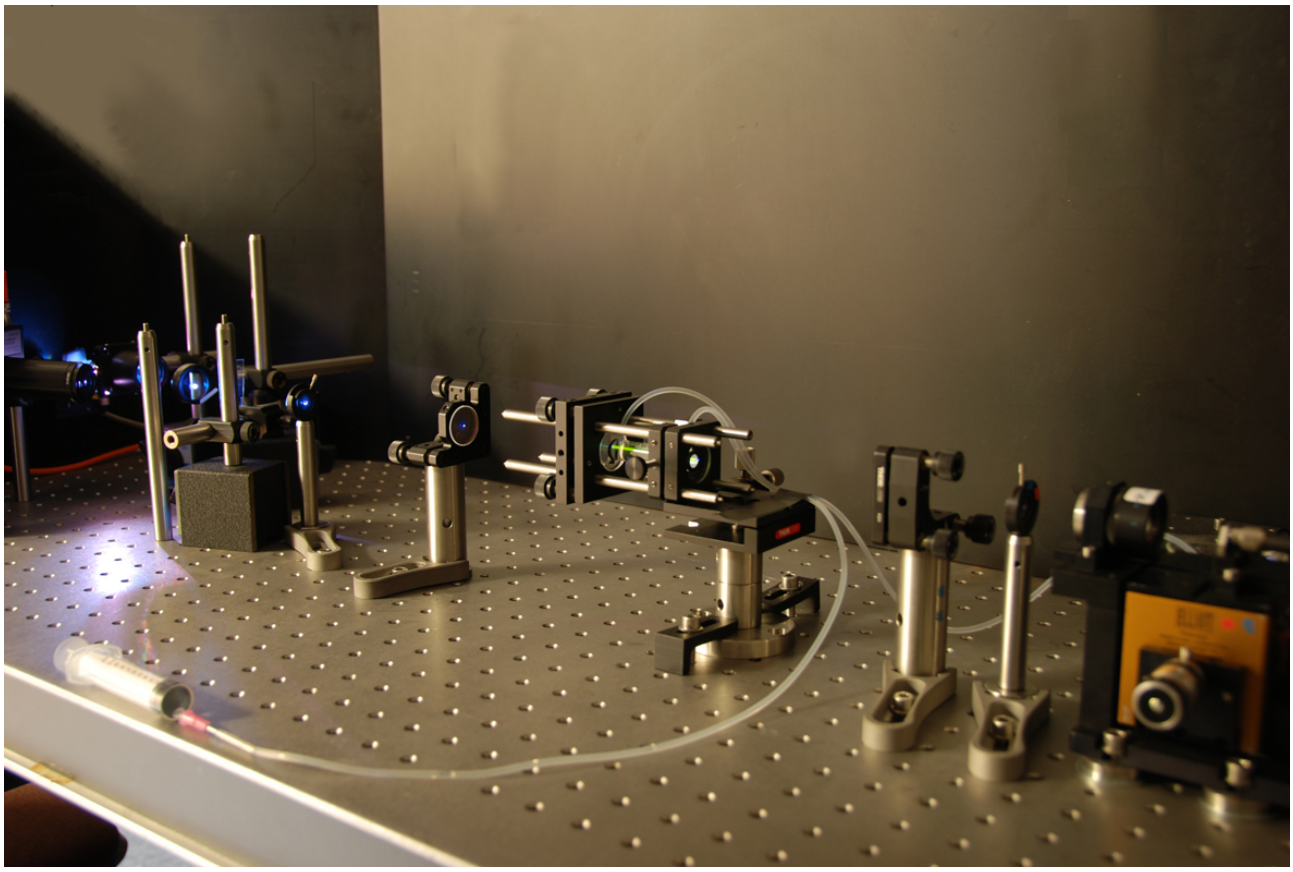

Laboratory SC-CEAS set-up of the sample cuvette inside the two-mirror optical cavity

List of Figures

References

I.M.P. Aarts, B. Hoex, A.H.M. Smets, R. Engeln, W.M.M. Kessels, and M.C.M. van de Sanden. Direct and highly sensitive measurement of defect-related absorption in amorphous silicon thin films by cavity ringdown spectroscopy. *Applied Physics Letters*, 84(16):3079–3081, 2004.

F. Adler, M.J. Thorpe, K.C. Cossel, and J. Ye. Cavity-enhanced direct frequency comb spectroscopy: Technology and applications. *Annual Review of Analytical Chemistry*, 3:175–205, 2010.

G Agrawal. *Nonlinear Fiber Optics*. Academic Press, 3rd edition, 2001.

N. Akhmediev and M. Karlsson. Cherenkov radiation emitted by solitons in optical fibers. *Physical Review A*, 51(3):2602–2607, 1995.

A.J. Alexander. Flowing liquid-sheet jet for cavity ring-down absorption measurements. *Analytical Chemistry*, 78(15):5597–5600, 2006.

R.R. Alfano. *The Supercontinuum Laser Source*. Springer-Verlag, New York, 2nd edition, 2006.

R.R. Alfano and S.L. Shapiro. Emission in the region 4000 to 7000 Å via four-photon coupling in glass. *Physical Review Letters*, 24(11):584–588, 1970.

Alzheimer's Society. Counting the cost caring for people with dementia on hospital wards. Technical report, 2009.

Alzheimers Association. 2013 Alzheimer's disease facts and figures. *Alzheimers & Dementia*, 9(2):208–245, 2013.

D.Z. Anderson, J.C. Frisch, and C.S. Masser. Mirror reflectometer based on optical cavity decay time. *Applied Optics*, 23(8):1238–1245, 1984.

C.B. Anfinsen. The formation and stabilization of protein structure. *Biochemical Journal*, 128(4):737–749, 1972.

C.B. Anfinsen. Principles that govern the folding of protein chains. *Science*, 181 (4096):223–230, 1973.

J. Arlt and M.J. Padgett. Generation of a beam with a dark focus surrounded by regions of higher intensity: The optical bottle beam. *Optics Letters*, 25(4): 191–193, 2000.

B. Bahnev, L. van der Sneppen, A.E. Wiskerke, F. Ariese, C. Gooijer, and W. Ubachs. Miniaturized cavity ring-down detection in a liquid flow cell. *Analytical Chemistry*, 77(4):1188–1191, 2005.

S.M. Ball and R.L. Jones. Broad-band cavity ring-down spectroscopy. *Chemical Reviews*, 103(12):5239–5262, 2003.

P. Beaud and W. Hodel. Ultrashort pulse propagation, pulse breakup, and fundamental soliton formation in a single-mode optical fiber. *IEEE Journal of Quantum Electronics*, (87):1938–1946, 1987.

A. Beeby, I.M. Clarkson, R.S. Dickins, S. Faulkner, D. Parker, L. Royle, A.S. de Sousa, J.A.G. Williams, and M. Woods. Non-radiative deactivation of the excited states of europium, terbium and ytterbium complexes by proximate energy-matched OH, NH and CH oscillators: An improved luminescence method for establishing solution hydration states. *Journal of the Chemical Society, Perkin Transactions 2*, 0(3):493–504, 1999.

B.P. Belousov. A periodic reaction and its mechanism. *Compilation of Abstracts on Radiation Medicine*, pages 145–147, 1959.

G. Berden and R. Engeln. *Cavity Ring-Down Spectroscopy: Techniques and Applications*. Wiley-Blackwell, 2009.

G. Berden, R. Peeters, and G. Meijer. Cavity ring-down spectroscopy: Experimental schemes and applications. *International Reviews in Physical Chemistry*, 19:565–607, 2000.

M. Bigas, E. Cabruja, J. Forest, and J. Salvi. Review of CMOS image sensors. *Microelectronics Journal*, 37(5):433–451, 2006.

K. Binnemans and C. Görller-Walrand. Optical absorption spectra of Eu^{3+} in $Y_3Ga_5O_{12}$ (YGG). *Journal of Physics: Condensed Matter*, 9:1637–1648, 1997.

T.A. Birks, W.J. Wadsworth, and P.S.J. Russell. Supercontinuum generation in tapered fibers. *Optics Letters*, 25(19):1415–1417, 2000.

G. Bitan, M.D. Kirkitadze, A. Lomakin, S.S. Vollers, G.B. Benedek, and D.B. Teplow. Amyloid β-protein (Aβ) assembly: Aβ40 and Aβ42 oligomerize through distinct pathways. *Proceedings of the National Academy of Sciences*, 100(1):330–335, 2003.

M. Born and E. Wolf. *Principles of Optics*, volume 45. Cambridge University Press, 7th edition, 1999.

M. Bouchard, J. Zurdo, E.J. Nettleton, C.M. Dobson, and C.V. Robinson. Formation of insulin amyloid fibrils followed by FTIR simultaneously with CD and electron microscopy. *Protein Science*, 9(10):1960–1967, 2000.

R.W. Boyd. *Nonlinear optics*. Academic Press, 3rd edition, 2003.

B.D. Buckner and D. L'Esperance. Digital synchroballistic schlieren camera for high-speed photography of bullets and rocket sleds. *Optical Engineering*, 52 (8):083105(1)–083105(9), 2013.

J.-C.G. Bünzli and C. Piguet. Taking advantage of luminescent lanthanide ions. *Chemical Society Reviews*, 34(12):1048–1077, 2005.

H. Cabrera, A. Marcano, and Y. Castellanos. Absorption coefficient of nearly transparent liquids measured using thermal lens spectrometry. *Condensed Matter Physics*, 9(2(46)):385–389, 2006.

B. Caughey and P.T. Lansbury. Protofibrils, pores, fibrils, and neurodegeneration: Separating the responsible protein aggregates from the innocent bystanders. *Annual Review of Neuroscience*, 26:267–298, 2003.

F.T.S. Chan, G.S. Kaminski Schierle, J.R. Kumita, C.W. Bertoncini, C.M. Dobson, and C.F. Kaminski. Protein amyloids develop an intrinsic fluorescence signature during aggregation. *Analyst*, 138(7):2156–2162, 2013.

J.S.Y. Chen, T.G. Euser, N.J. Farrer, P.J. Sadler, M. Scharrer, and P.S.J. Russell. Photochemistry in photonic crystal fiber nanoreactors. *Chemistry - A European Journal*, 16(19):5607–5612, 2010.

F. Chiti and C.M. Dobson. Protein misfolding, functional amyloid, and human disease. *Annual Review of Biochemistry*, 75(1):333–366, 2006.

S. Cotton. *Lanthanides and Actinides*. Macmillan Education, London, 1991.

S. Cova, A. Longoni, and A. Andreoni. Towards picosecond resolution with single-photon avalanche diodes. *Review of Scientific Instruments*, 52(3):408–412, 1981.

S. Cova, A. Lacaita, and G. Ripamonti. Trapping phenomena in avalanche photodiodes on nanosecond scale. *IEEE Electron Device Letters*, 12(12):685–687, 1991.

A.P. Cracknell and L. Hayes. *Introduction To Remote Sensing*. Taylor & Francis Group, 1991.

G. Cristobal, L. Arbouet, F. Sarrazin, D. Talaga, J.-L. Bruneel, M. Joanicot, and L. Servant. On-line laser Raman spectroscopic probing of droplets engineered in microfluidic devices. *Lab on a Chip*, 6(9):1140–1146, 2006.

A.M. Cubillas, M. Schmidt, M. Scharrer, T.G. Euser, B.J.M. Etzold, N. Taccardi, P. Wasserscheid, and P.S.J. Russell. Ultra-low concentration monitoring of catalytic reactions in photonic crystal fiber. *Chemistry - A European Journal*, 18(6):1586–1590, 2012.

S. Cundiff and J. Ye. Colloquium: Femtosecond optical frequency combs. *Reviews of Modern Physics*, 75(1):325–342, 2003.

H. Dautet, P. Deschamps, B. Dion, A.D. MacGregor, D. MacSween, R.J. McIntyre, C. Trottier, and P.P. Webb. Photon counting techniques with silicon avalanche photodiodes. *Applied Optics*, 32(21):3894–3900, 1993.

G.F. de Sá, O.L. Malta, C. de Mello Donegá, A.M. Simas, R.L. Longo, P.A. Santa-Cruz, and E.F. da Silva Jr. Spectroscopic properties and design of highly luminescent lanthanide coordination complexes. *Coordination Chemistry Reviews*, 196(1):165–195, 2000.

A.J. DeMello. Control and detection of chemical reactions in microfluidic systems. *Nature*, 442(7101):394–402, 2006.

Department of Health. Prime Ministers challenge on dementia. Technical report, 2012.

P. Deuflhard and F.A. Bornemann. *Numerische Mathematik*. Number 2 in De Gruyter Lehrbuch. De Gruyter, 2nd edition, 2002.

E.M. Dianov and V. Mamyshev. Stimulated-Raman conversion of multisoliton pulses in quartz optical fibers. *JETP Letters*, 41(6):242–244, 1985.

P.S. Dittrich and A. Manz. Single-molecule fluorescence detection in microfluidic channels–the holy grail in μTAS? *Analytical and Bioanalytical Chemistry*, 382 (8):1771–1782, 2005.

J.M. Dudley and S. Coen. Coherence properties of supercontinuum spectra generated in photonic crystal and tapered optical fibers. *Optics Letters*, 27(13): 1180–1182, 2002.

J.M. Dudley and J.R. Taylor. Ten years of nonlinear optics in photonic crystal fibre. *Nature Photonics*, 3(2):85–90, 2009.

J.M. Dudley, G. Genty, and S. Coen. Supercontinuum generation in photonic crystal fiber. *Reviews of Modern Physics*, 78(4):1135–1184, 2006.

J.M. Dudley, G. Genty, and B.J. Eggleton. Harnessing and control of optical rogue waves insupercontinuum generation. *Optics Express*, 16(6):3644–3651, 2008.

B.D. Dunlap and G.H. Lander. Evidence for strong localization of 5f electrons in neptunium intermetallics. *Physical Review Letters*, 33(17):1046–1048, 1974.

C. Dunsby, P.M.P. Lanigan, J. McGinty, D.S. Elson, J. Requejo-Isidro, I. Munro, N. Galletly, F. McCann, B. Treanor, B. Önfelt, D.M. Davis, M.A.A. Neil, and P.M.W. French. An electronically tunable ultrafast laser source applied to fluorescence imaging and fluorescence lifetime imaging microscopy. *Journal of Physics D: Applied Physics*, 37(23):3296–3303, 2004.

J.G. Edwards. Measurement of the cross-section for stimulated emission in neodymium glass. *Nature*, 212(5063):752–753, 1966.

H. El-Kashef. The necessary requirements imposed on polar dielectric laser dye solvents. *Physica B: Condensed Matter*, 279(4):295–301, 2000.

R. Engeln, G. von Helden, G. Berden, and G. Meijer. Phase shift cavity ring down absorption spectroscopy. *Chemical Physics Letters*, 262(1-2):105–109, 1996.

R. Engeln, G. Berden, R. Peeters, and G. Meijer. Cavity enhanced absorption and cavity enhanced magnetic rotation spectroscopy. *Review of Scientific Instruments*, 69(11):3763–3769, 1998.

R. Engeln, G. von Helden, A.J.A. van Roij, and G. Meijer. Cavity ring down spectroscopy on solid C60. *Journal of Chemical Physics*, 110(5):2732–2733, 1999.

I.R. Epstein and J.A. Pojman. *An Introduction to Nonlinear Chemical Dynamics: Oscillations, Waves, Patterns, and Chaos: Oscillations, Waves, Patterns, and Chaos*. Oxford University Press, USA, 1998.

A. Esposito. Beyond range: Innovating fluorescence microscopy. *Remote Sensing*, 4(1):111–119, 2012.

T.G. Euser, J.S.Y. Chen, M. Scharrer, P.S.J. Russell, N.J. Farrer, and P.J. Sadler. Quantitative broadband chemical sensing in air-suspended solid-core fibers. *Journal of Applied Physics*, 103(10):103108(1)–103108(7), 2008.

S. Faulkner, S.J.A. Pope, and B.P. Burton-Pye. Lanthanide complexes for luminescence imaging applications. *Applied Spectroscopy Reviews*, 40(1):1–31, 2005.

G.T. Fechner. Ueber die Anwendung des Gravitationsgesetzes auf die Atomenlehre. *Kastners Archiv für die gesamte Naturlehre*, (15):257–291, 1828.

S.E. Fiedler. *Incoherent broad-band cavity-enhanced absorption spectroscopy*. PhD thesis, Berlin, 2005.

S.E. Fiedler, A. Hese, and A.A. Ruth. Incoherent broad-band cavity-enhanced absorption spectroscopy. *Chemical Physics Letters*, 371(3-4):284–294, 2003.

R.J. Field, E. Koros, and R.M. Noyes. Oscillations in chemical systems. II. Thorough analysis of temporal oscillation in the bromate-cerium-malonic acid system. *Journal of the American Chemical Society*, 94(25):8649–8664, 1972.

W.B. Fowler and D.L. Dexter. Relation between absorption and emission probabilities in luminescent centers in ionic solids. *Physical Review*, 128(5):2154–2165, 1962.

U.F. Franck. Chemical oscillations. *Angewandte Chemie International Edition in English*, 17(1):1–15, 1978.

J.H. Frank, A.D. Elder, J. Swartling, A.R. Venkitaraman, A.D. Jeyasekharan, and C.F. Kaminski. A white light confocal microscope for spectrally resolved multidimensional imaging. *Journal of Microscopy*, 227(3):203–215, 2007.

M.H. Frosz, O. Bang, and A. Bjarklev. Soliton collision and Raman gain regimes in continuous-wave pumped supercontinuum generation. *Optics Express*, 14 (20):9391–9407, 2006.

G. Genty, M. Lehtonen, and H. Ludvigsen. Effect of cross-phase modulation on supercontinuum generated in microstructured fibers with sub-30 fs pulses. *Optics Express*, 12(19):4614–4624, 2004.

J.E. Geusic, H.M. Marcos, and L.G. Van Uitert. Laser oscillations in Nd-doped yttrium aluminum, yttrium gallium and gadolinium garnets. *Applied Physics Letters*, 4(10):182–184, 1964.

T. Gidalevitz, V. Prahlad, and R.I. Morimoto. The stress of protein misfolding: from single cells to multicellular organisms. *Cold Spring Harbor Perspectives in Biology*, 3(6):1–18, 2011.

C. Goldsbury, J. Kistler, U. Aebi, T. Arvinte, and G.J.S. Cooper. Watching amyloid fibrils grow by time-lapse atomic force microscopy. *Journal of Molecular Biology*, 285(1):33–39, 1999.

F.R. Gonçalves e Silva, O.L. Malta, C. Reinhard, H.-U. Güdel, C. Piguet, J.E. Moser, and J.-C.G. Bünzli. Visible and near-infrared luminescence of lanthanide-containing dimetallic triple-stranded helicates: Energy transfer mechanisms in the Sm^{III} and Yb^{III} molecular edifices. *Journal of Physical Chemistry A*, 106(9):1670–1677, 2002.

A. V. Gorbach and D. V. Skryabin. Theory of radiation trapping by the accelerating solitons in optical fibers. *Physical Review A*, 76(5):1–10, 2007a.

A.V. Gorbach and D.V. Skryabin. Light trapping in gravity-like potentials and expansion of supercontinuum spectra in photonic-crystal fibres. *Nature Photonics*, 1(11):653–657, 2007b.

A.V. Gorbach, D.V. Skryabin, J.M. Stone, and J.C. Knight. Four-wave mixing of solitons with radiation and quasi-nondispersive wave packets at the short-wavelength edge of a supercontinuum. *Optics Express*, 14(21):9854–9863, 2006.

C. Görller-Walrand and K. Binnemans. Spectral intensities of f-f transitions. In K.A. Gschneidner Jr. and L. Eyring, editors, *Handbook on the Physics and Chemistry of Rare Earths, volume 25*, chapter 167, pages 101–264. Elsevier, 1998.

X. Gu, L. Xu, M. Kimmel, E. Zeek, P. O'Shea, A.P. Shreenath, R. Trebino, and R.S. Windeler. Frequency-resolved optical gating and single-shot spectral measurements reveal fine structure in microstructure-fiber continuum. *Optics Letters*, 27(13):1174–6, 2002.

P. Guptasarma. Solution-state characteristics of the ultraviolet A-induced visible fluorescence from proteins. *Archives of Biochemistry and Biophysics*, 478(2): 127–129, 2008.

F. Gutierrez, C. Tedeschi, L. Maron, J.-P. Daudey, R. Poteau, J. Azema, P. Tisnès, and C. Picard. Quantum chemistry-based interpretations on the lowest triplet state of luminescent lanthanides complexes. Part 1. Relation between the triplet state energy of hydroxamate complexes and their luminescence properties. *Dalton Transactions*, (9):1334–1347, 2004.

C. Haass and D.J. Selkoe. Soluble protein oligomers in neurodegeneration: Lessons from the Alzheimer's amyloid β-peptide. *Nature Reviews Molecular Cell Biology*, 8(2):101–112, 2007.

R.H. Haitz. Mechanisms contributing to the noise pulse rate of avalanche diodes. *Journal of Applied Physics*, 36(10):3123–3131, 1965.

G.M. Hale and M.R. Querry. Optical constants of water in the 200 nm to 200 um wavelength region. *Applied Optics*, 12(3):555–563, 1973.

A.J. Hallock, E.S.F. Berman, and R.N. Zare. Direct monitoring of absorption in solution by cavity ring-down spectroscopy. *Analytical Chemistry*, 74(7):1741–1743, 2002.

A.J. Hallock, E.S.F. Berman, and R.N. Zare. Use of broadband, continuous-wave diode lasers in cavity ring-down spectroscopy for liquid samples. *Applied Spectroscopy*, 57(5):571–573, 2003.

E. Hamers, D. Schram, and R. Engeln. Fourier transform phase shift cavity ring down spectroscopy. *Chemical Physics Letters*, 365(3-4):237–243, 2002.

K. Hara, K. Hata, T. Kikuchi, and S. Kim. Application of avalanche photodiodes for scintillating fiber readout. *Nuclear Instruments and Methods in Physics Research A*, 383:252–255, 1996.

J.D. Harper and P.T. Lansbury. Models of amyloid seeding in Alzheimer's disease and scrapie:Mechanistic truths and physiological consequences of the time-dependent solubility of amyloid proteins. *Annual Review of Biochemistry*, 66 (1):385–407, 1997.

I. Hartl, X.D. Li, C. Chudoba, R.K. Ghanta, T.H. Ko, J.G. Fujimoto, J.K. Ranka, and R.S. Windeler. Ultrahigh-resolution optical coherence tomography using continuum generation in an air-silica microstructure optical fiber. *Optics Letters*, 26(9):608–610, 2001.

A. Hassani and M. Skorobogatiy. Design of the microstructured optical fiber-based surface plasmon resonance sensors with enhanced microfluidics. *Optics Express*, 14(24):11616–11621, 2006.

G. Haxel, J.B. Hedrick, and G.J. Orris. Rare Earth elements: Critical resources for high technology. Technical report, US Geological Survey, 2002.

Y. He, M. Hippler, and M. Quack. High-resolution cavity ring-down absorption spectroscopy of nitrous oxide and chloroform using a near-infrared cw diode laser. *Chemical Physics Letters*, 289:527–534, 1998.

E. Hecht. *Optics*. Addison Wesley, San Francisco, 4th edition, 2002.

L. Hegedus, M. Wittmann, Z. Noszticzius, S. Yan, A. Sirimungkala, H.-D. Forsterling, and R.J. Field. HPLC analysis of complete BZ systems. Evolution of the chemical composition in cerium and ferroin catalysed batch oscillators: experiments and model calculations. *Faraday Discussions*, 120:21–38, 2002.

A.M. Heidt, A. Hartung, G.W. Bosman, P. Krok, E.G. Rohwer, H. Schwoerer, and H. Bartelt. Coherent octave spanning near-infrared and visible supercontinuum generation in all-normal dispersion photonic crystal fibers. *Optics Express*, 19 (4):3775–3787, 2011.

Heraeus Quarzglas. Specialty fiber preforms for the most demanding applications. Technical report, 2012.

J.M. Herbelin, J.A. McKay, M.A. Kwok, R.H. Ueunten, D.S. Urevig, D.J. Spencer, and D.J. Benard. Sensitive measurement of photon lifetime and true reflectances in an optical cavity by a phase-shift method. *Applied Optics*, 19(1): 144–147, 1980.

D.R. Herriott and H.J. Schulte. Folded optical delay lines. *Applied Optics*, 4(8): 883–889, 1965.

J.T. Hodges, J.P. Looney, and R.D. van Zee. Response of a ring-down cavity to an arbitrary excitation. *Journal of Chemical Physics*, 105(23):10278–10288, 1996.

L.E. Hooper, P.J. Mosley, A.C. Muir, W.J. Wadsworth, and J.C. Knight. Coherent supercontinuum generation in photonic crystal fiber with all-normal group velocity dispersion. *Optics Express*, 19(6):4902–4907, 2011.

B.L. Horecker. The absorption spectra of hemoglobin and its derivatives in the visible and near infra-red regions. *Journal of Biological Chemistry*, 1(148): 173–183, 1943.

T.H.J. Huang, D.-S. Yang, N.P. Plaskos, S. Go, C.M. Yip, P.E. Fraser, and A. Chakrabartty. Structural studies of soluble oligomers of the Alzheimer β-amyloid peptide. *Journal of Molecular Biology*, 297(1):73–87, 2000.

S. Hüfner. *Optical spectra of transparent rare earth compounds*. Academic Press, 1978.

J. Hult. A fourth-order Runge-Kutta in the interaction picture method for simulating supercontinuum generation in optical fibers. *Journal of Lightwave Technology*, 25(12):3770–3775, 2007.

J. Hult, I.S. Burns, and C.F. Kaminski. Wide-bandwidth mode-hop-free tuning of extended-cavity GaN diode lasers. *Applied Optics*, 44(18):3675–3685, 2005.

J. Hult, R.S. Watt, and C.F. Kaminski. High bandwidth absorption spectroscopy with a dispersed supercontinuum source. *Optics Express*, 15(18):11385–11395, 2007.

A.A. Ishaaya, N. Davidson, G. Machavariani, E. Hasman, and A.A. Friesem. Efficient selection of high-order Laguerre-Gaussian modes in a Q-switched Nd:YAG laser. *IEEE Journal of Quantum Electronics*, 39(1):74–82, 2003.

M.N. Islam, G. Sucha, and I. Bar-Joseph. Femtosecond distributed soliton spectrum in fibers. *Journal of the Optical Society of America B*, 6(6):1149–1158, 1989.

T. Jimbo, V.L. Caplan, Q.X. Li, Q.Z. Wang, P.P. Ho, and R.R. Alfano. Enhancement of ultrafast supercontinuum generation in water by the addition of Zn^{2+} and K^{+} cations. *Optics Letters*, 12(7):477–479, 1987.

R.T. Jongma, M.G.H. Boogaarts, I. Holleman, and G. Meijer. Trace gas detection with cavity ring down spectroscopy. *Review of Scientific Instruments*, 66(4): 2821–2828, 1995.

B.R. Judd. Optical absorption intensities of rare-earth ions. *Physical Review*, 127 (3):750–761, 1962.

C.F. Kaminski, R.S. Watt, A.D. Elder, J.H. Frank, and J. Hult. Supercontinuum radiation for applications in chemical sensing and microscopy. *Applied Physics B*, 92(3):367–378, 2008.

V.I. Karpman. Radiation by solitons due to higher-order dispersion. *Physical Review E*, 47(3):2073–2082, 1993.

J. Kasparian, M. Rodriguez, G. Mejean, J. Yu, E. Salmon, H. Wille, R. Bourayou, S. Frey, Y.-B. Andre, A. Mysyrowicz, R. Sauerbrey, J.-P. Wolf, and L. Wöste. White-light filaments for atmospheric analysis. *Science*, 301(5629):61–64, 2003.

P.L. Kebabian, S.C. Herndon, and A. Freedman. Detection of nitrogen dioxide by cavity attenuated phase shift spectroscopy. *Analytical Chemistry*, 77(2): 724–728, 2005.

P.L. Kebabian, W.A. Robinson, and A. Freedman. Optical extinction monitor using cw cavity enhanced detection. *The Review of Scientific Instruments*, 78 (6):063102(1)–063102(9), 2007.

P.V. Kelkar, F. Coppinger, A.S. Bhushan, and B. Jalali. Time-domain optical sensing. *Electronics Letters*, 35(19):1661–1662, 1999.

J. Kido and Y. Okamoto. Organo lanthanide metal complexes for electroluminescent materials. *Chemical Reviews*, 102(6):2357–2368, 2002.

M.D. Kirkitadze, G. Bitan, and D.B. Teplow. Paradigm shifts in Alzheimer's disease and other neurodegenerative disorders: The emerging role of oligomeric assemblies. *Journal of Neuroscience Research*, 69(5):567–577, 2002.

S. Kishimoto. An avalanche diode electron detector for observing NEET. In *AIP Conference Proceedings*, volume 705, pages 881–884. American Institute of Physics, 2004.

S.-S. Kiwanuka, T.K. Laurila, and C.F. Kaminski. Sensitive method for the kinetic measurement of trace species in liquids using cavity enhanced absorption spectroscopy with broad bandwidth supercontinuum radiation. *Analytical Chemistry*, 82(17):7498–7501, 2010.

S.-S. Kiwanuka, T.K. Laurila, J.H. Frank, A. Esposito, K. Blomberg von der Geest, L. Pancheri, D. Stoppa, and C.F. Kaminski. Development of broadband cavity ring-down spectroscopy for biomedical diagnostics of liquid analytes. *Analytical Chemistry*, 84(13):5489–5493, 2012.

D. Kleine, J. Lauterbach, K. Kleinermanns, and P. Hering. Cavity ring-down spectroscopy of molecularly thin iodine layers. *Applied Physics B*, 72(2):249–252, 2001.

W.E. Klunk, J.W. Pettegrew, and D.J. Abraham. Quantitative evaluation of congo red binding to amyloid-like proteins with a β-pleated sheet conformation. *Journal of Histochemistry & Cytochemistry*, 37(8):1273–1281, 1989.

J.C. Knight. Photonic crystal fibres. *Nature*, 424:847–851, 2003.

J.C. Knight, T.A. Birks, P.S.J. Russell, and D.M. Atkin. All-silica single-mode optical fiber with photonic crystal cladding. *Optics Letters*, 21(19):1547–1549, 1996.

H. Kogelnik and T. Li. Laser beams and resonators. *Applied Optics*, 5(10): 1550–1567, 1966.

N. Korneev, E.A. Kuzin, B. Ibarra-Escamilla, M. Bello-Jiménez, and A. Flores-Rosas. Initial development of supercontinuum in fibers with anomalous dispersion pumped by nanosecond-long pulses. *Optics Express*, 16(4):2636–2645, 2008.

M. Kristiansen, J.H. Graversen, C. Jacobsen, O. Sonne, H.-J. Hoffman, S.K.A. Law, and S.K. Moestrup. Identification of the haemoglobin scavenger receptor. *Nature*, 409(6817):198–201, 2001.

H.H. Ku. Notes on the use of propagation of error formulas. *Journal of Research of the National Bureau of Standards-C. Engineering and Instrumentation*, 70C (4):263–273, 1966.

A Kudlinski, AK George, JC Knight, JC Travers, AB Rulkov, SV Popov, and JR Taylor. Zero-dispersion wavelength decreasing photonic crystal fibers for ultraviolet-extended supercontinuum generation. *Optics Express*, 14(12):5715–5722, 2006.

A. Kudlinski, M. Lelek, B. Barviau, L. Audry, and A. Mussot. Efficient blue conversion from a 1064 nm microchip laser in long photonic crystal fiber tapers for fluorescence microscopy. *Optics Express*, 18(16):16640–16645, 2010.

B. Kuswandi, Nuriman, J. Huskens, and W. Verboom. Optical sensing systems for microfluidic devices: a review. *Analytica Chimica Acta*, 601(2):141–155, 2007.

P. Lacovara, H.K. Choi, and C.A. Wang. Room-temperature diode-pumped Yb: YAG laser. *Optics Letters*, 37(1):109–11, 1991.

J.J. Lagowski. *Modern Inorganic Chemistry*. Undergraduate chemistry. Marcel Dekker, 1973.

J. Lakowicz. *Principles of Fluorescence Spectroscopy*. Kluwer Academic/Plenum Publishers, London, 2006.

J.M. Langridge, T.K. Laurila, R.S. Watt, R.L. Jones, C.F. Kaminski, and J. Hult. Cavity enhanced absorption spectroscopy of multiple trace gas species using a supercontinuum radiation source. *Optics Express*, 16(14):10178–10188, 2008.

O. Laporte and W.F. Meggers. Some rules of spectral structure. *Journal of the Optical Society of America*, 11(5):459–460, 1925.

M. Latva, H. Takalo, V.-M. Mukkala, C. Matachescu, J.C. Rodríguez-Ubis, and J. Kankare. Correlation between the lowest triplet state energy level of the ligand and lanthanide(III) luminescence quantum yield. *Journal of Luminescence*, 75(2):149–169, 1997.

T.K. Laurila, I.S. Burns, J. Hult, J.H. Miller, and C.F. Kaminski. A calibration method for broad-bandwidth cavity enhanced absorption spectroscopy performed with supercontinuum radiation. *Applied Physics B*, 102(2):271–278, 2010.

J.H. Lee, J. van Howe, X. Liu, and C. Xu. Soliton self-frequency shift: Experimental demonstrations and applications. *IEEE Journal of Selected Topics in Quantum Electronics*, 14(3):713–723, 2008.

K.K. Lehmann and D. Romanini. The superposition principle and cavity ringdown spectroscopy. *Journal of Chemical Physics*, 105(23):10263–10277, 1996.

K.K. Lehmann, G. Berden, and R. Engeln. An Introduction to Cavity Ring-down Spectroscopy. In *Cavity Ring-Down Spectroscopy*, pages 1–26. John Wiley & Sons, 2010.

S. Leon-Saval, T. Birks, W. Wadsworth, P.S.J. Russell, and M. Mason. Supercontinuum generation in submicron fibre waveguides. *Optics Express*, 12(13): 2864–2869, 2004.

S.-A. Leung, R.F. Winkle, R.C.R. Wootton, and A.J. DeMello. A method for rapid reaction optimisation in continuous-flow microfluidic reactors using online Raman spectroscopic detection. *Analyst*, 130(1):46–51, 2005.

M. Lindgren and P. Hammarström. Amyloid oligomers: Spectroscopic characterization of amyloidogenic protein states. *FEBS Journal*, 277(6):1380–1388, 2010.

C. Liu, E.J. Rees, T.K. Laurila, S. Jian, and C.F. Kaminski. Predicting supercontinuum pulse collisions with simulations exhibiting temporal aliasing. *Optics Letters*, 35(24):4145–4147, 2010.

C. Liu, E.J. Rees, T. Laurila, S. Jian, and C.F. Kaminski. Periodic interactions between solitons and dispersive waves during the generation of non-coherent supercontinuum radiation. *Optics Express*, 20(6):6316–6324, 2012.

H. Lodish, A. Berk, S.L. Zipursky, P. Matsudaira, D. Baltimore, and J. Darnell. *Molecular Cell Biology*. W. H. Freeman, 4th edition, 2000.

S.L. Logunov. Cavity ringdown detection of losses in thin films in the telecommunication wavelength window. *Applied Optics*, 40(9):1570–1573, 2001.

A. Lomakin, D.S. Chung, G.B. Benedek, D.A. Kirschner, and D.B. Teplow. On the nucleation and growth of amyloid β-protein fibrils: detection of nuclei and quantitation of rate constants. *Proceedings of the National Academy of Sciences*, 93(3):1125–1129, 1996.

T. Lührs, C. Ritter, M. Adrian, D. Riek-Loher, B. Bohrmann, H. Döbeli, D. Schubert, and R. Riek. 3D structure of Alzheimer's amyloid-β(142) fibrils. *Proceedings of the National Academy of Sciences*, 102(48):17342–17347, 2005.

J.D. Main Smith. The rare earths. *Nature*, 120:583–584, 1927.

I.H. Malitson. Interspecimen comparison of the refractive index of fused silica. *Journal of the Optical Society of America*, 55(10):1205–1208, 1965.

I.A. Mastrangelo, M. Ahmed, T. Sato, W. Liu, C. Wang, P. Hough, and S.O. Smith. High-resolution atomic force microscopy of soluble Aβ42 Oligomers. *Journal of Molecular Biology*, 358(1):106–119, 2006.

D.V. Matyushov and M.D. Newton. Understanding the optical band shape: Coumarin-153 steady-state spectroscopy. *Journal of Physical Chemistry A*, 105(37):8516–8532, 2001.

M. Mazurenka, A.J. Orr-Ewing, R. Peverall, and G.A.D. Ritchie. Cavity ring-down and cavity enhanced spectroscopy using diode lasers. *Annual Reports Section "C" (Physical Chemistry)*, 101(001):100–142, 2005.

J.R. McColl and F.C. Palilla. Use of rare earths in television and cathode ray phosphors. In *Industrial Applications of Rare Earth Elements*, ACS Symposium Series, pages 177–193. American Chemical Society, 1981.

G. McConnell. Confocal laser scanning fluorescence microscopy with a visible continuum source. *Optics Express*, 12(13):2844–2850, 2004.

T. McGarvey, A. Conjusteau, and H. Mabuchi. Finesse and sensitivity gain in cavity-enhanced absorption spectroscopy of biomolecules in solution. *Optics Express*, 14(22):10441–10451, 2006.

G. Meijer, M.G.H. Boogaarts, R.T. Jongma, D.H. Parker, and A.M. Wodtke. Coherent cavity ring down spectroscopy. *Chemical Physics Letters*, 217(1-2): 112–116, 1994.

V.K.L. Mer. Monodisperse colloids and higher-order Tyndall spectra. *The Journal of Physical and Colloid Chemistry*, 52(1):65–76, 1948.

G. Mie. Beiträge zur Optik trüber Medien, speziell kolloidaler Metallösungen. *Annalen der Physik*, 330(3):377–445, 1908.

S.K. Mishra and P.K. Dasgupta. Capillary scale light emitting diode based multi-reflection absorbance detector. *Analytica Chimica Acta*, 605(2):166–174, 2007.

D.M. Mittleman, R.H. Jacobsen, and M.C. Nuss. T-ray imaging. *IEEE Journal of Selected Topics in Quantum Electronics*, 2(3):679–692, 1996.

T Moeller. Periodicity and the lanthanides and actinides. *Journal of Chemical Education*, 47(6):417–423, 1970.

K.B. Mogensen, H. Klank, and J.P. Kutter. Recent developments in detection for microfluidic systems. *Electrophoresis*, 25(21-22):3498–3512, 2004.

L.F. Mollenauer and J.P. Gordon. *Solitons in Optical Fibers: Fundamentals and Applications*. Elsevier Science, 2006.

E. Moreels, C. de Greef, and R. Finsy. Laser light refractometer. *Applied Optics*, 23(17):3010–3013, 1984.

A. Morel. Optical properties of pure water and pure sea water. *Optical Aspects of Oceanography*, 52(1):217–229, 1974.

C.A. Morrison and R.P. Leavitt. Spectroscopic properties of triply ionized lanthanides in transparent host materials. In K.A. Gschneidner Jr. and L. Eyring, editors, *Handbook on the Physics and Chemistry of Rare Earths, volume 5*, chapter 46, pages 461–692. Elsevier, 1982.

O. Moudam, B.C. Rowan, M. Alamiry, P. Richardson, B.S. Richards, A.C. Jones, and N. Robertson. Europium complexes with high total photoluminescence quantum yields in solution and in PMMA. *Chemical Communications*, (43): 6649–6651, 2009.

R.N. Muir and A.J. Alexander. Structure of monolayer dye films studied by Brewster angle cavity ringdown spectroscopy. *Physical Chemistry Chemical Physics*, 5(6):1279–1283, 2003.

A. Mussot, A. Kudlinski, M. Kolobov, E. Louvergneaux, M. Douay, and M. Taki. Observation of extreme temporal events in CW-pumped supercontinuum. *Optics Express*, 17(19):17010–17015, 2009.

A.B. Myers. Molecular electronic spectral broadening in liquids and glasses. *Annual Review of Physical Chemistry*, 49:267–295, 1998.

F.B. Myers and L.P. Lee. Innovations in optical microfluidic technologies for point-of-care diagnostics. *Lab on a Chip*, 8(12):2015–2031, 2008.

R.L. Nagel and Q.H. Gibson. The binding of hemoglobin to haptoglobin and its relation to subunit dissociation of hemoglobin. *Journal of Biological Chemistry*, 246(1):69–73, 1971.

H. Naiki, K. Higuchi, M. Hosokawa, and T. Takeda. Fluorometric determination of amyloid fibrils in vitro using the fluorescent dye, thioflavine T. *Analytical Biochemistry*, 177(2):244–249, 1989.

A.V. Naumov. Review of the world market of rare-earth metals. *Russian Journal of Non-Ferrous Metals*, 49(1):14–22, 2008.

S.R.T. Neil, C.M. Rushworth, C. Vallance, and S.R. Mackenzie. Broadband cavity-enhanced absorption spectroscopy for real time, in situ spectral analysis of microfluidic droplets. *Lab on a Chip*, 11(23):3953–3955, 2011.

R.G. Neville. Practice research: Evaluation of portable haemoglobinometer in general practice. *British Medical Journal*, 294(6582):1263–1265, 1987.

S.M. Newman, I.C. Lane, A.J. Orr-Ewing, D.A. Newnham, and J. Ballard. Integrated absorption intensity and Einstein coefficients for the O_2 $a^1\ \Delta_g$–$X^3\ \Sigma_g^-$ (0,0) transition: A comparison of cavity ringdown and high resolution Fourier transform spectroscopy with a long-path absorption cell. *Journal of Chemical Physics*, 110(22):10749–10757, 1999.

N.T. Nguyen and S.T. Wereley. *Fundamentals and Applications of Microfluidics*. Artech House, 2002.

N. Nishizawa and T. Goto. Characteristics of pulse trapping by ultrashort soliton pulse in optical fibers across zerodispersion wavelength. *Optics Express*, 10(21): 1151–1159, 2002.

NKT Photonics. Supercontinuum generation in photonic crystal fibers. 2:1–10, 2009.

N. Nonaka, K. Itoh, M. Nakamura, K. Niwa, K. Yamamotob, and Y. Ishikawab. An APD linear array for scintillating fiber tracker read-out. *Nuclear Instruments and Methods in Physics Research Section A*, 383:81–88, 1996.

R.M. Noyes and R.J. Field. Oscillatory chemical reactions. *Annual Review of Physical Chemistry*, 25(1):95–119, 1974.

G.S. Ofelt. Intensities of crystal spectra of rare-Earth ions. *Journal of Chemical Physics*, 37(3):511–520, 1962.

A. O'Keefe and D.A.G. Deacon. Cavity ring-down optical spectrometer for absorption measurements using pulsed laser sources. *Review of Scientific Instruments*, 2544(12):2544–2551, 1988.

J.S. Olson, E.W. Foley, C. Rogge, A.-L. Tsai, M.P. Doyle, and D.D. Lemon. NO scavenging and the hypertensive effect of hemoglobin-based blood substitutes. *Free Radical Biology & Medicine*, 36(6):685–97, 2004.

W. Ostwald. Periodisch Veränderliche Reaktionsgeschwindigkeiten. *Physikalische Zeitschrift*, 1:87–88, 1899.

W. Ostwald. *Periodische Erscheinungen bei der Auflösung des Chroms in Säuren.* BG Teubner, 1900.

B. Ouyang and R.L. Jones. Understanding the sensitivity of cavity-enhanced absorption spectroscopy: Pathlength enhancement versus noise suppression. *Applied Physics B*, 2012.

Y.L. Pan and R.K. Chang. Multiple-anode PMT behaves like many detectors in one. *Laser Focus World*, (5):3–5, 2001.

Y.L. Pan and R.K. Chang. Multiple-anode PMT makes possible the detection, discrimination, enrichment, and deposition of bioaerosols on-the-fly. Technical report, Hamamatsu Photonics, 2006.

L. Pancheri and D. Stoppa. A SPAD-based pixel linear array for high-speed time-gated fluorescence lifetime imaging. In *Proceedings of ESSCIRC 2009*, pages 428–431, 2009.

E. Peters, S.A. Diddams, and P. Fendel. A deep-UV optical frequency comb at 205 nm. *Optics Express*, 17(11):233–237, 2009.

A.T. Petkova, R.D. Leapman, Z. Guo, W.-M. Yau, M.P. Mattson, and R. Tycko. Self-propagating, molecular-level polymorphism in Alzheimer's β-amyloid fibrils. *Science*, 307(5707):262–265, 2005.

R.D. Pimentel and G.C. Sprately. *Understanding Chemistry*. Holden-Day, San Francisco, 1971.

A.C.R. Pipino, J.W. Hudgens, and R.E. Huie. Evanescent wave cavity ring-down spectroscopy for probing surface processes. *Chemical Physics Letters*, 280(12): 104–112, 1997.

R.M. Pope and E.S. Fry. Absorption spectrum (380-700 nm) of pure water. II. Integrating cavity measurements. *Applied Optics*, 36(33):8710–8723, 1997.

M.J. Potasek and G.P. Agrawal. Self-amplitude-modulation of optical pulses in nonlinear dispersive fibers. *Physical Review A*, 36(8):3862–3868, 1987.

I.M. Povey, A.M. South, and A.K. de Roodenbeke. A broadband lidar for the measurement of tropospheric constituent profiles from the ground. *Journal of Geophysical Research*, 103(D3):3369–3380, 1998.

C.V. Raman and K.S. Krishnan. A new type of secondary radiation. *Nature*, 121 (3048):501–502, 1928.

E. Randone, G. Martini, M. Fathi, and S. Donati. SPAD-array photoresponse is increased by a factor 35 by use of a microlens array concentrator. In *LEOS Annual Meeting Conference Proceedings*, pages 324–325. IEEE, 2009.

J.K. Ranka, R.S. Windeler, and A.J. Stentz. Visible continuum generation in air-silica microstructure optical fibers with anomalous dispersion at 800 nm. *Optics Letters*, 25(1):25–27, 2000.

B.J.W.S. Rayleigh. *Scientific Papers: 1881-1887*. University Press, 1900.

P.M. Rentzepis. Picosecond chemical and biological events. *Science*, 202(4364): 174–82, 1978.

C.E. Rippmann, P.C. Nett, D. Popovic, B. Seifert, T. Pasch, and D.R. Spahn. Hemocue, an accurate bedside method of hemoglobin measurement? *Journal of Clinical Monitoring*, 13(6):373–377, 1997.

J.W. Robinson, E.M.S. Frame, and G.M. Frame. *Undergraduate Instrumental Analysis*. Taylor & Francis, 6th edition, 2004.

C. Rogers and W.F. Shadwick. *Bäcklund Transformations and Their Applications*. Academic Press, 1982.

D. Romanini and K.K. Lehmann. Ring-down cavity absorption spectroscopy of the very weak HCN overtone bands with six, seven, and eight stretching quanta. *Journal of Chemical Physics*, 99(9):6287–6301, 1993.

D. Romanini, A.A. Kachanov, N. Sadeghi, and F. Stoeckel. CW cavity ring down spectroscopy. *Chemical Physics Letters*, 264:316–322, 1997.

R.P. Rother, L. Bell, P. Hillmen, and M.T. Gladwin. The clinical sequelae of intravascular hemolysis and extracellular plasma hemoglobin: A novel mechanism of human disease. *Journal of the American Medical Association*, 293 (13):1653–1662, 2005.

A. Rulkov, M. Vyatkin, S. Popov, J. Taylor, and V. Gapontsev. High brightness picosecond all-fiber generation in 525-1800 nm range with picosecond Yb pumping. *Optics Express*, 13(2):377–381, 2005.

C.M. Rushworth, J. Davies, J.T. Cabral, P.R. Dolan, J.M. Smith, and C. Vallance. Cavity-enhanced optical methods for online microfluidic analysis. *Chemical Physics Letters*, 554:1–14, 2012.

P.S.J. Russell. Photonic crystal fibers. *Science*, 299(5605):358–362, 2003.

S.T. Sanders. Wavelength-agile fiber laser using group-velocity dispersion of pulsed super-continua and application to broadband absorption spectroscopy. *Applied Physics B: Lasers and Optics*, 75:799–802, 2002.

J. Satsuma and N. Yajima. Initial value problems of one-dimensional self-modulation of nonlinear waves in dispersive media. *Supplement of the Progress of Theoretical Physics*, (55):284–306, 1974.

N. Savage. Supercontinuum sources. *Nature Photonics*, 3(2):114–115, 2009.

T. Sawada, S. Oda, and H. Shimizu. Laser-induced photoacoustic spectroscopy of some rare earth ions in aqueous solutions. *Analytical Chemistry*, 51(6):688–690, 1979.

J.J. Scherer, J.B. Paul, H. Jiao, and A. O'Keefe. Broadband ringdown spectral photography. *Applied Optics*, 40(36):6725–6732, 2001.

A. Schliesser, N. Picqué, and T.W. Hänsch. Mid-infrared frequency combs. *Nature Photonics*, 6:440–449, 2012.

K.J. Schulz and W.R. Simpson. Frequency-matched cavity ring-down spectroscopy. *Chemical Physics Letters*, 297:523–529, 1998.

L.N. Seetohul, Z. Ali, and M. Islam. Liquid-phase broadband cavity enhanced absorption spectroscopy (BBCEAS) studies in a 20 cm cell. *Analyst*, 134(9): 1887–1895, 2009.

K.S. Shah, R. Farrell, R. Grazioso, R. Myers, and L. Cirignano. Large-area APDs and monolithic APD arrays. *IEEE Transactions on Nuclear Science*, 48 (6):2352–2356, 2001.

N. Shanks. Modeling biological systems: The Belousov–Zhabotinsky reaction. *Foundations of Chemistry*, 3(1):33–53, 2001.

D.F. Shriver and P.W. Atkins. *Inorganic Chemistry*. W.H. Freeman and Co., 1999.

A.E. Siegman. *Lasers*. University Science Books, 1986.

F. Silva, D.R. Austin, A. Thai, M. Baudisch, M. Hemmer, D. Faccio, A. Couairon, and J. Biegert. Multi-octave supercontinuum generation from mid-infrared filamentation in a bulk crystal. *Nature Communications*, 33(807):1–5, 2012.

D.V. Skryabin and A.V. Yulin. Theory of generation of new frequencies by mixing of solitons and dispersive waves in optical fibers. *Physical Review E*, 72(1):1–10, 2005.

A.H.M. Smets, J.H. van Helden, and M.C.M. van de Sanden. Bulk and surface defects in a-Si:H films studied by means of the cavity ring down absorption technique. *Journal of Non-Crystalline Solids*, 299-302:610–614, 2002.

A.V. Smith and B.T. Do. Bulk and surface laser damage of silica by picosecond and nanosecond pulses at 1064 nm. *Applied Optics*, 47(26):4812–4832, 2008.

A.V. Smith, B.T. Do, G.R. Hadley, and R.L. Farrow. Optical damage limits to pulse energy from fibers. *IEEE Journal of Selected Topics in Quantum Electronics*, 15(1):153–158, 2009.

S.P. Stark, T. Steinmetz, R.A. Probst, H. Hundertmark, T. Wilken, T.W. Hänsch, Th. Udem, P.S.J. Russell, and R. Holzwarth. 14 GHz visible supercontinuum generation: calibration sources for astronomical spectrographs. *Optics Express*, 19(17):15690–15695, 2011.

K. Stelmaszczyk, P. Rohwetter, M. Fechner, M. Queier, A. Czyzewski, T. Stacewicz, and L. Wöste. Cavity ring-down absorption spectrography based on filament-generated supercontinuum light. *Optics Express*, 17(5):3673–3678, 2009.

K. Stelmaszczyk, W.M. Nakaema, Z.-Q. Hao, P. Rohwetter, and L. Wöste. Probing of multi component gas samples by means of supercontinuum CRD-spectrography. In *Conference on Lasers and Electro-Optics (CLEO): Science and Innovations*, pages 11–12. Optical Society of America, 2011.

J. M. Stone and J. C. Knight. From zero dispersion to group index matching: How tapering fibers offers the best of both worlds for visible supercontinuum generation. *Optical Fiber Technology*, 18(5):315–321, 2012.

J.M. Stone and J.C. Knight. Visibly "white" light generation in uniform photonic crystal fiber using a microchip laser. *Optics Express*, 16(4):2670–2675, 2008.

D. Stoppa and D. Mosconi. Single-photon avalanche diode CMOS sensor for time-resolved fluorescence measurements. *IEEE Sensors Journal*, 9(9):1084–1090, 2009.

C.G. Tarsitano and C.R. Webster. Multilaser Herriott cell for planetary tunable laser spectrometers. *Applied Optics*, 46(28):6923–6935, 2007.

M.J. Thorpe, K.D. Moll, R.J. Jones, B. Safdi, and J. Ye. Broadband cavity ringdown spectroscopy for sensitive and rapid molecular detection. *Science*, 311(5767):1595–1599, 2006.

F.K. Tittel, D. Richter, and A. Fried. Mid-Infrared Laser Applications in Spectroscopy. In *Solid-State Mid-Infrared Laser Sources*, volume 516, chapter 11, pages 445–516. Springer-Verlag, Berlin Heidelberg, 2003.

J.C. Travers. Blue extension of optical fibre supercontinuum generation. *Journal of Optics*, 12(113001):1–19, 2010.

J.C. Travers, A.B. Rulkov, S.V. Popov, J.R. Taylor, A. Kudlinski, A.K. George, and J.C. Knight. Multi-Watt supercontinuum generation from 0.3 to 2.4 m in PCF tapers. In *Conference on Lasers and Electro-Optics (CLEO): Science and Innovations*, pages 2062–2063. Optical Society of America, 2007.

M. Trojanowicz. Recent developments in electrochemical flow detections–a review: part I. Flow analysis and capillary electrophoresis. *Analytica Chimica Acta*, 653(1):36–58, 2009.

T. Udem, R. Holzwarth, and T.W. Hänsch. Optical frequency metrology. *Nature*, 416:233–237, 2002.

P. Urquhart. Review of rare earth doped fibre lasers and amplifiers. *IEE Proceedings J (Optoelectronics)*, 135(6):385, 1988.

U.S. Department of Health and Human Services. National plan to address Alzheimer's disease. Technical report, 2012.

V.N. Uversky, J. Li, P. Souillac, I.S. Millett, S. Doniach, R. Jakes, M. Goedert, and A.L. Fink. Biophysical properties of the synucleins and their propensities to fibrillate: Inhibition of α-synuclein assembly by β- and γ-synucleins. *Journal of Biological Chemistry*, 277(14):11970–11978, 2002.

L. van der Sneppen, A. Wiskerke, F. Ariese, C. Gooijer, and W. Ubachs. Improving the sensitivity of HPLC absorption detection by cavity ring-down spectroscopy in a liquid-only cavity. *Analytica Chimica Acta*, 558:2–6, 2006.

L. van der Sneppen, G. Hancock, C.F. Kaminski, T.K. Laurila, S.R. Mackenzie, S.R.T. Neil, R. Peverall, G.A.D. Ritchie, M. Schnippering, and P.R. Unwin. Following interfacial kinetics in real time using broadband evanescent wave cavity-enhanced absorption spectroscopy: a comparison of light-emitting diodes and supercontinuum sources. *Analyst*, 135(1):133–139, 2010.

H.J. Vreman, J.J. Mahoney, A.L. Van Kessel, and D.K. Stevenson. Carboxyhemoglobin as measured by gas chromatography and with the IL 282 and 482 CO-Oximeters. *Clinical Chemistry*, 34(12):2562–2566, 1988.

W.J. Wadsworth, A. Ortigosa-Blanch, J.C. Knight, T.A. Birks, T.-P.M. Man, and P.S.J. Russell. Supercontinuum generation in photonic crystal fibers and optical fiber tapers: A novel light source. *Journal of the Optical Society of America B*, 19(9):2148–2155, 2002.

H. Waechter, D. Munzke, A. Jang, and H.-P. Loock. Simultaneous and continuous multiple wavelength absorption on nanoliter volumes based on frequency-division multiplexing fiber-loop cavity ring-down spectroscopy. *Analytical Chemistry*, 83(7):2719–2725, 2011.

P. K. Wai, C.R. Menyuk, Y.C. Lee, and H.H. Chen. Nonlinear pulse propagation in the neighborhood of the zero-dispersion wavelength of monomode optical fibers. *Optics Letters*, 11(7):464–466, 1986.

R.S. Watt, C.F. Kaminski, and J. Hult. Generation of supercontinuum radiation in conventional single-mode fibre and its application to broadband absorption spectroscopy. *Applied Physics B*, 90(1):47–53, 2008.

R.S. Watt, T.K. Laurila, C.F. Kaminski, and J. Hult. Cavity enhanced spectroscopy of high-temperature H_2O in the near-infrared using a supercontinuum light source. *Applied Spectroscopy*, 63(12):1389–1395, 2009.

P. Werle, R. Mücke, and F. Slemr. The limits of signal averaging in atmospheric trace-gas monitoring by tunable diode-laser absorption spectroscopy (TDLAS). *Applied Physics B*, 139:131–139, 1993.

M.H.V. Werts, R.T.F. Jukes, and J.W. Verhoeven. The emission spectrum and the radiative lifetime of Eu^{3+} in luminescent lanthanide complexes. *Physical Chemistry Chemical Physics*, 4(9):1542–1548, 2002.

P. Westermark, U. Engström, K.H. Johnson, G.T. Westermark, and C. Betsholtz. Islet amyloid polypeptide: Pinpointing amino acid residues linked to amyloid fibril formation. *Proceedings of the National Academy of Sciences*, 87(13):5036–5040, 1990.

J.U. White. Long optical paths of large aperture. *Journal of the Optical Society of America*, 32:285–288, 1942.

G.M. Whitesides. The origins and the future of microfluidics. *Nature*, 442:368–373, 2006.

G.O.S. Williams, J.S.Y. Chen, T.G. Euser, P.S.J. Russell, and A.C. Jones. Photonic crystal fibre as an optofluidic reactor for the measurement of photochemical kinetics with sub-picomole sensitivity. *Lab on a Chip*, 12(18):3356–3361, 2012.

L.R. Wilson, B.C. Rowan, N. Robertson, O. Moudam, A.C. Jones, and B.S. Richards. Characterization and reduction of reabsorption losses in luminescent solar concentrators. *Applied Optics*, 49(9):1651–1661, 2010.

W.J. Wiscombe. Improved Mie scattering algorithms. *Applied Optics*, 19(9): 1505–1509, 1980.

World Health Organistion. Dementia: A public health priority. Technical report, 2012.

C. Xiong, A. Witkowska, S.G. Leon-Saval, T.A. Birks, and W.J. Wadsworth. Enhanced visible continuum generation from a microchip 1064 nm laser. *Optics Express*, 14(13):6188–6193, 2006.

S. Xu, G. Sha, and J. Xie. Cavity ring-down spectroscopy in the liquid phase. *Review of Scientific Instruments*, 73(2):255–258, 2002.

V.W.W. Yam and K.K.W. Lo. Recent advances in utilization of transition metal complexes and lanthanides as diagnostic tools. *Coordination Chemistry Reviews*, 184(1998):157–240, 1999.

A. Yariv. *Optical Electronics in Modern Communications*. Oxford University Press, USA, 5th edition, 1997.

H.H. Yue, S.J. Qin, and R.J. Markle. Fault detection of plasma etchers using optical emission spectra. *IEEE Transactions on Semiconductor Manufacturing*, 13(3):374–385, 2000.

D.A. Yushchenko, J.A. Fauerbach, S. Thirunavukkuarasu, E.A. Jares-Erijman, and T.M. Jovin. Fluorescent ratiometric MFC probe sensitive to early stages of α-synuclein aggregation. *Journal of the American Chemical Society*, 132 (23):7860–7861, 2010.

P. Zalicki and R.N. Zare. Cavity ring-down spectroscopy for quantitative absorption measurements. *Journal of Chemical Physics*, 102(7):2708–2717, 1995.

G. Zandomeneghi, M.R.H. Krebs, M.G. McCammon, and M. Fändrich. FTIR reveals structural differences between native β-sheet proteins and amyloid fibrils. *Protein Science*, 13(12):3314–3321, 2004.

J.J. Zayhowski. Microchip lasers. *Optical Materials*, 11:255–267, 1999.

References

A.M. Zhabotinsky. Periodic processes of malonic acid oxidation in a liquid phase. *Biofizika*, 9:306–311, 1964.

A.M. Zhabotinsky and A.N. Zaikin. Oscillatory processes in biological and chemical systems. *Pushchino on Oka*, 2:279–283, 1971.

W.G. Zijlstra, A. Buursma, and W.P. Meeuwsen-van der Roest. Absorption spectra of human fetal and adult oxyhemoglobin, de-oxyhemoglobin, carboxyhemoglobin, and methemoglobin. *Clinical Chemistry*, 37(9):1633–1638, 1991.